Final Reports of Individual Researchers

Improved hydrogen production by cyanobacteria with the use of hydrogen-absorbing alloys

Yasuo ASADA and Nobuyuki NISHIMIYA
Energy Technology

There have been some kinds of hydrogen producing microorganisms; anaerobic fermenters with degradation of organic materials, and photosynthetic microorganisms (microalgae, cyanobacteria and photosynthetic bacteria) under specific conditions.

The enzymes producing and/or consuming hydrogen are nitrogenase and hydrogenase.
Hydrogen absorbing alloys (e.g., Fe/V/Zr) were encapsulated by SSG (Softened Sol Gel) method. The encapsulated metals were tolerant to oxygen and water. The metal was put in a closed vessel containing culture of nitrogen-fixing hydrogen producer, *Anabaeana cylindrica* under photosynthetic conditions or auto-fermentative hydrogen producer, *Spirulina platensis* in the dark and anaerobic conditions for several days. The total amount of hydrogen recovered in the alloys and Ar gas phase was higher in the presence of metal than in the absence of it (Japanese Patent ２０１１－１２４５９７). It is suggested that the hydrogen absorbing alloys affected the balance of hydrogen production and uptake in these hydrogen producers.

We adopted the SSG hydrogen absorbing alloys to facultative fermenter, *Enterobacter aerogenes*, also. The results were similar as for the cyanobacteria (the alloys were stimulative for the yields of hydrogen production). We are trying to adopt to the alloys to anoxygenic photosynthetic bacteria that produce hydrogen with nitrogenase system.The results above is the first step for further improvement of biohydrogen production. Besides of improvement of light energy conversion, new alloys which are reactive in lower pressure with higher rate of hydrogen absorption.

Asymmetric reduction of isoxazole by photosynthetic bacteria (by Asada's group)
It was reported that the intact cells of a cyanobacterium, *Synechococcus* PCC7942 reduce isoxazole or acetophenones into its s-type alcohol form. It is estimated that alcohol dehydrogenase could be catalyzed, however, what enzyme is really working is not so clear. We planned that three alcohol dehydrogenase genes from *Synechocytis* PCC6308 into a photosynthetic bacterium *Rhodobacter sphaeroides* RV by using RP4-derived conjugative vecter. It was at first successful in conjugative transformation. Three transconjugat carrying each alcohol dehydrogenase gene are demonstrated to have active alcohol dehydrogenase activity in its cell-free extract. Furthermore, we found alcohol assimilating *Rhodopseudomonas viridis* No.7 can asymmetrically reduce isookisazoles and acetophenone into their S form of alcohols. Then, we tried the transconjugants including *Rp.viridis* No.7's alcohol dehydrogenase for asymmetric reduction. We repeated the reduction experiments under various conditions. However, the transconjugant might vary into weak or no activity even for ethanol or butanol. The reason is not clear, but estimated to be to instability of transconjugation vector. The vectors might be lost during repeating the transfer the culture. The results are not enough (less than half of the plan). The author, Asada is very thankful to Lecturer, Ken-ich Ito, in our section for analysis of isoxazoles and acetophenones and Prof. Hideki Khono for making transconjugants.

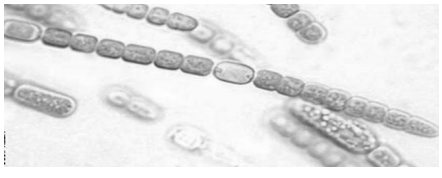

A.cylindrica

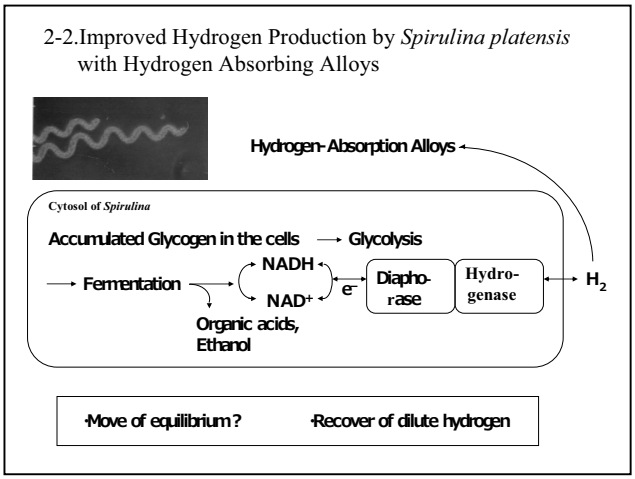

Hypothetical hydrogen metabolism in *S.platensis*

Control of Self-Organized Magnetized Plasmoids and Their Applications to Nano-Materials and Medical Technologies

Tomohiko ASAI
Nanomaterials and Nanodevices

Self-organized magnetized plasmoid has attractive advantages for the variety of applications because of its wide range of plasma parameters and its ease of control. In this work, applications of the magnetized plasmoid for a rapid thin-film deposition and EUV light source have been proposed and demonstrated. Also, several innovative applications of the plasma formation technique, e.g. medical treatment and muon catalyzed nuclear fusion have been proposed and initiated in this project.

1. Development of high-speed film deposition technique by magnetized coaxial plasma gun

Magnetized Coaxial Plasma Gun (MCPG) has been applied for new alloy film deposition technique of Magnetized Coaxial Ion Gun (MCIG) method as shown in Figure 1. This method realizes the generation of metallic thin film with the materials which have high-melting-point (e.g., Ti, Zr …). Generation methods for these materials had been limited to the ion beam assisted vacuum deposition. The optimization of gun operation and the initial experiment with composite material electrode have been successfully performed. Result of the scratch test (JIS R 3255) on an aluminum thin-film, which formed on a SiO_2 substrate with the newly proposed MCIG technique, indicates 4.2 times higher adherence strength compared to the conventional vacuum vapor deposition technique. The developed technique had been applied for a patent via NUBIC. (”Fast alloy film deposition method”, by Tomohiko Asai, Kaoru Suzuki, Nobuyuki Nishimiya, Mikio Takatsu, 2012.9.6 (JP2012-195690))
(Collaboration with Prof. K. Suzuki, Prof. N. Nishimiya and Prof. S. Masutani et al.)

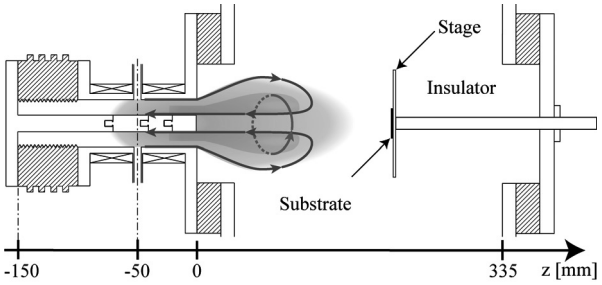

Figure 1. Schematic diagram of MCIG

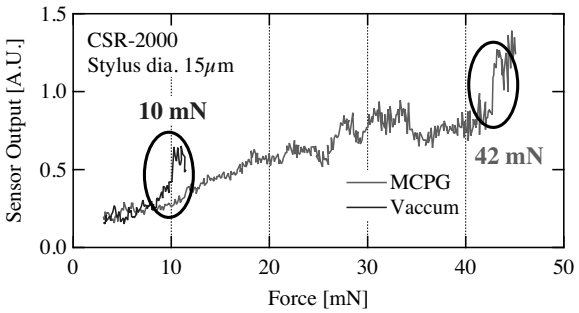

Figure 2. Result of the adherence strength test of aluminum thin-film on a SiO_2 substrate by methods of a vacuum vapor deposition and newly proposed MCIG technique

2. Development of MCIG with carbon electrode for hard DLC generation

Based on the MCIG technique which has been developed for the thin-film generation of high-melting point metals, experimental investigations of novel technique of diamond-like Carbon (DLC) generation has been initiated. Generally, DLC is generated by the discharge or spattering in the hydrocarbon gas atmosphere. Therefore, precise control of the hydrogen content in a DLC is difficult. The proposed method by utilizing MCIG with carbon electrode does not require hydrocarbon gas to generate DLC. Then the content of hydrogen is easily controlled by changing mixing ratio of

discharge gas. The functionality of DLC is generally depends on the hydrogen content and ion energy injected into substrate. The MCIG technique potentially controls both hydrogen contents and injection energy of carbon ion.
(Collaboration with Mr. M. Hiratsuka and Dr. H. Nakamori et al.)

Figure 3. LF jet for a medical applications

3. Application of LF Plasma jet for Medical Treatments

The atmospheric-pressure LF (Low Frequency) plasma jet has been investigated to apply for surface modification technique of e.g. CNT composite materials. The application of the LF jet for medical treatments has recently been initiated. The high energy electron and ions supplied by the LF jet have a potential to be a tool to control chemical balance of cells in addition to the direct effect of hot particles.

In this project, we are focusing on the application to the cancer treatment. The experimental device had been developed (Figure 3) and the initial experiments have been initiated.
(Collaboration with Prof. N. Fukuda, Dr. K. Fujiwara, Dr. K. Saito and Dr. H. Koguchi (AIST) et al.)

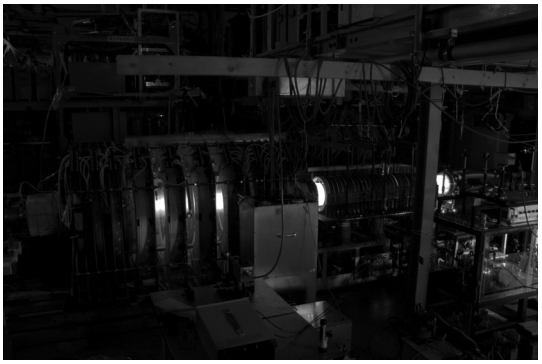

Figure 4. FAT device

4. High-efficiency method of muon catalyzed fusion

The muon catalyzed fusion (μCF) is one of the nuclear fusion reaction processes caused in a μ-atom. To improve the efficiency of μCF, innovative concept of fusion reactor design has been proposed and preliminary experiments on a super-Alfvénic translated FRC (Field-Reversed Configuration) plasma (Figure 4) have been initiated.

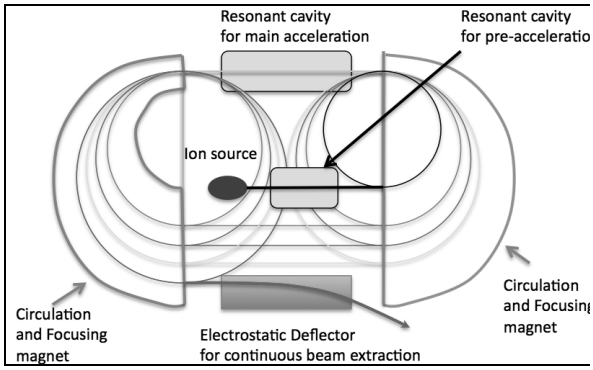

Figure 5. Schematic of FFAG accelerator for high energy hadron

The application of GeV-class hadron particles to new energy production by using nuclear fusion reactors has been discussed. The FFAG (Fixed Field Alternating Gradient) accelerator is an attractive candidate for this study because it is compact with small magnetic materials, and is capable to supply stable beam for DC-magnetic field operation, although the electric field of the acceleration rf-devices is low up to 100 kV/m due to the requirements for large aperture and for time-variation of rf frequency to adjust to the non-linear velocity of high-energy particles. We have studied to improve the FFAG accelerator by applying magnetic field configuration to main bending magnets, to satisfy isochronous condition and phase stability. Figure 5 shows the conceptual design of the new accelerator. Numerical investigation has been initiated to optimize the accelerator design for the application to μCF.
(Collaboration with Dr. E. Nakamura (KEK))

Imaging of Bionanomachines

Shigeru CHAEN
Nanomaterials and Nanodevice

In studies on bio-nanomachines, the conventional ensemble techniques have been used. However the ensemble of many bio-nanomachines does not represent the real view of the bio-molecule, because the individual reaction does not intrinsically synchronizes with each other. Studying single-molecule at a time is necessary for understanding the bio-nanomachine in action. Here we report studies on the biomolecular motor using the ordinary fluorescent imaging and the receptor protein on the biomembrane using the single-moecule fluorescent imaging technique.

1. Studies on the biomolecular motor using the ordinary fluorescent imaging technique.

In vitro motility assays using bipolar myosin thick filaments demonstrated that actin filaments were capable of moving in both directions along the myosin filament tracks. The movements, however, were slower in the direction leading away from the central bare zone than towards it. To understand the mechanism underlying these different direction-dependent motilities, we have examined the effects of temperature on the velocities of the bidirectional movements along reconstituted myosin filaments. The apparent activation energy of the movement away from the central bare zone was significantly higher (79 kJ/mol) than that of the movement toward the zone (44 kJ/mol). Given that the backward movement away from the central bare zone would cause the myosin heads to be constrained and the stiffness of the cross-bridges to increase, these results suggest that the elastic energy required for the cross-bridge transition is supplied by thermal fluctuations. （*Biochem. Biophys. Res. Commun. 2010, 396, 593-542*）.

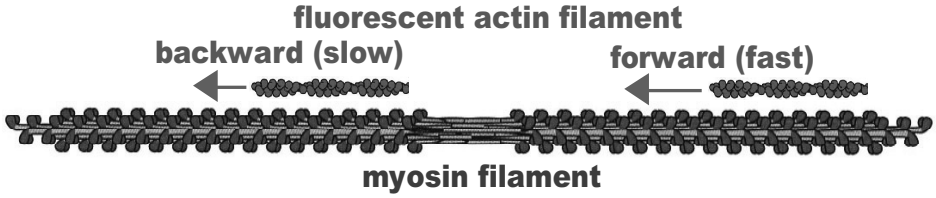

2. Imaging of ATP hydrolysis of bionanomachines.

As mentioned above, we have suggested that the backward movement causes the myosin heads to be constrained and increase in the energy required for the ADP release step by the findings that the thermal activation energy. In this study, in order to examine whether ADP release rate is slower in the backward than the forward movement, we constructed an assay system to estimate the ADP release rate from the displacement of fluorescent nucleotides bound to myosin heads by flash photolysis of caged ATP. Using the new assay system, we obtained that ADP release rate is slower in the backward than the forward movement (*BIOPHYSICS 2013, 9, 13-20*).

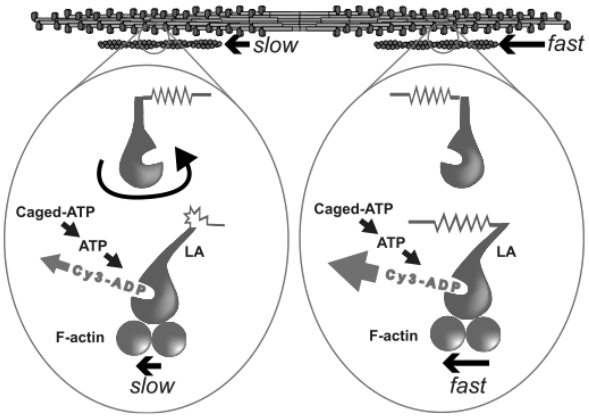

3. Studies on the receptor protein on the biomembrane using the single-moecule fluorescent imaging technique

Single molecule imaging technique has broken through the bottlenecking problem of optical resolution limit and provided a method to directly observe each single molecule by optical microscopy. Traditional epi-fluorescence microscopy can not identify faint fluorescence from a single molecule buried in enormous amount of background fluorescence. Evanescent field illumination method provides a device for drastically reducing background fluorescence and enables *in vitro* single molecule imaging of purified proteins. The method, however, has several problems to overcome in *in vivo* usage. Intense and heterogeneous distribution of autofluorescence in living cells or tissues is a deep-rooted obstacle to reduce background. Brownian motion of objective molecules bring about spaciotemporally ever-changing distribution of their fluorescence intensity. To surmount these difficulties, we have improved our microscopy system to accomplish high contrast imaging and investigated alternative fluorescent reagents instead of GFP. We have so far singled mPlum, a fluorescent protein, out for High S/N ratio and long lifetime of its chromophore. We intend to evaluate *in vivo* usage of mPlum. In practice, we conduct *in vivo* single molecule imaging of a fusion protein consisting of Plasma Membrane Targeting sequence (PMT) and mPlum expressed in living cells. PMT sequence makes it possible to place the fusion protein directly under plasma membrane.

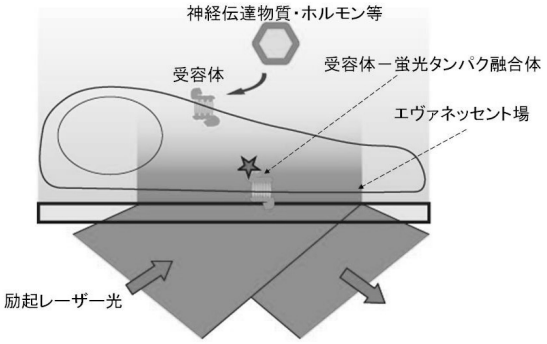

4. Development of a new wet cell using a carbon thin diaphragm to observe a living cell in aqueous solution with Scanning Electron Microscopy at nanometer resolution

In electron microscopy, transparency of specimens against a beam of electrons in TEM or intensity of secondary electrons and so on induced by an incident electron beam in SEM is translated into contrast. Any material surrounding a specimen, which prevents electron beam passing or detection of secondary electrons, obstructs to create an image. Hence, electron microscopy intrinsically requires high voltage electron beam irradiation of specimens and high vacuum under 10-4 Pa in the cell for specimens. Water in samples must be replaced with some resins or completely dried up. These conditions make it difficult to observe wet or living samples like enzymes retaining catalytic activities or living cells in aqueous solution. To image wet and living samples using electron microscopy at nanometer resolution, we are developing a new wet cell for SEM whereby living cells and enzymes can be maintained in aqueous solution. A carbon thin layer with thickness of 20 nm was made by vacuum evaporation. We applied it as a diaphragm withstanding a pressure gap for separating a specimen in solution at atmospheric pressure from high vacuum environment. Cells and enzymes were placed on its surface of the atmospheric side. They were imaged using SEM. The EM photographs show detailed structures of the cell membrane and the enzymes.

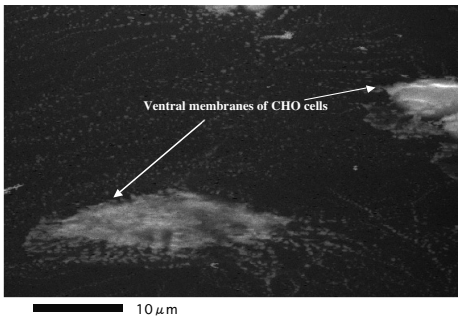

Drug discovery of pyrrole-imidazole (PI) polyamide by the chemical biology and Development of plasma medicine for cancer

Noboru FUKUDA, Jun IGARASHI, Kousuke SAITO

Medicine

1. Drug development of PI polyamide as practical medicines

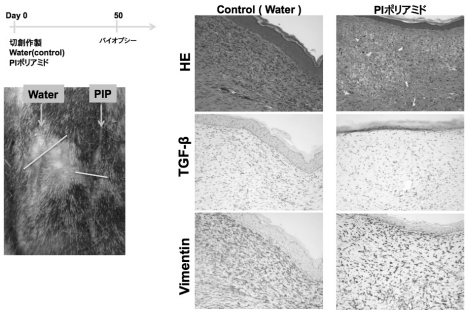

We confirmed that PI polyamide targeting human TGF-β1 **(**GB1101) is strongest to inhibit the expression of TGF-β1 mRNA in human- and marmoset-derived fibroblasts. We checked the combination of components of soluble materials and solutions for PI polyamides and found that Macrogol Ointment was most effective substrate to delivery the PI polyamide into skin. We examined effects of PI polyamides targeting human TGF-β1 on development of skin finrotic scar created in common marmosets and confirmed acual inhibition of the skin scar.

2. Development of the Nihon University original methodology inducing iPS cells using the PI polyamide targeting human TGF-β1

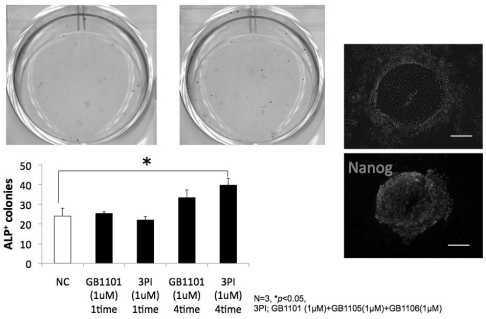

We examined the iPS-producing method establishment using proteolysis resistant cell-permeable proteins and the iniciation factor, TGF-β1 inhibitor, PI polyamide targeting human TGF-β1, Apigenin, TGF-β1 antagonist and Apigenin, and TGF-β1 and PI polyamide targeting human TGF-β1.

3. Development of plasma medicine for skin malignant melanoma

We started a project of the development of plasma medicine for skin malignant melanoma collaborating with the plasma team in College of Science and Technology. This plasma medicine targets the cancer stem cell with all trans retinoic acid to reduce the tolelance of radical oxygen species.

4. Drug development of cyclic PI polyamides

To verify the higher efficiency of biological activities of the cyclic PI polyamides, we have been carrying out the comparison between hairpin and cyclic PI polyamides with nine-ring or ten-ring this year. According to results of Real-Time PCR, cyclic PI polyamides targeted human TGF-β1 much more significantly than hairpin PI polyamides, indicating the cyclic PI polyamides maybe can be used as a new type of DNA-binding molecule with lower dose.

Single Photon Optoelectronics Devices

Hideomi HASHIBA
Nano-devices; Quantum information

Our research aims development of single photon optoelectronic devices. The research has focused on silicone/Au waveguides, CdSe colloidal quantum dots as single photon emitters for quantum information transport, two dimensional TiO_2 photonic crystals of low refractive index for solar cells, and single photon detectors for THz range on this project.

1. THz plasma excitations of quantum dots confined with potential barriers

One of the promising ways to perform single-photon counting of terahertz radiation consists in sensitive probing of plasma excitation in the electron gas upon photon absorption. We aimed to reveal appearance of plasma excitations under high ratio of incoming photons and at high temperature. Our device is assembled from a GaAs/AlGaAs quantum dot, electron reservoir and superconducting single-electron transistor. The quantum dot is isolated from the surrounding electron reservoir in such a way that when the excited plasma wave decays, an electron could tunnel off the dot to the reservoir. Plasma excitations of the QD arises with a formation of confinement potential barrier from the reservoir having resistances more than resistance quanta, and we revealed that appropriate shape of the barriers lowers dark counts by suppression of flow of hot electrons form the reservoir and reveals higher order excited states. The higher order excited states is expected to have the same plasma frequency of that of the first and shows a heat bath effect of the QD. The detector shows high noise equivalent power of ~10^{-19} $WHz^{-1/2}$. (1 paper, 1 lecture meeting, 2 posters)

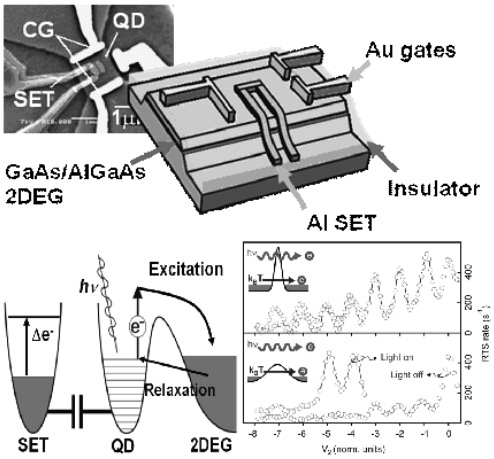

2. Development of fabrication technology of silicone waveguides, Au strip couplers and single photon emitters by one dimensionally aligned CdSe quantum dots

Semiconductor wave guides and photonic crystals are increasingly important in optoelectronic devices for quantum information technology. We study silicone wave guide devices with its third-order nonlinearities. Research of silicone wave guide devices on this project has been focused on development of simple fabrication method of the waveguides and we attained to develop concrete fabrication method for a Si waveguide of 320 nm wide and more than 1 mm long. The waveguide has small roughness of side-walls of less than 10 nm and accuracy of shape of the waveguide is restricted by our EBL that has field alignment precision of around 100 nm by auto-align mode or around 50 nm by manual align. This also affects for large sized structure such as Au stripe couplers. We also studied fabrication technique of arrays of colloidal quantum dots of 5 nm CdSe covered by silica. We attained 55 nm wide, 1.5 mm long array of the QD

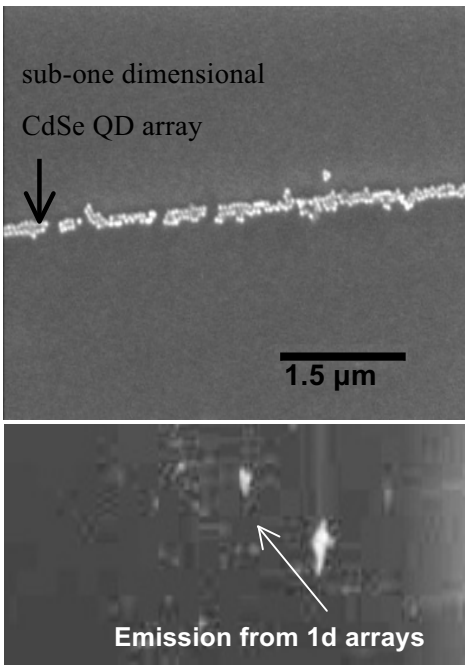

in sub-one dimensional shape. Evanescent coupling of the quantum dots to gold thin film of 37 nm was also confirmed. （1 poster）

3. Fabrication of titanium dioxide photonic crystals for dye sensitized solar cells

Titanium dioxide (TiO_2) has been draw attention for dye sensitized solar cells by its catalytic characteristics. Our aim is an experimental study of fabrication of fine structures, i.e. photonic crystals, of TiO_2 for solar cells to enhance its efficiency. A TiO_2 thin layer of 150 nm thick was grown on an FTO glass substrate with a fine patterned ZEP resist mask by a conventional RF magnetron sputter method with Ti target. We found that, during the deposition, keeping ratio of Ar-O_2 gas of 2:1 and the deposition ratio of around 0.5 Å/s ensures enough oxygen to form TiO_2 and low temperature to avoid deformation of fine pattern of the ZPU resist mask. Design of the fine patterns is photonic crystal structure of periodic zigzag slabs of 108 nm width, 608 nm in period. TiO_2 layers are white-transparent, amorphous, and those roughnesses are around 7 nm. Baking of TiO_2 fine structures.at 500 ^{o}C transforms TiO_2 from amorphous to rutile and anatase forms while keeping the same profile of the fine structures. Our new fabrication method can be one of a promising technique to optic devices on researches and industrial area. (2 papers, 1 poster)

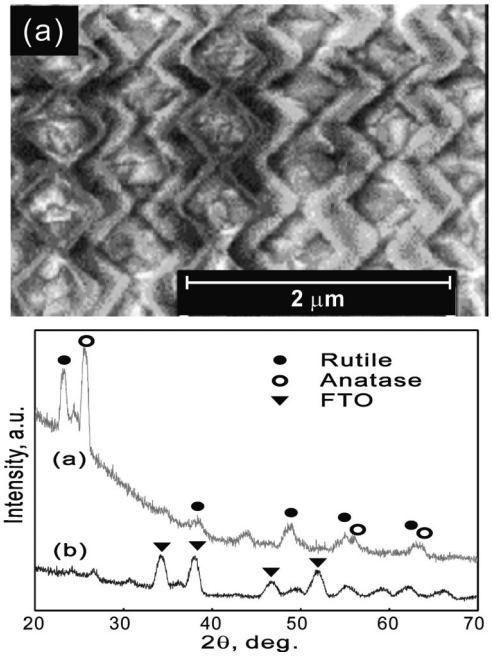

Preparation of Development of Materials for Intermediate Temperature Solid Oxide Fuel Cells with Nono-mixing process

Takuya HASHIMOTO
Energy Technology

Solid oxide fuel cells (SOFC) attract much interest due to high energy conversion efficiency and low emission of pollution gas. At present, operation temperature of SOFC is about 800-1000 ºC, which should be reduced to 600-800 ºC for practical application. In order to reduce operating temperature, new materials for cathode, electrolyte and anode which work at such a low temperature should be developed. In this study, potentials of the compounds listed below as new SOFC materials have been investigated. Improvement of property as SOFC materials has been examined by employing Pechini process as preparation method, which is expected as nano-mixing process. Fabrication and evaluation of new SOFC test cell combining these new materials are in progress.

1. Optimization of preparation method and sintering temperature of $LaNi_{0.6}Fe_{0.4}O_{3-\delta}$ as new cathode material and its stability at low oxygen partial pressures

$LaNi_{1-x}Fe_xO_{3-\delta}$, especially $LaNi_{0.6}Fe_{0.4}O_{3-\delta}$, attracted interest as new cathode material for SOFC due to low chemical reactivity with electrolyte material originating from absence of Sr. However, possibility of practical application was not verified enough because optimization of preparation conditions and evaluation of electrical property of $LaNi_{1-x}Fe_xO_{3-\delta}$ as cathode material had not been sufficiently carried out.

In this study, preparation of $LaNi_{1-x}Fe_xO_{3-\delta}$ with Pechini process, one of the solution mixing method, was examined in place of conventionally used solid state reaction process. Employing Pechini process, preparation temperature of $LaNi_{1-x}Fe_xO_{3-\delta}$ decreased, resulting in preparation of single phase specimens with high homogeneity and large Ni content originating from prevention of reduction of trivalent Ni (*Solid State Ionics* 2011). It was also clarified that sintering of $LaNi_{0.6}Fe_{0.4}O_{3-\delta}$ powder prepared by Pechini method at 1050 °C produced sintering body with density of 70 %, high specific surface area and homogeneous pore size distribution, which are ideal as cathode material (*J. Amer. Ceram. Soc.* 2012). Comparison of $LaNi_{0.6}Fe_{0.4}O_{3-\delta}$ sintering bodies prepared by other solution processes was also carried, indicating that Pechini process employed in this study was superior from the viewpoint of controllability of sintering density, specific surface area and homogeneity of pore size distribution (*Mater. Res. Bull.* 2013).

For practical application, electrical property under low oxygen partial pressure is also an important factor since cathode is exposed to low oxygen chemical potential under SOFC operation. Also, variations of crystal structure, mechanical property and so on by variation of oxygen partial pressures at high temperature due to generation of δ are inevitable information for practical application. It was revealed that δ of $LaNi_{0.6}Fe_{0.4}O_{3-\delta}$ at 300-700 °C under oxygen partial pressure of $1\text{-}10^{-4}$ atm was within 0.10±0.01. The concentration of oxide ion vacancy reached more than 3 % under SOFC operating conditions, suggesting that not only electrical conduction but also oxide ion diffusion in $LaNi_{0.6}Fe_{0.4}O_{3-\delta}$ was high. The smaller δ variation of $LaNi_{0.6}Fe_{0.4}O_{3-\delta}$ at SOFC operating conditions compared to other candidate cathode oxides indicated superior stability of $LaNi_{0.6}Fe_{0.4}O_{3-\delta}$ as cathode material. It was also clarified that electrical conductivity of $LaNi_{0.6}Fe_{0.4}O_{3-\delta}$ showed more than 130 $S{\cdot}cm^{-1}$ below 700 °C despite of oxygen partial pressure as low as 10^{-4} atm, indicating high potential of $LaNi_{0.6}Fe_{0.4}O_{3-\delta}$ as cathode material for SOFC (*ECS Transactions* 2013).

2. Preparation and evaluation of proton conductivity of $Ba_{1-x}Sr_xZr_{0.9}Y_{0.1}O_{3-\delta}$

At present, yttria stabilized ZrO_2, oxide ion conductor, has been employed as electrolyte material for

SOFC. For realization of enough oxide ion conductivity, temperature more than 900 ºC is necessary, which make the operation of SOFC at intermediate temperature impossible. In this study, development of new proton conducting oxide is examined since it has been regarded that light proton can be transferred at low temperature more easily than heavy oxide ion.

$SrZrO_3$ and $BaZrO_3$ with distorted perovskite structure attracted much interest as mother phase of proton conducting oxides. It was reported that oxide ion vacancy generated by partial Y^{3+} substitution for Zr^{4+} site played the important role for proton conduction. Although $BaZr_{1-x}Y_xO_{3-\delta}$ showed high proton conductivity, poor sintering property was severe problem for application. Sintering property of $SrZr_{1-x}Y_xO_{3-\delta}$ was high; however, three kinds of structural phase transition in $SrZr_{1-x}Y_xO_3$, which were absent in $BaZr_{1-x}Y_xO_{3-\delta}$, were problems for application. In this study, preparation and evaluation of property of $Ba_{1-x}Sr_xZr_{0.9}Y_{0.1}O_{3-\delta}$ was performed under speculation that it might have the both merits of $BaZr_{1-x}Y_xO_{3-\delta}$ and $SrZr_{1-x}Y_xO_3$. Employing Pechini process, single phase specimens with composition of $Ba_{1-x}Sr_xZr_{0.9}Y_{0.1}O_{3-\delta}$ were successfully prepared. It was revealed that $Ba_{0.6}Sr_{0.4}Zr_{0.9}Y_{0.1}O_{3-\delta}$ had superior sintering property and no first order structural phase transition from room temperature to 1200 ºC (*Thermochim. Acta* 2012, *IOP Conf. Series, Mater. Sci. and Eng*. 2011).

Electrical conductivity of dense $Ba_{0.6}Sr_{0.4}Zr_{0.9}Y_{0.1}O_{3-\delta}$ ceramics was measured either by dc four probe method or ac impedance method. It showed higher electrical conductivity than those of so far reported $BaZr_{1-x}Y_xO_{3-\delta}$ and $SrZr_{1-x}Y_xO_{3-\delta}$, indicating high potential as new proton conducting oxide (*Solid State Ionics* 2012). Ac impedance measurements of $Ba_{1-x}Sr_xZr_{0.9}Y_{0.1}O_{3-\delta}$ revealed that electrical conductivity of grain boundary improved with Sr substitution, showing correspondence with increase of sintering property with Sr substitution. Ac impedance measurement of $Ba_{0.6}Sr_{0.4}Zr_{0.9}Y_{0.1}O_{3-\delta}$ also showed that improvement of electrical conductivity at grain boundary was necessary for further improvement of proton conductivity in $Ba_{0.6}Sr_{0.4}Zr_{0.9}Y_{0.1}O_{3-\delta}$ system.

3. Trial for development of new SOFC using new materials

Since the high potential as proton conducting electrolyte material of $Ba_{0.6}Sr_{0.4}Zr_{0.9}Y_{0.1}O_{3-\delta}$ was demonstrated, fabrication of test cell using this material was examined. The single phase powder of $Ba_{0.6}Sr_{0.4}Zr_{0.9}Y_{0.1}O_{3-\delta}$ was prepared with Pechini process and the disk pellet with about 20 mm diameter was prepared with uniaxial pressing. After cold isostatic pressing (CIP), the pellet was sintered at 1500 ºC in air. The sintering density of obtained specimen was more than 95 %, which is sufficient for electrolyte of SOFC. After polishing surface as mirror, Pt paste was painted on the both surfaces and heat-treated for preparation of electrode. For gas sealing, ring shape pyrex glass was attached on the surface of the electrolyte and partially melted at 900 ºC for adherence to Al_2O_3 tube for fuel flow. Fig. 1 shows photograph of fabricated test cell. Adherences between electrolyte, electrode and gas sealant were confirmed with secondary electron microscope and gas flow test. At present, trial for electrical power generation at 500 ºC is in progress. Fabrication of test cell employing other electrode material is also in progress.

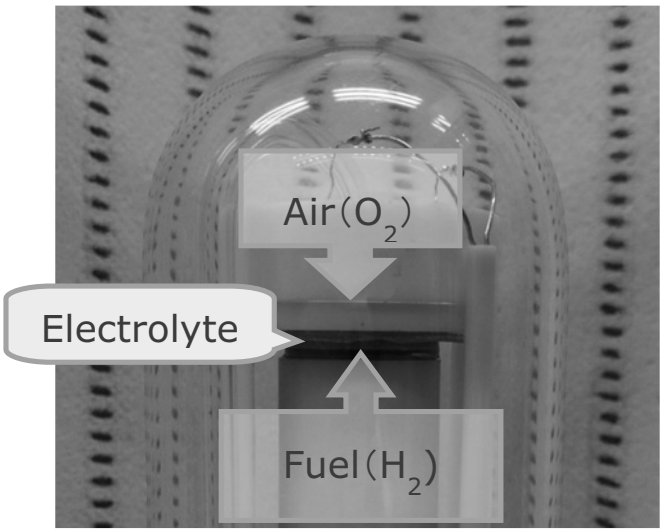

Fig. 1 Photograph of test cell.

Development of Poly(lactic acid)s Films as biopolymer, and Applications to New Material Field

Hiroki IKAKE
Supramolecular and Self-Assembly

In our group, the aim of development of poly(lactic acid)s (PLA) films as biopolymer with the high thermal- and mechanical- resistance. And then, the improved PLA was submitted to new material field.

1. Preparation of Poly(butylene terephthalate) Oriented Films by using High Magnetic Field

Orienting the crystalline domains of poly(L-lactide) (PLLA) in a specific direction would be one of excellent techniques to give various functions to PLLA. High Magnetic field was irradiated to semicrystalline PLLA, while annealing it at elevated temperatures according to a program. After holding PLLA at 185°C for 10minutes, it was held to raise the degree of crystallization at 140°C for various holding time. The oriented PLLA films were analyzed with small-angle X-ray scattering (SAXS). SAXS intensity of the oriented films was shown the cyclic behavior by an angle of 180 degree, and then it increased to a certain direction with increasing holding time. The aspect ratio (Y/X) of the maximum scattering vector was about 20%, the degree of orientation of the annealed film for 6hrs. These results of SAXS suggested that the degree of orientation of PLLA films was increased with increasing the crystal growth time under irradiated magnetic field at 10T.

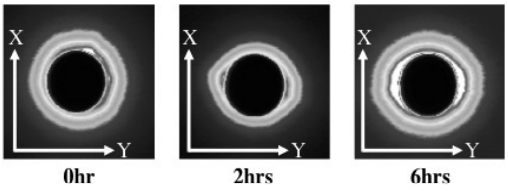

Fig.1 2D SAXS images of PLLA films heat treated for 0, 2, and 6hrs at 140°C under magnetic field at 10T.

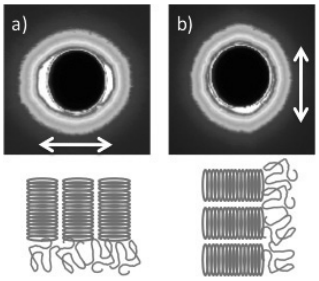

Fig.2 2D SAXS and drawn images of the heat treated PLLA films for 6hrs under magnetic field at 10T. Image a) azimuthal angle: 0° and Image b) 90°.a) azimuthal angle: 0° and Image b) 90°.

2. Effect of Cast-solvent on the Morphology of Mixtures of Stereoisomeric Poly(lactic acid)s

Semicrystalline films were prepared by casting chloroform (CHL), acetonitrile (ACN) or tetrahydrofuran (THF) solutions of a mixture (mix-poly(lactic acid) (PLA)) of poly(L-lactic acid) (PLLA) and poly(D-lactic acid) (PDLA) (Fig.3). All of the films involve stereocomplex crystals (sc-PLA) of PLLA and PDLA, but no crystals of PLLA or PDLA. The origin of the marked cast-solvent dependence of the morphology was studied by assuming that the structure of sc-PLA would be constructed by the balance of the interaction energy E_1 between the PLLA and PDLA chains in solution, and the interaction energy E_2 between PLLA or PDLA chains and solvent molecules. With the relation between E_1 and E_2, the scheme for the formation of sc-PLA was classified into two categories, Category-I and -II. In Category-I, the relation $E_1 > E_2$ holds over the entire concentration range, and in Category-II, the relation $E_1 < E_2$ holds over the range from dilute to moderate concentrations. As a result, the data indicate that Category-I would be proper when sc-PLA is formed by casting a THF or ACN solution of mix-PLA, and that Category-II would be proper when sc-PLA is formed by casting the CHL solution of mix-PLA.

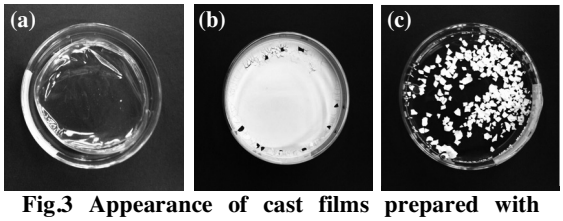

Fig.3 Appearance of cast films prepared with different cast solvent (a) mix-PLA(CHL), (b) mix-PLA(ACN), (c) mix-PLA(THF).

3. Effect of Cast-solvent on the Morphology of Mixtures of Stereoisomeric Poly(lactic acid)s

Two kinds of cast films, mix-PLA(DOX) film and mix-PLA(CHL) film, were prepared with an

equal-weight mixture of poly(D-lactic acid) (PDLA) and poly(L-lactic acid) (PLLA) by using 1,4-dioxane (DOX) or chloroform (CHL) as casting solvent, and it is clarified that mix-PLA(DOX) films are opaque, whereas mix-PLA(CHL) films are transparent (Fig.4). The relation between the transparency of these mix-PLA films and their morphology was studied by wide-angle X-ray diffraction, differential scanning calorimetry, and small-angle X-ray scattering. It is shown that the transparency does not depend on the crystallinity of sc-PLA, but on the macrostructure of the stereo-complex composed of PLLA and PDLA, sc-PLA, which is reflected in crystal size, lamella thickness and long period and their distribution. The transparency is lowered as the macrostructure becomes more disturbed or disordered. Moreover, it is shown that mix-PLA(CHL) films have good transmittance comparable to that of poly(methyl methacrylate) or polycarbonate and better thermal-resistance.

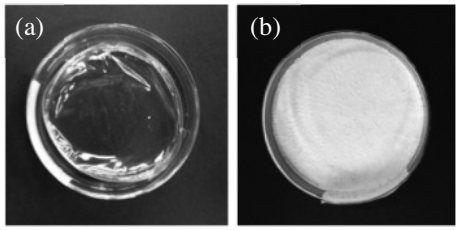

Fig. 4 Appearance of (a) mix-PLA(CHL) and (b) mix-PLA(DOX) films.

4. Morphology of Poly(lactic acid) Stereocomplex/Silica Hybrid Films

Poly(L-lactic acid) (PLLA) and poly(D-lactic acid) (PDLA) which were hybridized with inorganic substance, SiO_2, stereocomplex (sc-PLA/SiO_2) were prepared in order to improve the heat-resistance and mechanical properties of sc-PLA. Hybrid polymer films, sc-PLA(H)/SiO_2 and sc-PLA(C)/SiO_2, consisting of stereocomplex(sc) crystals of poly(lactic acid)s, which were prepared with solvent-cast method by addition of SiO_2 to a mixture of end-OH group modified poly(L-lactic acid) PLLA and poly(D-lactic acid) PDLA, and end-COOH group modified PLLA and PDLA, respectively. In the DSC curves of sc-PLA(H)/SiO_2, endothermic signal was observed at 235°C , whereas, in the DSC curves of sc-PLA(C)/SiO_2, broader endothermic signal was observed at 225~235°C. Moreover, in Lorentz - corrected SAXS pattern, the peak position of the hump for sc-PLA(H)/SiO_2 is located at smaller scattering vector q than that for sc-PLA(C)/SiO_2, where q is defined by $(4\pi)/\lambda \times \sin(\theta/2)$ and θ is scattering angle, and it was suggested that the morphology of film of these modified PLA hybrids is seriously influenced by variation in modification of end-groups of PLA chains. From dynamic viscoelastic measurement and thermo-gravimetric analysis, it was clarified that the hybrid thus prepared has 3-dimensional network structure, and higher heat-resistance and mechanical properties than those of sc-PLA.

5. Disintegration of poly(lactic acid)s stereocomplex by HFIP and its influence on alkaline hydrolysis

The present purpose of the study is to establish a useful method to disintegrate the structure of stereocomplex PLA(sc-PLA) of poly(L-lactic acid) (PLLA) and poly(D-lactic acid) (PDLA), and degrade the disintegrated chains. The sample powder of sc-PLA, which was prepared from an equal amount of PLLA and PDLA, was dissolved in 1,1,1,3,3,3-hexafluoroisopropanol in a concentration of 5 % and then the solution was treated with 1wt%NaOH *aq*. solution at different temperatures in order to find a suitable condition for the alkaline hydrolysis of sc-PLA. From SAXS data, it was shown that the radius of gyration of polymer chain increases as the standing time of the sample solution becomes longer, and the polymer chains are gradually set free from crystal of sc-PLA. From the Arrhenius plots for the sample, the rate constant of samples were increased with increasing the disintegration temperature.

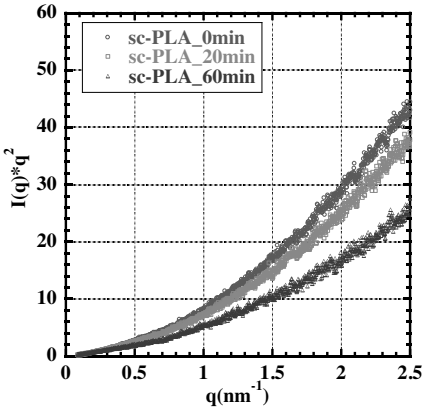

Fig.5 Kratky plots of sc-PLA in HFIP solution for various disintegration times.

Electronic properties of solid surfaces and adsorbed molecules

Hiroshi ISHIDA
Quantum Theory and Computation

1. Introduction

Recent progress in microfabrication techniques has enabled us to adsorb molecules at desired positions and to synthesize atomic monolayers in layer-by-layer fashion. Novel quantum phenomena occur in these nano-size systems as a result of energy-level discretization, symmetry lowering, change in the boundary condition of wave functions, and electron correlation effects. In the search for new functional materials and in the development of nano-size devices, the importance of theoretical calculations are ever increasing as a tool to analyze and predict experimental observations. In the present work, we conducted theoretical calculations of the electronic structure of solid surfaces and adsorbed molecules by placing emphasis on "the effects of strong electron correlations" and "the calculation of truly semi-infinite solid surfaces".

2. Electronic structure of the Metal/Mott insulator interfaces

An important question from a view point of device application is whether a device such as tunnel junctions works properly when a band insulator is replaced by a Mott insulator originating from strong electron correlations. As a theoretical technique to treat strongly correlated systems, dynamical mean-field theory (DMFT) is widely used. In particular, for bulk crystals, its extension to cluster type DMFT methods where electron correlations among neighboring atomic sites are taken into consideration are becoming standard. On the contrary, DMFT calculations for surface systems were so far restricted to those using the single-site approximation. In the present work, we applied the cluster DMFT technique to correlated surface and interface systems.

Fig. 1 shows the tight-binding model employed for calculating the metal/Mott insulator/metal interface, where an atom chain in the normal direction indicated by dashed lines was used as a unit of cluster for the cluster DMFT. We introduced the Hubbard type on-site Coulomb energy for the middle layers sandwiched between two non-interacting metal electrodes. It was demonstrated that the mehanism of the metal-to-insulator transition in the correlated layers as well as the tunneling conductance through them changes qualitatively from those obtained by the single site DMFT. Similarly, we calculated the electronic structure of a monolayer of the Mott insulator adsorbed on a semi-infinite non-interacting metal substrate. In doing so, we adopted a cluster consisting of 4 sites as a cluster for the cluster DMFT approach in order to consider interatomic electron correlations within the plane. While in the single DMFT, the overlayer becomes a Fermi liquid due to proximity effects to the metal substrate, it was found that the overlayer remains a non-Fermi liquid in the cluster DMFT calculation to much lower temperatures.

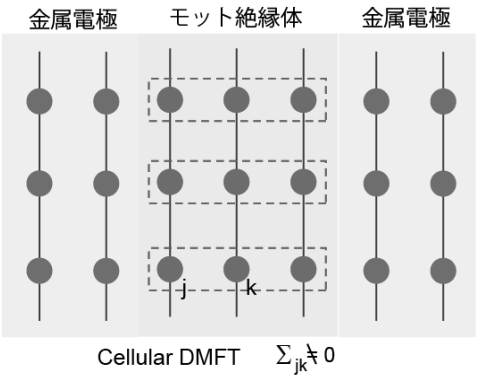

図 1

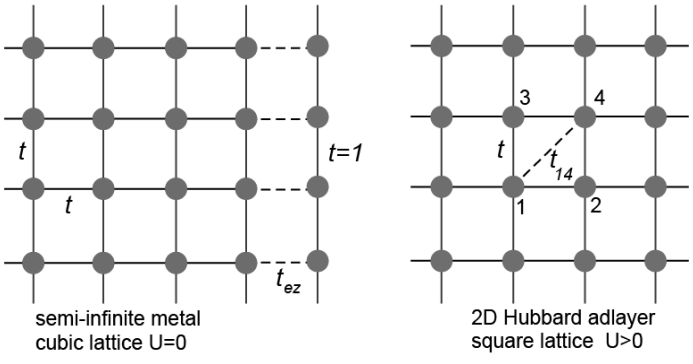

図 2

3. Coulomb blockade and Kondo effect in the Hubbard molecule

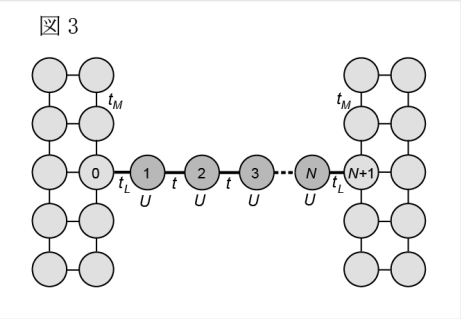

It has become possible to measure conductance of single molecules connected to metal electrodes. On the theory side, calculations of the ballistic conductance for molecules are reported based on the Landauer formula and density functional theory (DFT). The agreement between theory and experiment is not necessarily good as DFT cannot treat many body effects caused by strong Coulomb interactions between electrons in the molecules. To address this issue, we considered a *N*-site Hubbard molecule bridging two non-interacting semi-infinite metallic electrodes and calculated its electronic structure in the limit of the zero bias voltage by using the exact diagonalization technique. It was shown that our method can describe Coulomb blockade effects as well as the formation of Kondo resonance at low temperature originating from the coupling of localized spins in the molecule and conduction electrons in the electrodes.

4. Rashba effects in the localized surface bands of crystal surfaces

Spin-orbit interactions play an important role in the electronic structure of crystal surfaces. One example is the topologically protected surface states of topological insulators. Another is the spin polarization of localized surface bands observed in nonmagnetic materials such as Ag and Bi. The latter is called the Rashba effect. Previous first-principles calculation of the Rashba effect within DFT were performed by approximating crystal surfaces by thin slabs. However, the slab model is not suitable for the accurate description of localized surface states and surface resonances, since the bulk energy levels in the normal direction are discretized. We have incorporated the spin-orbit interaction term in our embedded Green's function program and performed first-principles DFT calculations of the Rashba effect for a number of truly semi-infinite surfaces. As an example, we show in Fig. 4 the calculated surface band structure of Au(111) and Bi/Ag(111) surfaces, where we plotted the intensity map of $\rho(\varepsilon, \boldsymbol{k})$, the *k*-resolved local density of states within a muffin-tin sphere of an outermost surface atom, as functions of the wave vector and one-electron energy. The dark regions correspond to the energy gaps of projected bulk energy bands. Bright lines in the energy gaps are the localized surface states. As the Kramers degeneracy is lifted at the surface due the lack of the space inversion symmetry, the surface bands become spin-polarized except for the the Γ point in surface Brillouin zone.

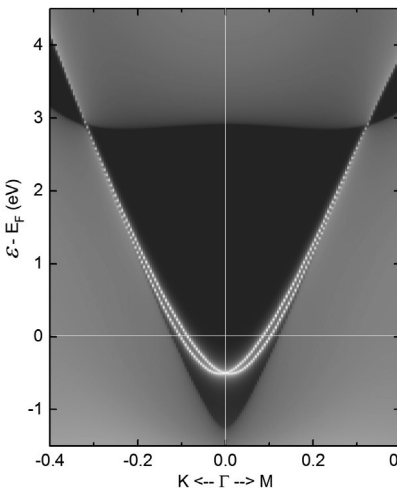

図4(a)　Au(111)表面のRashba効果

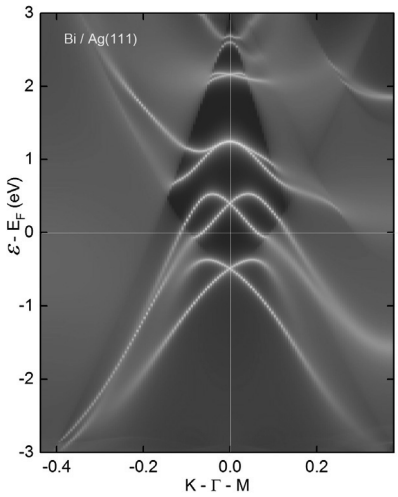

図4(b)　Bi/Ag(111)表面のRashba効果

References

(1) Ishida, H.; Liebsch, A.; *Phys. Rev. B* **2010**, *82*, 045107.
(2) Ishida, H.; Liebsch, A.; *Phys. Rev. B* **2012**, *85*, 045112.
(3) Ishida, H.; Liebsch, A.; *Phys. Rev. B* **2012**, 86, 205115.

Multi-functional and Highly Dense Devices by Fabrication and Control of Nanostructures

Nobuyuki IWATA
Nanomaterials and Nanodevices

The purpose of this study is to induce the giant magnetoelectric (ME) effect in superlattices using perovskite-related oxides and ferromagnetic metal/Cr_2O_3 heterostructures. In addition, the ferroelectric and ferromagnetic multiferroic property is expected in superlattices. For highly dense devices, the single-walled carbon nanotubes (SWNTs) with the features of the homogenious electric property, controlled growth position, and aligned growth orientation are fabricated at nm-scale using free electron laser (FEL) irradiation, treatment of substrates, and atomic arrangement of the substrate surface. The C_{60} multi-functional and flexible transistor is also expected by both of top-down and bottom-up techniques.

1. Multi-function in superlattices using perovskite-related oxides

The aim of our study is to synthesize the oxides superlattices with atomically sharp interface. The superlattices could be the quite low consumption magnetic devices controlled with electric field, and multifunctional, for example ferroelectric and ferromagnetic multiferroic devices. For the fabrication of the superlattices, highly refined and atomically controllable deposition technique arerequired. We developed the synthesis of highly dense targets and layer-by-layer growth technique, and carried out the detailed analysis of crystal structures for the superlattices. The materials used were ABO_3 (A=Ca,La, B=Fe,Mn) 、 $REMO_3$ (RE=La,Bi, M=Fe,$Fe_{1-x}Mn_x$). Although it is difficult to calcine the target with the density more than 95%, the targets of $LaFeO_3$(LFO) : 95.5% 、 $CaFeO_x$(CFO) : 96.4%、$BiFeO_3$(BFO) : 95.2%、 $BiFe_{1-x}Mn_xO_3$(BFMO) : 96.6% were able to be fabricated using the Pechini method by the collaboration research with Prof. Takuya Hashimoto. The superlattices were fabricated by the alternate stacking of the ABO_3 and $REMO_3$ using pulsed laser deposition method. High quality superlattices grew by a cube-on-cube manner demonstrated by a x-ray diffraction, reflection and reciprocal space mapping, where the superstructure satellite peaks and Laue oscillation were clearly observed. Decreasing temperature, magnetic interaction through the interface was developed expected in the illustration of the temperature and/or magnetic field dependence of an in-plain sheet resistance and a Hall resistance. In Fig.1 (a) surface morphology and (b) reflection high energy electron diffraction (RHEED) image of the [CFO/BFMO] superlattice with the thickness of 80 nm are illustrated. The surface and the RHEED image showed step-terraces structure and streak pattern, indicating two-dimensional flat surface at the atomic level. Figure 2 shows saturation magnetization as a function temperature. The closed squares are measured data. The solid line was illustrated using Brillouin function with the Curie temperature of 450K. Inset figures are magnetization curves at 300K and 10K. The magnitude per $Fe_{1-x}Mn_x$ at 300K was

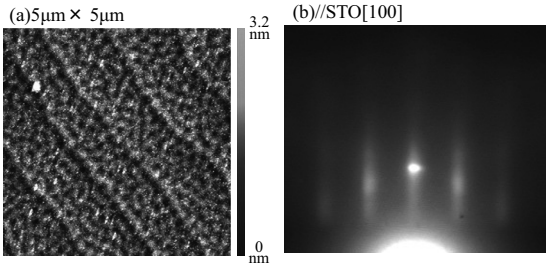

Fig.1 : (a) surface image and (b) RHEED pattern of [CFO/BFMO] superlattice.

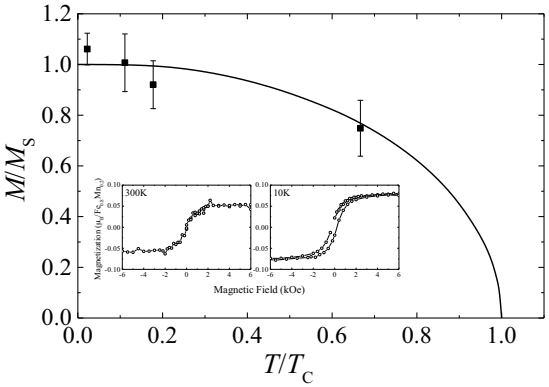

Fig.2 : Saturation Magnetization vs. temperature of [CFO/BFMO] superlattices. The symbols of ■ are measured data. The M_S is saturation magnetization at 0K. The T_C is Curie temperature. The solid line is illustrated using Brillouin function.

$0.055\mu_B$, which is approximately four times larger than that of bulk. Fabricating superlattice with the atomically smooth interface developed artificially the magnetic property.

2. Fabrication of Highly Dense Transistor using Single-Walled Carbon Nanotubes

For the supreme fine field effect transistor (FET) with nm order in size, the single-walled carbon nanotubes (SWNTs) were synthesized by a chemical vapor deposition (CVD) method using ethanol as a feeding gas. The grown SWNTs are expected to have the features of homogeneous semiconducting property, which is correspondence with the homogeneous chirality, controlled growth position, and anisotropic alignment. Those features are realized by the irradiation of the free electron laser (FEL) during the CVD process, the surface treatment, and the growth on the atomic arrangement surface of the single crystal substrate. The FEL is composed of micro-pulses with the full width at half maximum of hundreds femto-second, and the wavelength is variable from 0.3 to 6μm. Those distinctions make it possible to grow the chirality controlled SWNTs without a collapse of bonding by thermal heating. The surface treatment is able to decide the deposition position of the catalysts, resulting in the growth position control of the SWNTs.

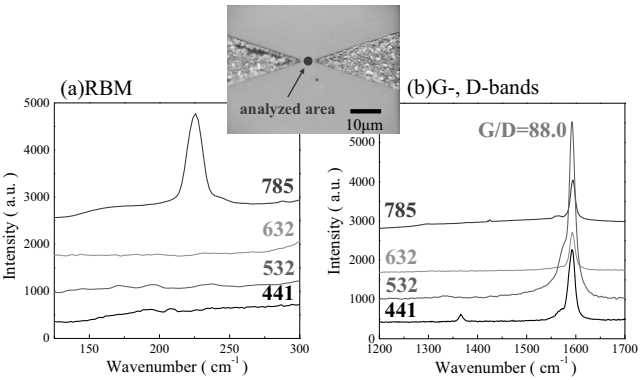

Fig.3 : Raman spectra of (a) RBM and (b) G and D peaks for SWNTs grown between electrodes with 800nm-FEL irradiation. The notation of the 441,532,632,785 indicate wavelength of the excitation laser used in Raman measurement. The unit is nm. The hydrophilic treatment was done only the area between electrodes..

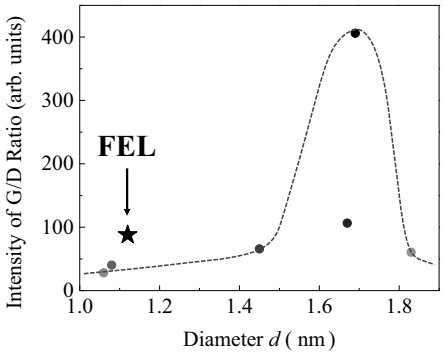

Fig.4 : The value of G/D ratio of the SWNTs grown without FEL as a function of the SWNTs diameter. The symbol of ★ indicates the data of the SWNTs grown with 800nm-FEL irradiation.

The alignment growth of the bundled SWNTs was grown on sapphire substrate with the length of approximately 500 nm. Figure 3 shows the Raman spectra of the SWNTs grown with the 800nm-FEL irradiation. The spectra were detected at the region with 1μm in diameter between electrodes described in the inset image. The radial breathing mode (RBM) and D- and G-peaks were illustrated in (a) and (b), respectively. The RBM peak appeared only in the spectrum detected using 785 nm excitation laser with the G/D ratio of 88. At the area 10μm away from the area between the electrodes, the RBM as well as G- and D-peaks did not appear. Those results reveal that the high quality SWNTs grow with the semiconducting property, where the chirality possibility is reduced at only four types of (14,0), (13,2), (10,6) and (5,7). The FEL irradiation is quite effective to control and reduce the possibility of the chirality, considering that the metal and semiconducting mixed SWNTs with the chirality more than 30 grow when the CVD process is carried out for the SWNTs growth without the FEL irradiation. The surface treatment is also effective to control the growth position. Figure 4 shows the G/D ratio as a function of the SWNTs diameter. The highest quality was the SWNTs with 1.7 nm in diameter showing the value more than 400 in the G/D ratio. With the same CVD condition using the 800nm-FEL irradiation, the growth was restricted in the SWNTs with the diameter of 1.1 nm, and the quality was also developed demonstrated by the increase of the value of G/D ratio. It is concluded that the synthesis position and the chirality control are achieved simultaneously by the hydrophilic surface treatment between electrodes and the FEL irradiation. In particular the chirality control of the SWNTs during the CVD process is successfully carried out at the first time in the world.

Development for Application of Cluster and Molecular Aggregating

Ken JUDAI
Nanomaterials and Nanodevices

The construction of nano architectures by self-assembly of molecules requires well-understanding on molecular nature and complete control of molecular interaction. In this study, silver acetylide and acetylsalicylic acid were investigated as a model compound for a nano helix, which is important bio architecture such as DNA double helix and α-helix of protein. Besides, a novel carbon materials preparation method is also established. Copper acetylide self-assembles into nanowires, and its nanostructures are suitable to prepare new carbon materials.

1. Origin of Nano Helix by Molecular Aggregates

Silver tolylacetylide does not have chiral center carbon, and is an achiral molecule. However, it turned out that twisted nano ribbon structures, chiral helices, were generated by recrystallization in solution phase. We have investigated for the chiral origin how the achiral molecules aggregate to the chiral nano helical structure. The solvent for recrystallization was changed between methanol, ethanol, 1-propanol, and 1-butanol systematically. Fast recrystallization solvent such as methanol was observed as twisted nanoribbon structures, and the other side, slower solvent such as 1-butanol was as straight non-twisted nanoribbon structures. Helical and non-helical structures can be controlled by recrystallization solvent. Crystallization speed, in other words, quality of crystal by crystallization kinetics is important for twisted nanoribbon structure (*J. Nanosci.* 2013).

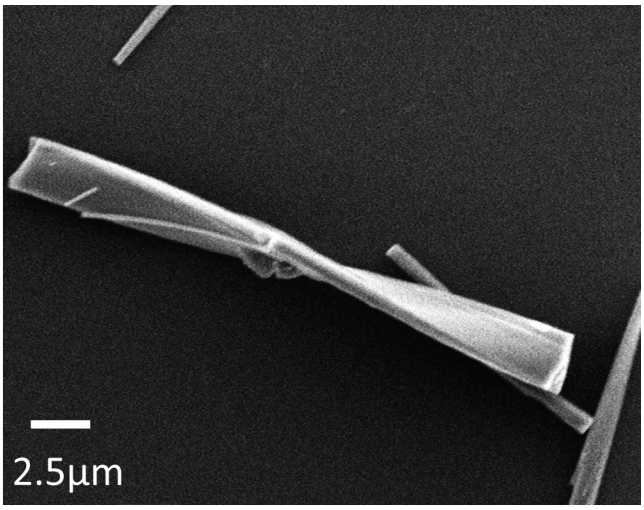

Figure 1 SEM image of silver tolylacetylide.

An additional experiment showed that light irradiation made solution color changing to red and enhancement of twisting nanoribbon structures. The light irradiation produced decomposition of silver acetylide and dimerization reaction. The dimerization of acetylide indicated red color, and displacement of crystal by the decomposed compounds enhanced crystal tension and twisting.

Acetylsalicylic acid is a famous and well-known molecule. It does not have chiral center carbon, and it is an achiral molecule. However, it was recently found that the crystal structures of acetylsalicylic acid are also helically rotated. 5 mg of acetylsalicylic acid was put on a microscope slide and was covered with a covered slip. It was melted by a hot plate at 135 °C temperature, and was subsequently cooled down by room temperature. Figure 2 indicates a polarized-light microscope image of the recrystallization of acetylsalicylic acid with the crossed Nicole prism. The periodical structures with 500 μm pitch were observed. The light transmission is depended upon the difference of refraction indices by birefringence and thickness of crystal in the polarization microscope. The thickness of the crystal could not alter periodically because the position of covering glass slip determined the thickness. The difference of birefringence was only solution to explain the microscopic image. Taking into account only acetylsalicylic acid used, the recrystallization of acetylsalicylic acid should turn and rotate in the crystal growth. In short, the acetylsalicylic acid crystal is growing with twisting and rotating as same as silver acetylide molecules. The periodic polarization microscope

image can be explained by every single or half turn of crystal surface corresponding to the pitch of birefringence change.

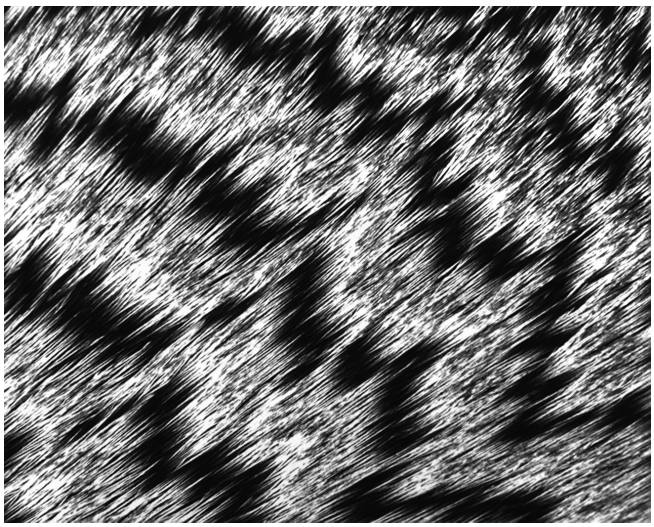

Figure 2 Polarization microscope of acetylsalicylic acid

Acetylsalicylic acid is famous molecules and the crystal structure has been also known. The powder x-ray diffraction was measured by the sample of periodically twisting crystal. All the diffracted peaks could be assigned by the reported crystal structure of acetylsalicylic acid with $P2_1/c$ space group symmetry. However, the space group of $P2_1/c$ has an inversion center, and it was allowed for packing achiral molecules only. Actually the crystal space group symmetry indicated no information on righ-handed or left-handed helical crystals. We should study further the origin of chiral nano helix from the point of symmetry.

2. New Amorphous Carbon Preparation Method by Nano Structures

Copper acetylide and silver acetylide are famous as explosive compounds. However, when the explosive crystal was downsized into nano scale, the explosive nature would be eliminated by much less thermal conductance preventing from explosive chain reactions. This nano less-explosive character was applied to new noble carbon material production.

Generally amorphous carbon was generated by high temperature exposing of organic compound for carbonization. The high temperature for carbonization makes crystallization to graphite partially. In this method, the carbonization reaction can proceed in lower temperature because of chemical reactive nature of copper acetylide, and genuine amorphous carbon materials can be generated.

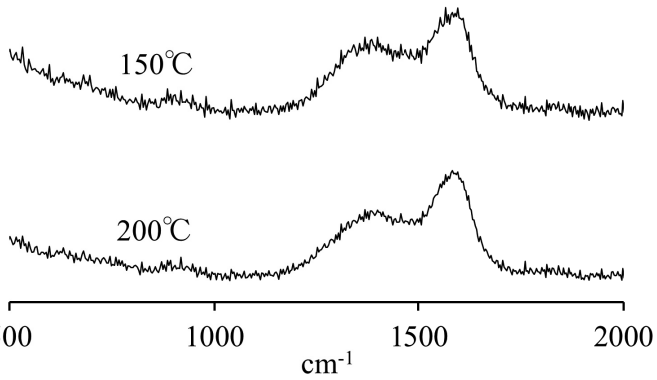

Figure 3 Raman spectra from nano copper acetylide

Figure 3 shows Raman spectra of new carbon materials generated by low temperature carbonization of copper acetylide nano compounds and acid treatment for removal of copper element. In this year, the existed spectrometer and newly resourced optical parts such as Raman special filters were assembled in order to measure Raman spectroscopy in our laboratory. Around 1600 cm^{-1} peaks assigned to G-band were observed as same as typical carbon materials, and also about 1380 cm^{-1} peaks assigned to D-band. The Raman spectra in this method showed extremely broader peaks than those of typical carbon materials, and the G-band and the D-band were deeply overlapped. These specific Raman peaks were observed by only diamond-like-carbon materials.

A novel model of onset breast cancer by implanting mature adipocyte-derived dedifferentiated fat (DFAT) cells

Koichiro KANO
Medicine

Animal models of cancer, particularly mouse models of cancer, are commonly used to study tumor biology and develop new approaches to conquering human cancer. Previous research in modeling cancer in laboratory animals, especially experimental mice, has advanced tremendously our insights into the biology of cancer. Our goal is to make a novel model of onset breast cancer implanting mature adipocyte-derived dedifferentiated fat (DFAT) cells.

1. Mature adipocytes derived DFAT cells can transdifferentiate into mammary epithelial cells and/or myoepithlial cells in vivo

After birth, the mammary gland is primary composed of adipocytes and a limited the epithelial ductal network. But during pregnancy, the epithelium expands and invades the surrounding fat pad, whereas apparent reduction of cell number and diminution of the cell size is observed on adipocytes. After weaning, the decrease of mammary epithelium takes place concomitant with the repopulation of the mammary fat pad with adipocytes. The mechanism of interacting capacity between epithelial cells and adipocytes is not clear. Here we show that stromal adipocytes in the mammary gland are necessary to the formation of mammary gland. We transplanted wild-type mammary gland into the fad pad of GFP transgenic mouse. The end buds of expanded mammary glands were expressed GFP. In contrast, less expression were detected at GFP mammary glands in wild-type fat pad. Sectioning demonstrated that transplanted and normally formed mammary gland from the wild-type in the cleared fat pad of the GFP transgenic female mouse, alveoli were composed of transplanted epithelial cells and stromal cells, surrounding epithelium. At the pregnancy and lactation, transplanted stromal adipocytes formed functional alveoli-like structures with expressing the epithelial markers and secreted abundant intracellular lipids into the lumen. Our studies indicate that stromal adipocytes of the mammary gland are important not only as a stroma, but as a composition, directly participate, in the development of the mammary glands.

We have previously reported that the establishment of a preadipocyte cell line derived from dedifferentiated mature adipocytes of GFP transgenic mice using ceiling culture. These cells possess most of characteristics of preadipocytes in vitro and in vivo, and we called these cells dedifferentiated fat (DFAT) cells. Moreover DFAT cells can trans-differentiate into mesenchymal cell lineages (osteoblasts, chondrocytes and endothelial cells) in vitro and in vivo. Here we show the first report that DFAT cells derived from mesoderm trans-differentiation into ectoderm-derived mammary epithelial cells and/or myoepithelial cells in vivo. We implanted DFAT cells into mammary anlagen-free adipose tissue of wild-type female mice, and then recipient female mice mated with male mice. At day 5 post partum, DFAT cells could not form a functional mammary gland. When DFAT cells were implanted into normal mammary adipose

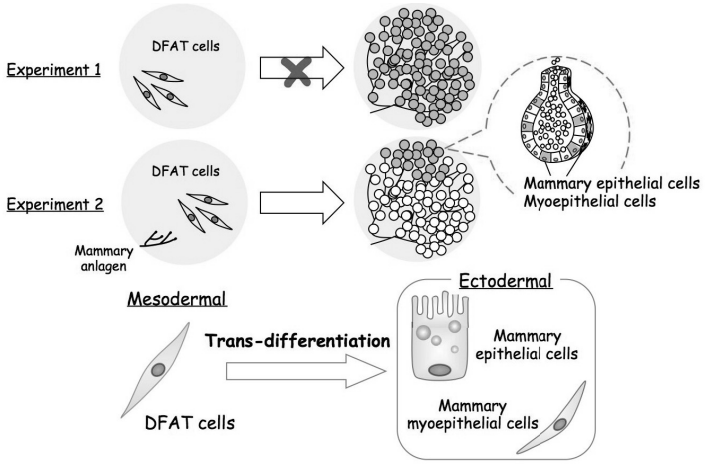

DFAT cells can trans-differentiate into mammary epithelial cells and/or myoepithelial cells in vivo through interaction with mammary anlagen

tissue, a number of GFP positive cells were detected in mammary alveoli throughout tissues. Additionally, double immunofluorescent staining showed that a number of GFP positive cells were positive for the epithelial cell markers E-cadherin, Keratin18 and/or the myoepithelial cell marker aSMA. These findings indicate that DFAT cells derived from mesoderm can trans-differentiation into ectoderm-derived mammary epithelial cells and/or myoepithelial cells through interaction with mammary anlagen in vivo.

2. Actin cytoskelton dynamics control adipocyte differentiation via regulation of MKL1

The hallmark of adipogenesis process is the dramatic alteration in actin cytoskelton as the structure of filamentous actin is converted from stress fibers to cortical actin. Here, we report that actin cytoskelton dynamics act as a trigger of adipocyte differentiation. Actin cytoskelton remodeling was immediately caused via the down-regulation of RhoA/ROCK signaling, which is a prominent regulator of cytoskeletal dynamics, and this actin remodeling was required for a master regulator PPARγ expression and adipocyte differentiation. Also it was found that the cellular G-actin levels were rapidly elevated depending on adipocyte differentiation, and increasing G-actin caused adipogenesis by preventing nuclear translocation of MKL1, which is a transcriptional co-activator. Moreover, we revealed that MKL1 expression was reduced during adipogenesis, and further only knockdown of MKL1 could trigger adipocyte differentiation. Besides, PPARγ was closely involved in the down-regulation of MKL1 in a positive feedback manner. Our findings provide new insights to the regulatory mechanism of adipocyte differentiation that actin cytoskelton dynamics control adipocyte differentiation via regulation of MKL1, and that MKL1 is a novel repressive regulator of adipocyte differentiation.

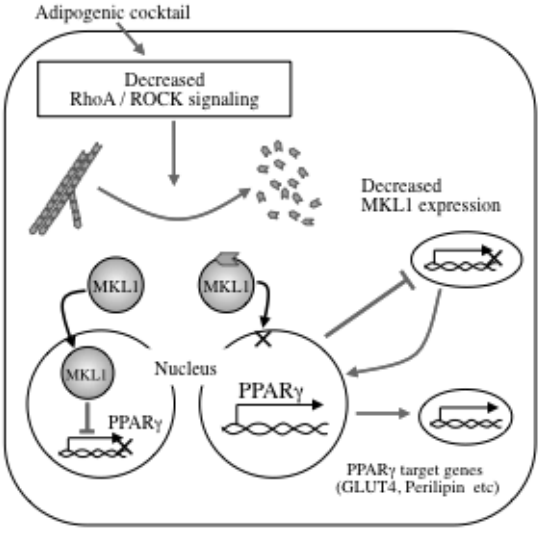

Novel model for the regulatory mechanism of adipocyte differentiation that actin stress fiber disruption triggers adipocyte differentiation via regulation of MKL1.

Anti-tumor effect of pyrrole-imidazole polyamide targeting *KCNQ1OT1* gene as new therapeutic agent

Tsugumichi KOSHINAGA

Medicine

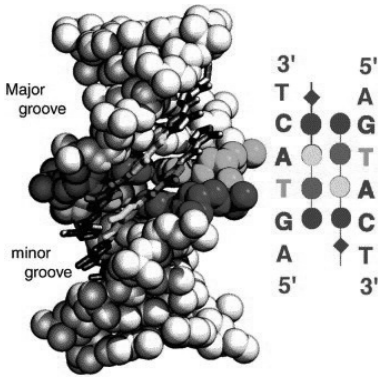

Beckwith-Wiedemann syndrome (BWS) is a human imprinting disorder with a variable phenotype, including the major features like omphalocele, pre- and postnatal overgrowth and macroglossia. Around 10% of BWS patients develop embryonal tumor (Wilm's tumor, Hepatoblastomoa). It has been known that BWS is associated with epigenetic alterations in two imprinting control region, KvDMR and H19DMR, on chromosome 11p15.5. Genomic alteration in KvDMR regions, such as aberrant methylation, deletion of gene and paternal uniparent disomy, lead to overexpression of *KCNQ1OT1* gene, which is non-coding RNA and suppress circumjacent genes in *cis*. In normal status, *KCNQ1OT1* promoter region of maternal allele is de-methylated, but of paternal allele is methylated. De-methylation of *KCNQ1OT1* promoter region in maternal allele make overexpression of *KCNQ1OT1* gene. Expression of tumor suppressor gene *KIP2* is suppressed by *KCNQ1OT1*, and de-methylation of *KCNQ1OT1* promoter region accompanied with down-regulation of *KIP2* has been reported in colorectal cancer, lung cancer, and other adult cancer. Based on these facts, we hypothesize that suppression of *KCNQ1OT1* gene could show anti-tumor effect. So, we have been tried to develop chemical compounds suppressing this gene.

Pyrrole-Imidazole polyamides (PIP) are small synthetic chemicals composed of the aromatic amino acids N-methylpyrrole (Py) and N-methylimidazole (Im). A combination of PI polyamides recognized the specific DNA base pairs, (Im/Py, Py/Im and Py/Py pairs bind to G-C, C-G, and A-T/T-A, respectively). A concatenation of these pairs made it possible to bind to a variety of specific DNA sequences, and suppressed the transcription of their target genes by competitive inhibition of the binding of transcription factors. Since PIPs were efficiently delivered to nuclei of several tissues without any specific drug-delivery systems, they can be powerful tools to develop gene-specific silencers. We generated PIPs h-CCAAT1 (PI-1) and h-CCAAT3 (PI-3) targeting promoter region of *KCNQ1OT1* gene and investigated their anti-tumor effect.

h-CCAAT-1 (PI-1)

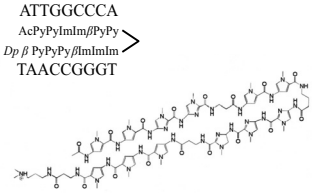

h-CCAAT-3 (PI-3)

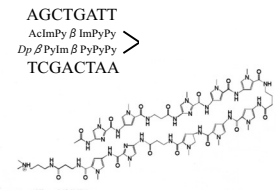

It was clearly shown by real-time PCR that the expression level of *KCNQ1OT1* was significantly reduced in human BWS fibroblast cell line BWS6 and BWS9 treated with both PI-1 and PI-3, compared to control cells ($P<0.05$). Similar result was found in Wilm's tumor cell line G401, which has de-methylated CpG island (CpGi) on

KCNQ1OT1 promoter and shows up-regulated expression of this gene. In addition, induction of KIP2 protein in G401 cells after the combined treatment with PI-1 and PI-3 was detected by western blotting. When the effect of the PIPs on cell viability was tested by WST8 assay, G401 cells treated with the both PIPs showed significantly lower number of living cells compared to that in the control cells. Since it has been reported that KIP2 is involved in the induction of apoptosis via mitochondria pathway, we examine the cells by using apoptosis marker. In the Fluorescence-activated cell sorting analysis, we found the higher number of cells undergoing apoptosis in the PIPs treated group than in the control group. Taken together, our current data strongly suggested that the combined treatment with PI-1 and PI-3 induced apoptosis in the Wilm' tumor cells by suppressing *KCNQ1OT1* expression, followed by the up-regulation of KIP2 protein.

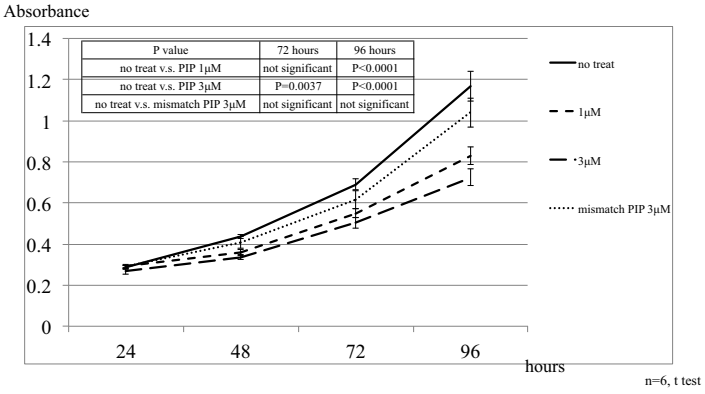

P value	72 hours	96 hours
no treat v.s. PIP 1μM	not significant	P<0.0001
no treat v.s. PIP 3μM	P=0.0037	P<0.0001
no treat v.s. mismatch PIP 3μM	not significant	not significant

Based on these results, we believe that the PIPs targeting *KCNQ1OT1* gene have possibility to be new therapeutic agents for tumor with de-methylated CpGi on *KCNQ1OT1* promoter.

Experimental Studies for Quantum Memory using Neutral Atoms

Takeshi KUWAMOTO
Quantum Information Group

Quantum information processing is hoped very much as a next-generation information, communication and computer technology. Quantum memory is indispensable and keystone for constructing scalable quantum processing systems. Our aim in this project is establishing the basic technique for materializing the quantum memory using neutral atoms. We especially intend to store the quantum entangled states. Our scheme is (1) generation of orthogonally polarized photon pairs resonantly coupled with ^{87}Rb atoms, (2) construction of high performance light storage system using electromagnetically induced transparency phenomena and (3) storage of quantum entangled states with unified two systems.

1. Generation of orthogonally polarized photon pairs

Quantum entanglement states are made up of orthogonally polarized photon pairs. Atomic sample we use is ^{87}Rb atom, and its transition wavelength for photon storage is 795 nm with linewidth of 6 MHz. Therefore, we have to first prepare the orthogonally polarized photon pairs which met above requirements. In order to obtain the required photon pairs, we performed following R&D.

Orthogonally polarized photon pairs with 795-nm wavelength were produced by a parametric down conversion which was brought about by injecting a 397.5-nm-wavelength pump laser into 10-mm-length nonlinear optical crystal (type II PPKTP). The pump laser was obtained by pumping a type I PPKTP crystal placed in a bow-tie type optical resonator with a 60-mW power, 795-nm-wavelength laser. Obtained power of the 397.5-nm pump laser was 6 mW, and this value was 3 times larger than the case without resonator.

In general, orthogonally polarized photons immediately after the type II PPKTP have the frequency expansion of THz order. Since the bandwidth of photons coupled with atoms is several MHz, this wide spread of frequency have to be narrowed. We utilized optical interference filters and etalons to obtain the narrow-bandwidth orthogonally polarized photons.

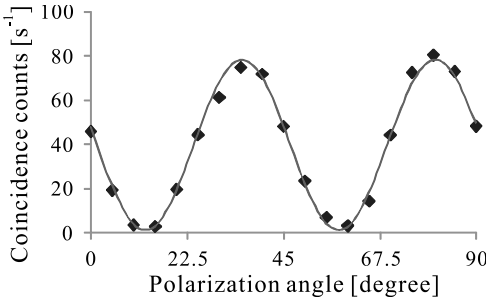

Fig. 1. Two-photon interference of orthogonally polarized photons.

Figure 1 shows result of two-photon interference measurement of generated orthogonally polarized photons. This measurement is performed to estimate the quantum property and quality of photons. The obtained visibility was 97.4%. This result shows that generated orthogonally polarized photons satisfy a demand as the quantum light source.

We measured the absorption of the generated photons by ^{87}Rb atoms enclosed in grass cell in order to confirm the frequency extent of photons. Figure 2 shows the absorption rate of photons as a function of atomic sample temperature. At the temperature of 95°C, 97% of photons were absorbed. This means that the frequency broadening of photon is about 500 MHz.

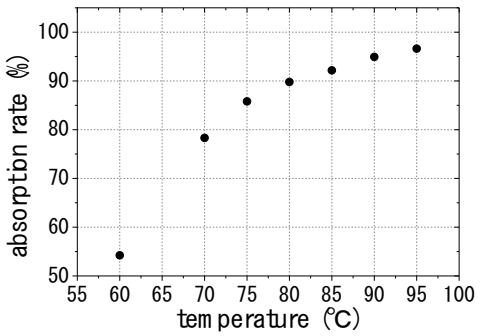

Fig. 2. Absorption rate of generated orthogonally polarized photons by ^{87}Rb atoms as a function of atom temperature.

2. Light Storage system

The phenomenon called electromagnetically induced transparency is used to store the light in a neutral atomic sample. For this phenomenon, when two different resonance lights are shined to three level atoms, one of light (probe light) passes thorough the sample without any interaction. That is, the atomic sample is transparent medium for the probe light. Moreover, by controlling the intensity of another light (control light), the probe light can be stored in atoms. In this study, we used ^{87}Rb atoms enclosed in grass cell as the sample, because of the abundant knowledge of its properties.

As probe and control light source, two external cavity diode lasers were used. The frequency fluctuation of control laser was controlled by a frequency locking system using Rb sample, and suppressed to be less than 1 MHz. The frequency of probe laser was controlled by the optical phase-lock with the beat signal between the probe and control lasers such that the frequency difference between two lasers agrees with that between the two low-lying atomic-energy levels. The probe laser beam was converted into a 5-μs-width gaussian pulse with an acousto-optic modulator. Rb sample grass cell was placed in a threefold magnetic shield and its temperature was controlled with a heater using hot-water.

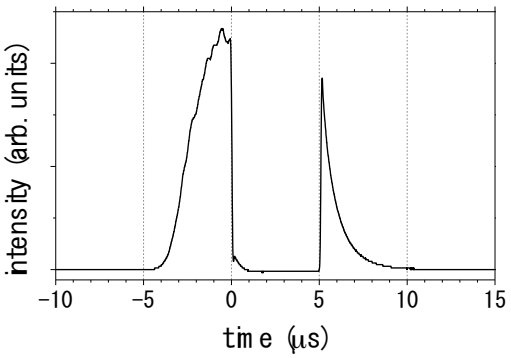

Fig. 3. Result of storage and retrieval experiment for laser pulse. The right peak corresponds to the retrieved light pulse after 5-μs storage.

The probe and control laser beams were coaxially propageted and injected into Rb grass cell. By suddenly switching off the control laser light, the probe light pulse was stored in the atomic sample. Figure 3 shows an example of the results of light storage experiment for the storage time of 5 μs. The efficiency of retrieved light pulse was 85%. This value means that we prepared sufficiently high-performance experimental system for light storage.

We investigated the storage of extremely weak coherent light pulses, because the intensity of orthogonally polarized photons would be very weak. Figure 4 shows the result of light storage experiment for the 2.6-nW probe laser power. In this case, the retrieved signal was not confirmed. This means that the storage and retrieval of orthogonally polarized photons using current our system is difficult.

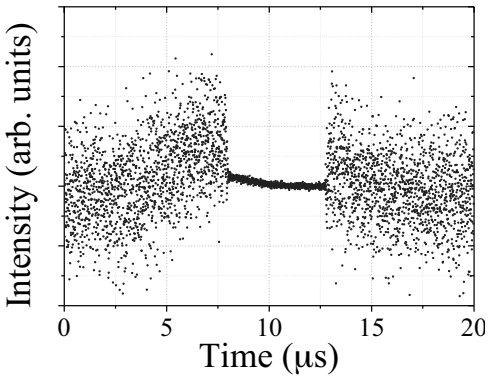

Fig. 4. Result of Storage and retrieval experiment for weak (2.6 nW) coherent light pulse.

3. Summary

We investigated the generation of orthogonally polarized photons pairs and the construction of light storage system using electromagnetically induced transparency. For the orthogonally polarized photons, the quantum characteristic was sufficient. However, its bandwidth has to be narrowed still more. For the light storage system, high-efficient storage was realized. However, the storage of extreme weak light is difficult for our current system. The ultracold high-density atomic sample earned from laser cooling technology would be required.

Construction of the Escherichia coli expression system of the cell membrane permeable iPSCs induced factors that strengthened proteolysis resistance

Yoshikazu MASUHIRO

Medicine

It is required that the induced pluripotent stem cells (iPSCs) to use for regenerative medicine are safe genetically. As for the current iPSCs derivative methods, the virus methods are mainstream, but gene variation is concerned about by these methods. Therefore, the derivative method using protein and the reagent is expected in future.

1. Making of the proteolysis-resistant and cell membrane permeable mouse Yamanaka factors

The derivative method with the cell membrane permeable proteins have been already reported by two groups, but induced efficiency is extremely bad, and there are many problems (operation and preparations are great). For this reason, it is thought that cell-permeable proteins are degraded in a cell early. Therefore, in this study, we work on development of iPSCs induced factor (Oct4, Sox2, Klf4, Glis1) having resistance in the proteolysis in the cell. We try in particular application (it fuses as a tag) of proteolysis-resistant motif Stabilon which we developed originally in our laboratory (Arakawa, T, Masuhiro, Y, et. al. 2010, BBRC). In a past study, because the Stabilon was quite effective about Sox2 and Glis1, we made Stabilon fusion and a non-fusion for these proteins. From the quantity of the expression and simplicity of purification, we decided that these proteins expressed in inclusion body of Escherichia coli.

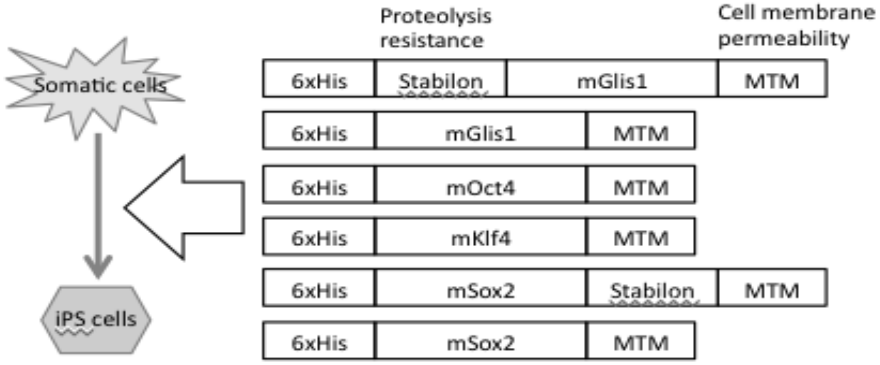

We performed cloning of these yamanaka factors in pET28a expression plasmid and transformed it in BL21(DE3). Oct4; 3mg, Sox2; 3mg, Sox2-Stabilon; 3 mg, Klf4; 4.5mg, Glis1; 1.2mg and Glis1-Stabilon; 1.2 mg expressed in BL21(DE3) per 1 liter LB culture media. In addition, we purified these proteins under guanidine hydrochloric acid and urea (denature condition) from an inclusion body, and performed refolding by the dialysis. These denature proteins refolded about Oct4; 30%, Sox2; 10%, Sox2-Stabilon; 30%, Klf4; 5%, Glis1; 0% and Glis1-Stabilon; 5%. In addition, we were able to confirm the DNA binding capacity by Gel shift assay about Sox2, Sox2-Stabilon.

2. Making of the proteolysis-resistant and cell membrane permeable Homo sapiens Yamanaka factors

To make genetically safe human induced pluripotent stem cells, we wrestled for expression system development of the proteolysis-resistant and cell membrane permeable Homo sapiens Yamanaka factors protein. We made a fusion body and a non-fusion body about Oct4, Sox2, Klf4, all of Glis1 and built a good expression stock in BL21(DE3). We introduce it into a normal human fibroblast cell and going to try iPS induction in future.

3. Making of the proteolysis-resistant and cell membrane permeable cell-differentiation factors

It is important that the establishment of efficient induction of the differentiation cell from induced pluripotent stem cells, too. In this study, we tried expression system construction of the protein which was inducible with a maturity white blood cell (granulocyte), Treg cell, hepatocytes. The maturity white blood cell differentiation system built expression system of cell membrane permeable RARα (retinoic acid receptor in the nucleus) as protein therapy of the acute promyelocytic leukemia. About the Treg cell, we built expression system of the cell membrane permeable Foxp3 (master gene of Treg cell) as the protein therapy which atopy and asthma improve. For hepatocellular regenerative medicine, we performed expression system construction of Sox17 and HNF3β which promoted hepatocellular differentiation. We made the Stabilon-fusion for all of these proteins. About RARα, we confirmed that the ability of DNA binding, cell-permeability, transcriptional activity and induction of granulocyte from NB4 (from a patient). About Foxp3, we confirmed the ability of cell membrane permeability, transcription activity.

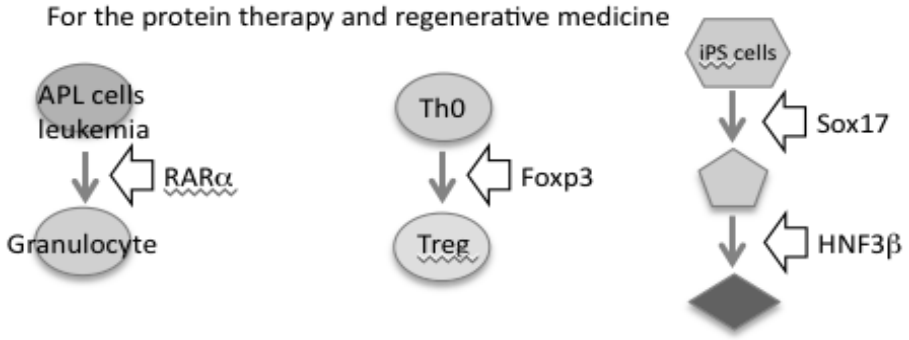

Pharmacokinetic/Pharmacodynamic Modeling of Tumor-localizing Photosensitizing Compounds and Pyrrole-Imidazole Polyamides

Takahiko AOYAMA, Yoshiaki MATSUMOTO
Medicine

In drug development, the study for the pharmacokinetics of drug candidates is necessary. Model-based drug development is characterized as the development and application of mathematical models of drug efficacy and safety from preclinical and clinical data to improve drug development knowledge management and decision making. In pre-clinical phase, mathematical modeling is an approach for making prediction of human pharmacokinetics. We investigate the pharmacokinetics of novel compound CT101019a which is a candidate for tumor-localizing photosensitizing compound, and of pyrrole-imidazole polyamides in the *N*. research project.

1. Pharmacokinetic modeling of tumor-localizing photosensitizing compounds

In photodynamic therapy, a systemically administered photosensitizing agent is activated by laser light of a specific wavelength delivered by an optical fiber. Light activated photosensitizer molecules react with endogenous oxygen which initiates a series of intracellular events that result in the destruction of target tissues. Talaporfin sodium is a photosensitizing agent (Fig. 1). CT101019a (supplied by Prof. Otsuki) is a novel compound for photosensitizing agent (Fig. 2).

To describe the relationships between light dose, percent cures and plasma talaporfin sodium concentration, we develop the pharmacokinetic/photodynamic model of talaporfin sodium. The plasma talaporfin sodium concentration, percent cures following photodynamic therapy and light dose reported by Ferrario *et al*. were used as the source of pharmacokinetic/photodynamic modeling data. The pharmacokinetics for talaporfin sodium in mice was described by two-compartment model with first-order elimination. The relationships between the percent cures, light dose and plasma talaporfin sodium concentration were described by Emax model (Fig. 3).

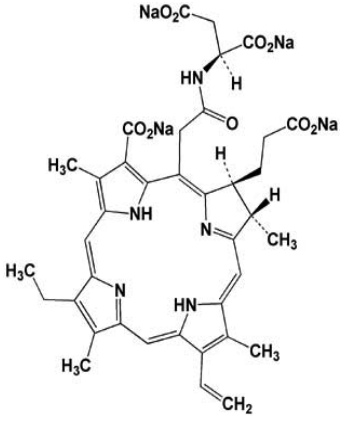

Fig. 1 Talaporfin sodium

A simple and sensitive HPLC method is developed for the determination of plasma CT101019a concentration in rats and applies to the pharmacokinetic study. The half-life of CT101019a was shorter than talaporfin sodium. To predict human pharmacokinetics of CT101019a, exploratory population pharmacokinetic model of talaporfin sodium was developed using the human, rat and mice pharmacokinetic data of talaporfin sodium. Simulated human plasma CT101019a concentration profile is shown in Fig. 4. These findings are useful for drug developments of tumor-localizing, photosensitizing agent.

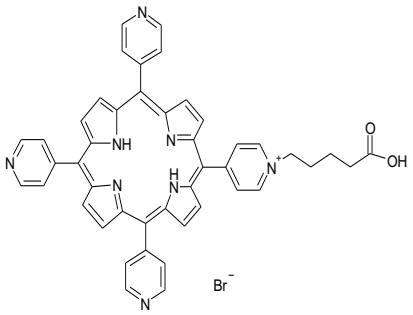

Fig. 2 CT101019a

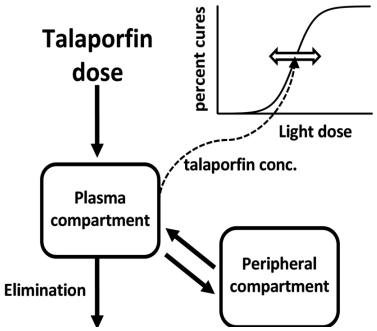

Fig. 3 Pharmacokinetic/photodynamic model of talaporfin sodium

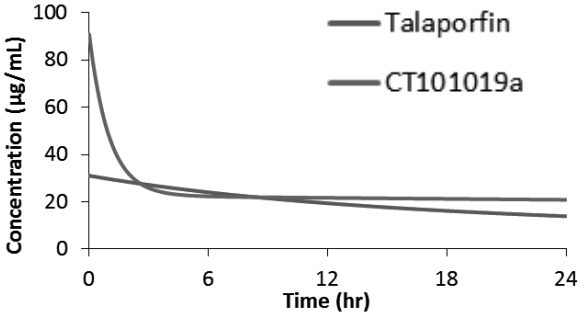

Fig. 4 Simulated human plasma concentrations

2. Pharmacokinetic modeling of pyrrole-imidazole polyamides

Pyrrole-imidazole (PI) polyamides (supplied by Prof. Fukuda) are synthetic molecules composed of aromatic rings of *N*-methylpyrrole and *N*-methylimidazole amino acids shown in Fig. 5. PI polyamides can easily enter into the nucleus and bind to chromosomal DNA, and have been identified as novel candidates for gene therapy. We develop a simple and sensitive method using an internal standard that was developed for different sequence and longer PI polyamide (*J Biomed Biotechnol*, 2012). Using the urinary and biliary excretion data, we develop a pharmacokinetic model (Fig. 6, 7) that describes the plasma PI polyamide (MW, 1035) concentration profiles under lower limit of quantification (*Biol. Pharm. Bull*, 2009; Non-Viral Gene Therapy, In-Tech Open Access Publisher, 2011). The possible metabolism of several PI polyamides (MW, 1422-1669) was investigated. The peaks of their metabolites and the decreases in the PI polyamides concentrations with incubation time were not detected under the experimental conditions. Because of the potential co-administration with other drugs, it was investigated whether PI polyamides inhibits various human cytochrome P450 *in vitro*. PI polyamides did not inhibit any of the tested human cytochrome P450. These findings indicate that the possibility of metabolic interaction between PI polyamides and other drugs commonly used in the treatment of patients is low.

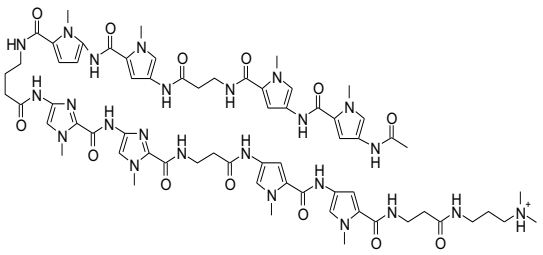

Fig. 5 Example for structure of PI polyamides

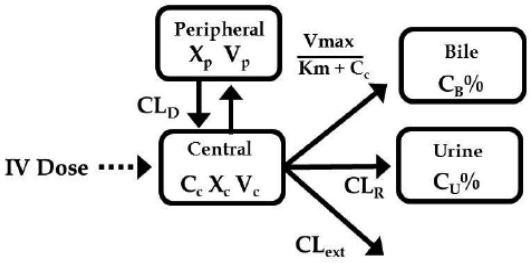

Fig. 6 Pharmacokinetic model of PI polyamides (Non-Viral Gene Therapy, 2011)

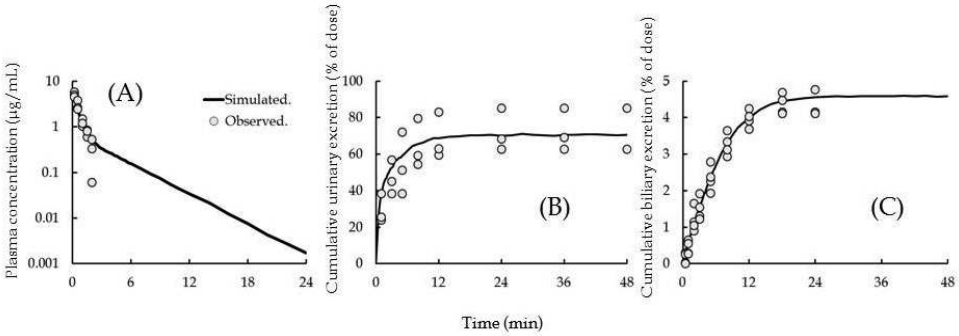

Fig. 7 Plasma PI polyamides concentration (A), cumulative urinary (B) and biliary (C) excreation profiles (Non-Viral Gene Therapy, 2011)

Self-assembly and Self-organization from the viewpoint of Device-fabrication Methods

Sachiko MATSUSHITA
Supramolecular and Self-Assembly; Energy Technology

Two subjects related with self-assembly and self-organization were studied with perspective of the developments of unexplored scientific fields and new technology: 1) Dye-sensitized photonic crystal electrodes, and 2) Fabrication of optical devices via self-assembly.

1. Dye-sensitized photonic crystal electrodes

There are few reports on photoelectric conversion efficiency using naturally-occurring dyes for dye-sensitized solar cells (DSSC). This is because the matching with an excited electronic level of naturally-occurring dye to the conduction band of semiconductor is problematic; the excited electrons are easily relaxed to the steady state with fluorescence or heat emission. We examined the fluorescence inhibition effect of a self-assembled photonic crystal using Chlorine e6 dye. Chlorine e6 is derived from chlorophyll and has a long excited electron lifetime. We prepared TiO_2 inverse opals with various particle sizes by liquid phase deposition (LPD) and described their effect on DSSCs with

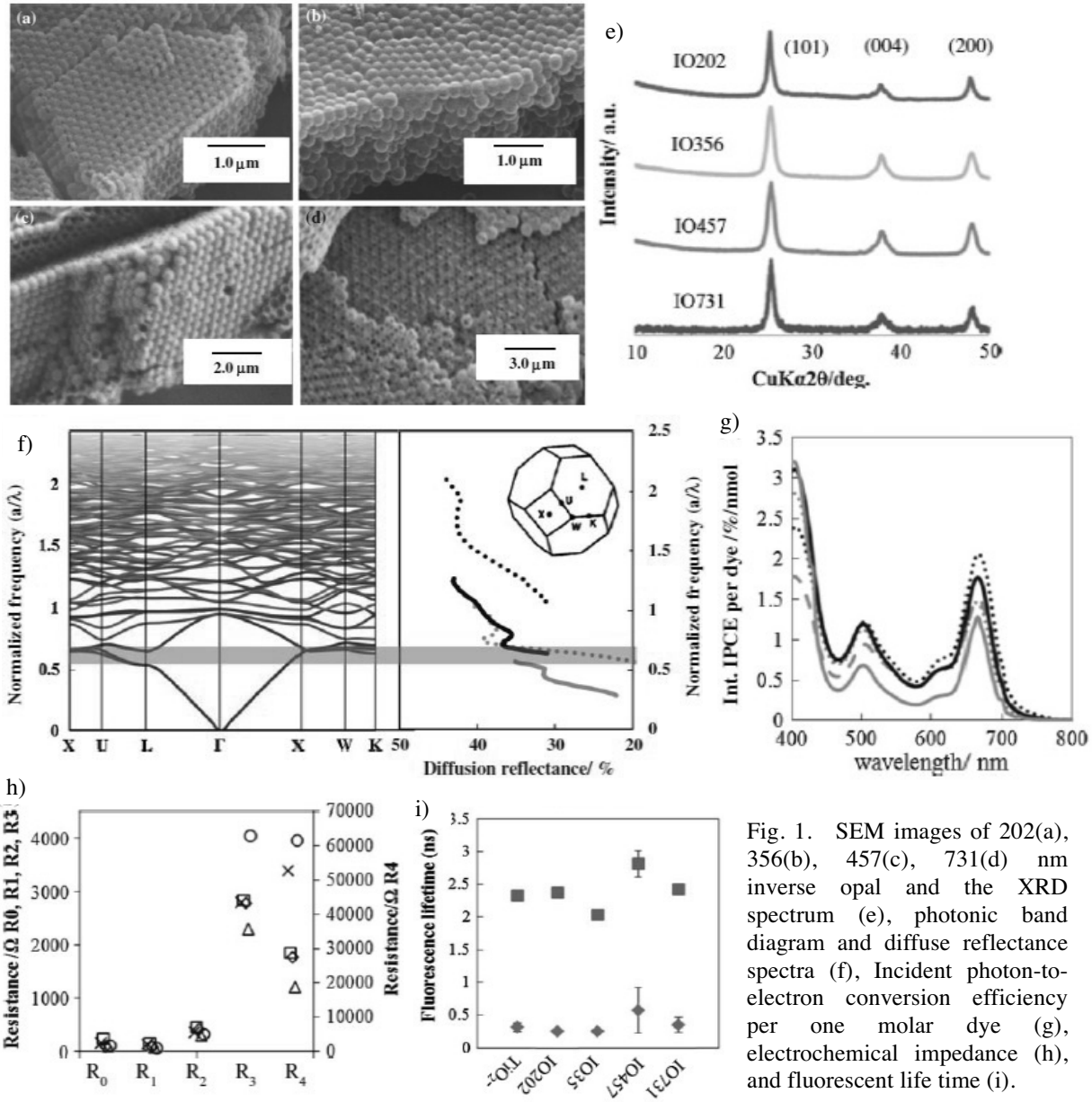

Fig. 1. SEM images of 202(a), 356(b), 457(c), 731(d) nm inverse opal and the XRD spectrum (e), photonic band diagram and diffuse reflectance spectra (f), Incident photon-to-electron conversion efficiency per one molar dye (g), electrochemical impedance (h), and fluorescent life time (i).

regard to structural, optical and electrochemical properties. In addition, we explored the implications of fluorescence lifetime measurements relative to the photonic band diagram and the amount of adsorbed dye. Although the main factor affecting the external photoelectric conversion efficiency was the diffusion resistance of the electrolyte and the contact resistance between TiO_2 interfaces, the possibility that the dye fluorescence lifetime, i.e. the photonic band structure, can affect the internal quantum efficiency per one dye molecule was also investigated (Fig. 1, *J. Porous Mater., in press.*).

For the better understanding of the relationship between the photonic band and electrochemical reaction, full-photonic bandgap photonic crystal composed of TiO_2-electrolyte structure is required. Thus, we also demonstrated the fabrication of a photonic crystal structure of (001) rutile TiO_2 substrate by deep reactive ion etching (RIE) using SF_6 plasma. A vertical etching profile and a smooth etched surface, which satisfy the requirements for optical device application, were obtained (*Jpn. J. Appl. Phys.,*51*,* 098002 (2012)).

2. Fabrication of optical devices via self-assembly

Complicated metal nanoshell/dielectric core structures, such as a nano-six-petaled structure, were fabricated by controlling the sintering and etching of colloidal crystal structures (Fig. 2a, *Chem.Comm., 48 (11), 1668-1670* (2012)). As the sintering processes, one-step sintering and two-step sintering were examined. The two-step sintering process successfully suppressed the movement of SiO_2 particles on a quartz substrate during the thermal sintering. As the subsequent HF etching treatment, the two-step sintered structures showed different morphology from the etched one-step sintered structures. The structural dependence of position and intensity of the plasmon resonance peak was observed. These optical phenomena were discussed from the viewpoint of domain size, particle shapes and nanogaps. The Raman scattering effect of these nanostructures was also examined （Fig. 2b, *Colloid. Surf. A,* 436, 930-936 (2013).）.

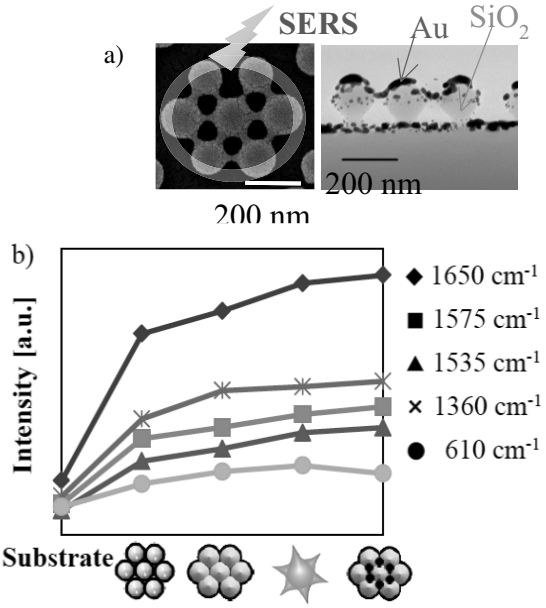

Fig. 2. TEM images of the nano structures (a) and Raman scattering analysis of Rhodamine 6G(b)。

Research for high density and high speed magnetic recording
- Thermally assisted magnetic recording applying near field optical light -

Katsuji NAKAGAWA
Information (Recording)

Information recording as well as information processing, and information communication are very important information infrastructure. Thermally assisted magnetic recoding (TAMR) has been studied in this project to achieve high-density magnetic recording. This research leads to a patent for achieve high-speed magnetic recoding as well as an award for the 2013 best paper of Magnetics Society Japan.

1. Thermally Assisted Magnetic Recording

Heat distribution and heat response by the effect of a surface plasmon antenna have been studied, because it is very important to locally heat by the plasmon antenna to achieve high-density magnetic recording. The structure of the antenna as well as the recoding media has been also studied by the Finite Difference Time Domain (FDTD) method.

It was found that the Bit Patterned Medium (BPM) was an effective medium for increasing temperature by the plasmon antenna as well as for isolated heat in the medium. The temperature distributions for BPM and continuous medium (CM) are shown in Fig. 1. The peak temperature increase in BPM was 140 degrees in Celsius after 1 ns light exposure, even though the temperature rise for CM was only 10 degrees in Celsius.

The temperature plane distribution for BPM calculated by FDTD method is shown in Fig. 2. It is observed that the particle of the BPM at the tip of the plasmon antenna shows the highest temperature.

The temperature responses for the square ordered BPM are shown in Fig. 3. The peak temperature rise for the particle #1 shows 140 degrees, and the its temperature decreases lower than 20 degrees in 1 ns. The second highest neighbor particle #3 shows 65 % temperature rise compared with the particle #1.

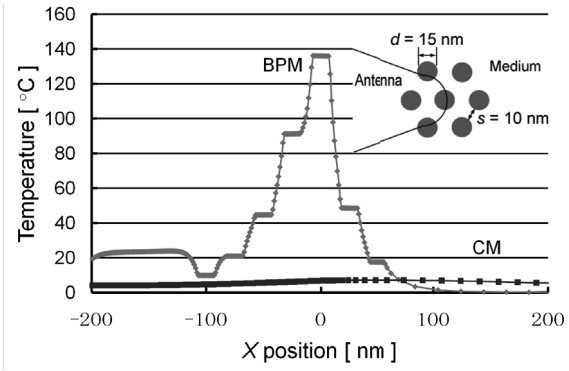

Fig. 1 Temperature distributions of continuous medium (CM) and bit patterned medium (BPM).

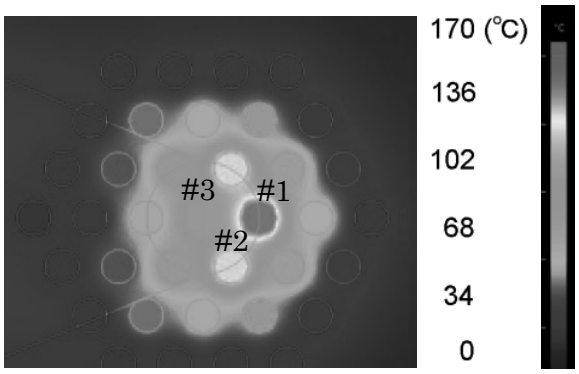

Fig. 2 Temperature distributed diagram parallel to X-Y plane of bit patterned medium (BPM).

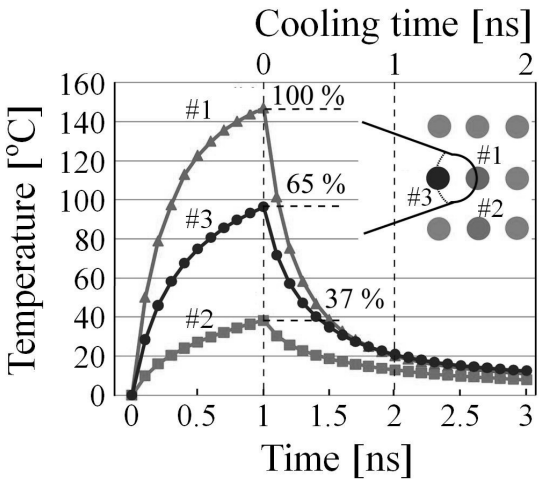

Fig. 3 Temperature of three columns (#1, #2, and #3) as a function of time. Media was BPM with rectangular arrangement.

2. Experimental results for TAMR

Plasmon antennas made by gold were placed over a magnetic layer, and exposed with femto-second laser by Assoc. Prof. Tsukamoto who is a project member. Written magnetic domains at the tip of the plasmon antennas and the rings around the number were observed by a magnetic force microscope, as shown in Fig. 4. The result has been reported to the Journal of Magnetics Society of Japan, Vol. 37, 119-122 (2013). The paper was awarded as one of the 2013 best paper of Magnetics Society of Japan.

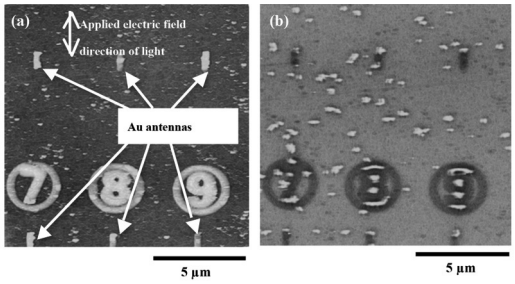

Fig. 4 Surface morphology (a) and written magnetic domains (b) observed by magnetic force microscope for rod plasmon antennas.

The minimum domain size in Fig. 4 was 166 nm× 120 nm. To achieve smaller written domain, the process of E-beam lithography was improved to get fine antenna patterns by the advice from Dr. Hashiba who is one of the project members. The smaller written magnetic domain: 120 nm ×84 nm was achieved by using smaller and square plasmon antenna, as shown in Fig. 5. The achieved written magnetic domain size is a little bit bigger than the size of goal, but 60% of the goal has been achieved. We still keep trying this experiment, because we are confident to achieve the goal by simulation.

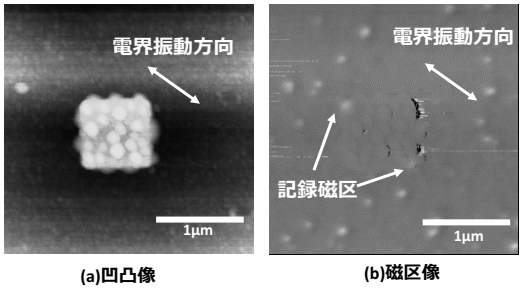

Fig. 5 Surface morphology (a) and written magnetic domains (b) observed by magnetic force microscope for square plasmon antennas.

3. Optical-induced ultra-high speed magnetization

The phenomenon of optical-induced ultra-high speed magnetization which has been found by the project members: Assoc. Prof. Tsukamoto, Prof. Itoh, and *et. al.*, has a potential to increase a recording speed by 100 thousands times. The research to increase magnetic recording density with applying this optical-induced ultra-high speed magnetization with circularly polarized light has been studied collaborated Prof. Ohnuki who is one of the project members. It was found that circularly polarized light in the metallic particle at the center of cross metal aperture enabled to be generated by FDTD method. The aperture shape of a four-leaf clover can also create circularly polarized light in a metal particle, as shown in Fig. 6. A patent about this result has been submitted.

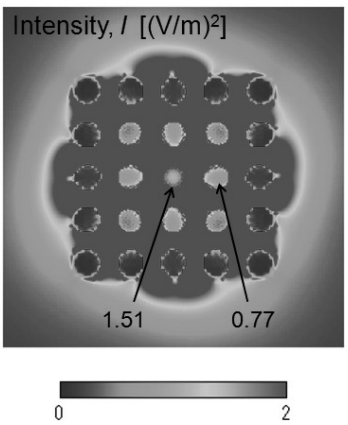

Fig. 6 One of simulation results calculating optical intensity distribution for patterned media.

An analysis method of a transient response phenomenon of surface plasmon generation by simulation was investigated in collaboration with Assoc. Prof. Ohnuki, and we developed into the electromagnetic transient analysis method which could apply nano-sized dispersion material and ensure accuracy of the calculation. It makes assumption of plasma frequency and transient analysis of arbitrary three-dimensional objects possible.

Development of Elemental Technologies toward Quantum Information and Communications

Naoto NAMEKATA
Information Technology

Quantum information and communication technologies (QICTs) are the most advanced ICTs that rely on quantum effects, and they offer the ways to realize (1) unconditionally secure communication and (2) low-power and high-capacity communication. Specifically, (1) can be realized by quantum key distribution (QKD), and (2) can be realized by a coherent optical communication technology that incorporates quantum information processing (computing). These QICTs give us "secure" and "green" solution for ICTs, which is very important especially in a highly developed information society. In this work, we have developed elemental technologies for QICTs.

1. Photon Detection Technologies

Photon detector is essential for QICTs. In order to realize QICTs using installed optical fiber networks, the photon detector must have a high photon detection efficiency in telecommunication band (~ 1550 nm: the minimum-loss window of optical fibers) with low noise counts. We have developed the telecom-band single-photon detector (SPD) using a compound semiconductor device, namely an InGaAs/InP avalanche photodiode (APD). Although the SPD based on the InGaAs/InP-APD is very practical, it has drawbacks, compared with the other SPDs, that are an afterpulse noise and a low repetition frequency. We proposed a "sinusoidal gating" method in which a sinusoidal voltage was used as the gate voltage. Then, using the sinusoidally gated InGaAs/InP-APD, high-speed single-photon detection at 1550 nm can be realized with a low afterpulse probability. Currently, we achieved a repetition frequency of 2 GHz which is three orders of magnitude higher than that of the conventional gated InGaAs/InP-APD. Moreover, the photon detection efficiency of > 10% was achieved with a dark count probability of 10^{-7} and an afterpulse probability of < 3% (*IEEE Photo. Tech. Lett.* 2010; *Opt. Express* 2011). We also applied the sinusoidal gating method to a Si-APD. Using the sinusoidally gated Si-APD (quantum efficiency was 72.4%), visible-light single photons can be successfully detected with a detection efficiency of 70.6%, which implies that a photo-excited single charge carrier in a silicon avalanche photodiode can trigger a detectable avalanche (charge) signal with a probability of 97.6% (*Appl. Phys. Lett.* in press).

Although advanced QICTs demands the photon number resolving capability, the SPDs described above do not have it. Therefore, we have developed the so-called photon-number-resolving detector (PNRD) using a superconducting Titanium transition edge sensor (Ti-TES). We achieved a detection efficiency of > 80 % at 1550 nm with a photon number resolving capability of < 0.2 eV. Then, we applied the developed PNRD to a non-Gaussian operation on the pulsed squeezed vacuum at 1550 nm. The two-photon-subtracted squeezed state was successfully generated (*Nature Photonics*, 2010). We observed dips in reconstructed Wigner functions of the generated quantum states (see Fig. 1), which is the clear evidence that the non-Gaussian operation was realized.

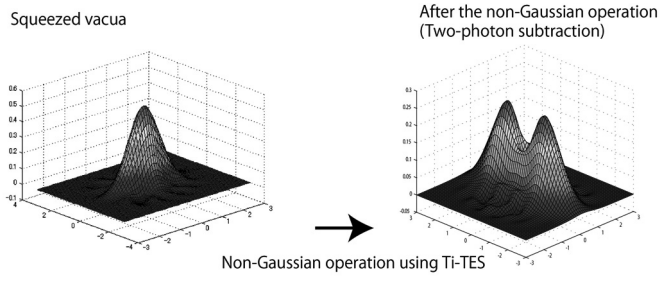

Fig. 1. Wigner function of the generated non-Gaussian state

2. Quantum Key Distribution Experiments

We performed a 2 GHz clocked differential-phase-shift QKD (DPS-QKD) experiment using SPDs based on sinusoidally gated InGaAs/InP-APD. A secure key rate of 24 kbit/s was achieved over 100 km of optical fiber, which was higher than the previous record. Moreover, we have successfully distributed secure keys against the general individual attacks over 160 km of optical fiber (*Opt. Express*, 2011. Fig.2). These results will accelerate the realization of a practical QKD over a metro-sized optical fiber network.

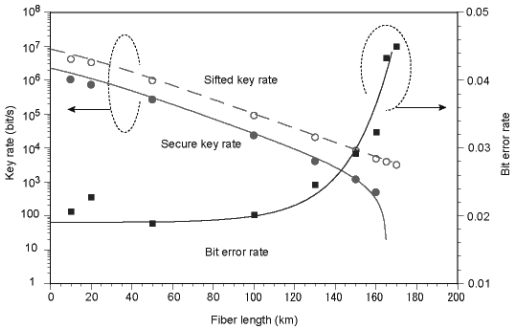

Fig. 2. Secure key rate as a function of the communication distance

To extend the communication distance further, e.g. > 400 km, entanglement-based QKD system is preferable, because it will play an important role in the quantum repeaters described in the next section. We have developed the polarization entangled photon pair source and the entanglement-based QKD system using it (Fig. 3).

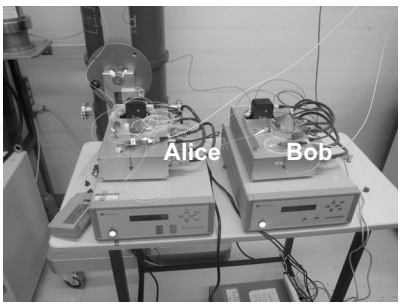

Fig. 3. Entanglement-based QKD system

3. Elemental Technologies for Quantum Repeater

To realize the long-distance QKDs, we need the quantum repeater which can improve the throughput reduction with distance from exponential to polynomial. The quantum repeater is composed of three elemental technologies: the entanglement swapping, quantum memories (or buffer storages), and the quantum non-demolition measurement of the photon number.

We demonstrated entanglement swapping with 1550 nm polarization-entangled photon pairs created by spontaneous parametric down conversion (SPDC) in two spatially separated type-II periodically poled lithium niobate (PPLN) bulk crystals. In a partial Bell-state measurement, entanglement was observed between two photons from independent sources. We employed sinusoidally gated InGaAs/InP-APDs operated at a repetition frequency of 1.28 GHz, which increased a four-fold coincidence count rate without degrading the fidelity of entanglement swapping. The obtained fidelity is ~ 90% which is high enough to infer a violation of Bell inequality and to implement the entanglement-based quantum key distribution (*J. Phys. B*, 2013).

In our experiment, the success probability of the entanglement swapping is less than 10^{-6}. To enhance the success probability, the key technology is the quantum memory (or buffer storages). In this work, we have tried to realize the photon buffer storage by means of an optical switching network. As shown in Fig.4, the photon buffer storage we designed is composed of optical fibers and low-loss fiber-optic components. It gives the programmable optical delay to photons with a low optical loss, and a quantum state of light (polarization of photons) can be maintained without any active compensation.

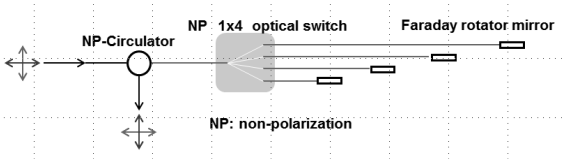

Fig. 4. Photon buffer storage using the optical switching network.

Summary

We have developed the advanced photon detection technologies. The state-of-the-art photon detectors have overcome the difficulties in development of QICTs.

Development of Nano-Composite Technologies for Innovative Hydrogen Storage

Nobuyuki NISHIMIYA
Energy Technology

Hydrogen storage alloys have occluding function to uptake hydrogen atoms into lattice spaces. Innovative hydrogen storage is thus expected by designing the lattice spaces or by stimulating active surface sites by means of ultraviolet irradiation and so on. Interruption of hydrogen storage by ambient oxidative attacks is took away by encapsulating the alloys with hydrogen permeable membranes and innovative hydrogen recovery from gas mixtures produced by water photo-splitting and biological fermentation and so on becomes plausible. The present study aims to apply several innovative hydrogen storage techniques to energy technologies through nano-composite formation on the basis of collaboration with peoples in the N. research project.

1. Application of Encapsulated Alloys Resistant to Ambient Air and Water

Environment resistant hydrogen storage alloys were prepared by encapsulating the alloys with silica-based hydrogen permeable membranes blended with silicone precursor. When the estimated thickness of the wall was 20 nm, the elastic capsule endured the expansion by 20% on hydrogen occlusion. Cycling experiments comprising hydrogenation of encapsulated ZrVFe alloys under the ambient pressure of detonating gas at room temperature and dehydrogenation thereof at elevated temperatures in vacuo showed reproducible behaviors for three times, which was contradictory to original alloys having no hydrogen occlusion ability after the second cycle. That clearly showed the difference of oxygen resistance.

Partial pressure of hydrogen was lowered in the presence of the encapsulated alloys during hydrogen production by cyanobacteria compared to the case in the absence of the alloys (Figure 1, *19th WHEC,* 2013). More hydrogen than that corresponding to the downward shifts from the dotted line in Figure 1 was occluded by the encapsulated alloys, and total amounts of hydrogen both in the gas phase and in the solid phase, the latter being determined by a vacuum extraction method on heating, exceeded 7 times as much as those in the absence of the alloys. The increased yield of hydrogen would be due to an equilibrium shift by removing hydrogen from the formation side.

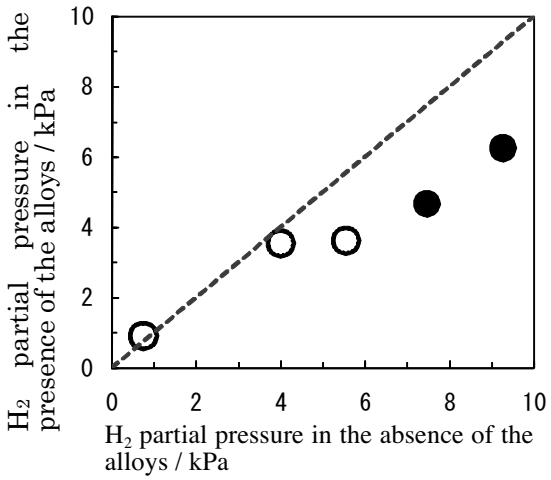

Figure 1 Effect of alloys on H2 partial pressure during bio-hydrogen production
●: Anabaena-ZrVFe system
○: Spirulina-$(Ti_{0.5}Zr_{0.5})(Fe_{0.2}Mn_{0.8})_{1.5}$ system

2. Photo-Stimulated Hydrogen Occlusion and Photo-Stimulated Hydrogen Desorption

Hydrogen capacity of a hexagonal alloy, $(Ti_{0.2}Zr_{0.8})(Fe_{0.5}Mn_{0.5})_{1.5}$, under 1 MPa of hydrogen at room temperature increased by 20% on ultra-violet irradiation at 352 nm in air. Presence of a photocatalyst, WO_3, enhanced the hydrogen capacity by 60%, and the enhancing effect was higher in a nitrogen atmosphere. It is plausible that some nitrogen containing functional groups were generated on irradiation and that they promoted hydrogen occlusion.

Ultra-violet irradiation lowered hydrogen desorption temperatures in vacuo for $LiBH_4$ and MgH_2, and the lowering was enhanced by the coexistence of WO_3. Desorption from $(Ti_{0.2}Zr_{0.8})(Fe_{0.5}Mn_{0.5})_{1.5}$ itself was not enhanced by irradiation, but specified combinations of photocatalysts lowered the

desorption temperature on irradiation.

While the lowering of hydrogen desorption temperatures was realized by addition of conventional catalysts, for example, the ones from MgH_2 at 130℃ and 400℃ were lowered to 60℃ and 200℃ by addition of Nb_2O_5, ultra-violet irradiation with WO_3 further added inhibited the desorption at the lower temperature. That meant the irradiation cancelled the catalytic effect, in other words, a route to an ON/OFF control of catalytic effects by irradiation was proposed.

3. Hydrogen Spillover at the Liquid Nitrogen Temperature

Hydrogen occupies 0.1575 nm^2 per molecule when adsorbed on high specific surface area materials at cryogenic temperatures. Such ordered adsorption gives a composition of C_6H_2 on graphene, or hydrogen capacity of 2.7% If hydrogen could adsorb in atomic states, a surface composition of C_6H_6 would be attained to present promising hydrogen storage materials. Since spillover would be easy with hydrogen atoms available, such metals that dissociate hydrogen at low temperatures like 77 K (liquid nitrogen temperature) are needed.

Through synthesis of single-walled carbon nanotubes by a torch arc method, synthesis of metal-modified nanocarbons by a conventional arc method, graphene formation by the Hammers method and metal-modification, synthesis of carbon-modified metals by a methanol CVD (Chemical Vapor Deposition) and synthesis of metal-modified nanocarbons by calcination of electrospun polymer fibers, Pt proved to have the highest dissociation activity of hydrogen among Ni, Pd and Pt. Such were also the case for BN, CN and BCN which were prepared by respective wet procedures (*J. Alloys and Compounds*, 2013). Search for alternative metals or alloys that could replace expensive and rare Pt revealed potential feasibility of Cr-Fe and Invar (Fe-Ni-Mn) alloys. In the course of surveying, a unique alloy as described in the next section appeared, which showed irregular hydrogen occlusion isotherms.

4. Superposition of Hydrogen Storage in Lattices and Adsorption at Liquid Nitrogen Temperature

Occlusion of hydrogen proceeds with atomic hydrogen trapped inside the lattice, and the occluded amount of hydrogen is thus normally proportional to power of 1/2 of hydrogen pressure (Sieverts' law). But the amount of hydrogen occluded at RT (26℃) in $(Ti_{0.2}Zr_{0.8})(Fe_{0.5}Mn_{0.5})_{1.5}$ was ruled out by power of 1/4 of pressure, and the one at cryogenic temperatures was proportional to power of 1 of pressure as shown in Figure 2.

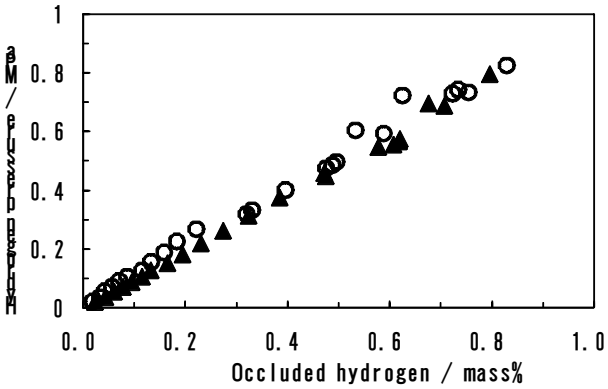

Figure 2 Hydrogen occlusion isotherms at 77 K for $(Ti_{0.2}Zr_{0.8})(Fe_{0.5}Mn_{0.5})_{1.5}$
○: simple adsorption at 77 K
▲: successive adsorption at 77 K after RT occlusion

The dependence on power of 1 meant Henry's law and hydrogen proved to dissolve as molecules. The power of 1/4 phenomenon would be actual if one molecule of hydrogen could form 2 atoms and additionally the same amount of vacancies.

Hydrogen adsorption at 77 K after RT sorption of 0.634 mass% under 1 MPa of hydrogen (▲ in Figure 2) unexpectedly proceeded similarly as adsorption without the RT sorption. Furthermore, measured equilibrium pressures at 77 K were unreasonably higher than those at RT. It is thus likely that the hydrogen storage inside the crystal lattices (occlusion at RT) and the solution-like adsorption at 77 K carried out at different sites. Otherwise solution at 77 K could occur either at lattice spaces or at vacancies connecting to the lattice spaces. Novel materials capable of both lattice type occlusion and solution type adsorption will be promising for innovative hydrogen storage.

Nano-Electromagnetic Simulation for Light-Material Interactions

Shinichiro OHNUKI
Quantum Theory and Computation

We have developed fast and reliable electromagnetic simulation methods for studying interaction between light and nanoscale objects. We apply our novel methods to designing nanoscale devices for high-speed and high-density magnetic recording, quantum telecommunication, and so on. This research was awarded the 2013 academic award from College of Science & Technology, Nihon University and the 2013 best paper of Magnetics Society Japan.

1. Time Domain Responses of Electromagnetic Fields by Integral Equation Methods

We have developed novel fast and accurate solvers based on integral equation methods with fast inverse Laplace transform for time domain electromagnetic problems (*J. Electromag. Waves and Applic.*, 2012). The advantages of our proposed method are (1) the computational error is easy to be controlled, (2) there is the no restriction of selecting time step size, and (3) an arbitrary observation time can be selected. Using the combination of fast algorithms and parallel computing, the speedup rate becomes over 100 times faster. We have designed plasmonic antennas which can localize circularly polarized light in nanoscale (Figs. 1 and 2).

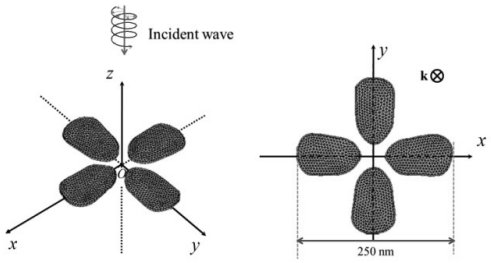

Fig. 1 Design of Plasmonic Antennas for All-Optical Recording.

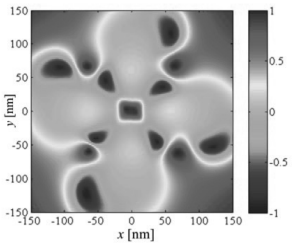

Fig. 2 Verification of Localized Circularly Polarized Light.

2. Design of Plasmonic Antennas with Bit-Patterned Media for High-Density Magnetic Recording

We study characteristics of plasmonic antennas with bit-patterned media to realize high-density all-optical magnetic recording through the collaboration with Prof. Katsuji Nakagawa, Information Group (*IEEJ Trans. A*, 2014). Figure 3 shows an asymmetric cross antenna constituted by two dipole antennas with bit-patterned media. Antenna lengths are selected to obtain 90° phase shift. Localized circularly polarized light is generated inside the particulate medium at the center of antennas. In our proposed system, the recording density can be achieved over 2Tbit/inch^2.

We investigate the motion and required DC field of magnetization reversal using micro magnetics simulation in collaboration with Prof. Arata Tsukamoto, Information Group, as in Fig.5.

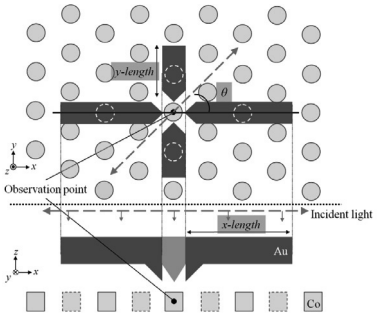

Fig. 3 Proposed system for high-density all-optical magnetic recording.

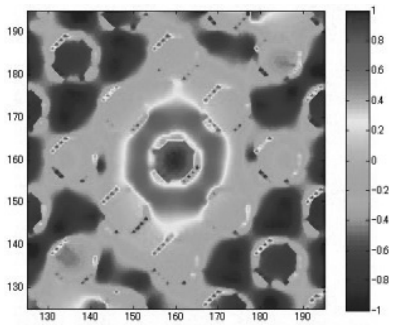

Fig. 4 Circularity inside the bit-patterned media.

3. Multiphysics Simulation of Nanoscale Objects in Laser Fields

We have developed the coupled Maxwell-Schrödinger scheme which is based upon the FDTD method in collaboration with Prof. Tokuei Sako, Quantum Theory and Computation Group (*Int. J. Numer. Model.*, 2013). Our proposed method can handle tunneling effects due to well structures. We have investigated current densities and electromagnetic fields of nano plates. Advantages of our method have clarified in comparison with conventional classical solvers.

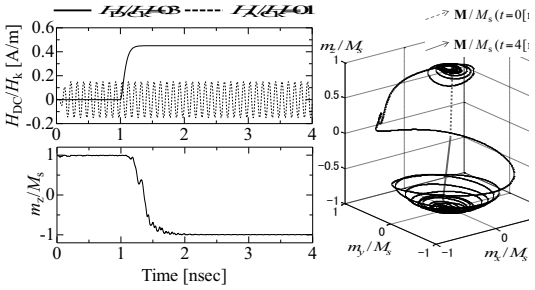

Fig. 5 Magnetization reversal by micro magnetics simulation.

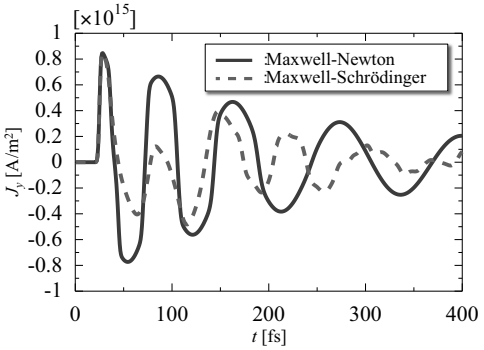

Fig. 6 Time domain response of current density in a nano plate.

We have investigated the interaction between the light control pulse and thin tube including only a single electron as shown in Fig. 7, where the pulse is designed to control the electron-state. The time domain response of probability density is presented in Fig. 8. Our designed pulse has excellent ability to control the electron state with high accuracy.

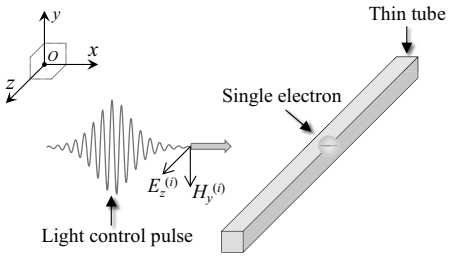

Fig. 7 Nano tube and the coordinates.

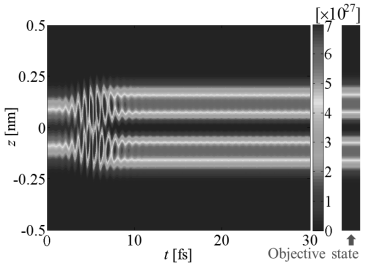

Fig. 8 Control of electrons states by a light pulse.

4. Modeling of Plasmonic Waveguides for a High Sensitivity Optical Sensor

We have proposed an optical sensor which consists of a metal stripe and nano wire. Using the proposed device, electromagnetic energy is concentrated around the metal stripe and the energy can be efficiently absorbed into the nano wire. Joule heat inside the nano wire is produced due to the electromagnetic energy and becomes over 50 times higher than that for the case without the metal stripe.

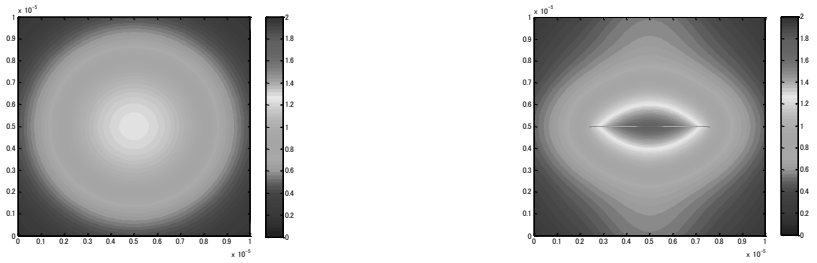

(a) without the metal stripe (b) with the metal stripe

Fig. 9 Electromagnetic field around the nano wire.

Self-Assembled Supramolecules and Their Applications to Energy, Medical, and Information Technologies

Joe OTSUKI
Supramolecular and Self-Assembly; Energy Technology

Self-assembly of appropriately designed molecules offers a promising bottom-up method for producing nanostructures. This work aims at developing new molecular self-assembling systems, revealing self-assembled structures and dynamic behaviors at the molecular level, and searching for applications of self-assembly to energy, medical, and information technologies. We believe that assembly of a chlorophyll derivative into double-helical structures and visualization of rotational motion of a double-decker porphyrin complex at the molecular scale are two prominent achievements.

1. Structures, control, and dynamic behaviors of molecular self-assemblies

We revealed the effects of side arms introduced in the porphyrin framework on the self-assembly at the molecular scale using scanning tunneling microscopy (STM).[1] We found that interactions between porphyrins and the graphite surface predominates when the porphyrin was modified with long side arms, resulting in arrays of face-on porphyrins on the substrate. On the other hand, when the porphyrin was modified with short side arms, intermolecular interactions outweighed, giving rise to porphyrin columns with stacked porphyrin molecules (Fig. 1a). We also investigated the self-assembly of artificial chlorophyll, which has a zinc ion in the center and a pyridyl moiety on the periphery.[2] This molecule forms a quite stable cyclic tetramer in solution. In the crystal, the pyridyl group in one molecule coordinates to the zinc ion in the next molecule, giving rise to coordination polymers. A pair of helical polymers wrap around each other, affording double helices as shown in Fig. 1b. These highly-ordered, extended structures of porphyrins and chlorophylls are interesting as potential wires for energy and electrons.

We constructed a system in which interaction between a zinc-porphyrin and a pyridyl group can be switched on/off with the trigger of light (Fig. 1c).[3,4] The molecules incorporate a photoisomerizable azopyridine group in a molecular bowl. In the trans configuration, the pyridyl group sticks out of the bowl, while in the cis configuration, the pyridyl group directs inward. We found that the binding constant for the trans isomer was up to 20 times larger than that for the cis isomer.

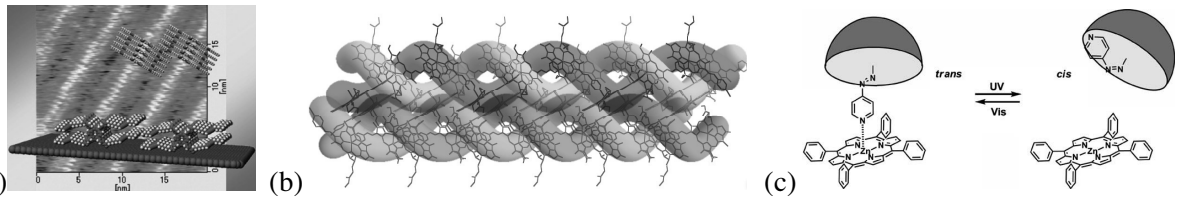

Fig. 1. Structures and control of porphyrin assemblies. (a) One-dimensional porphyrin columns. (b) Double helices of a chlorophyll derivative. (c) Control of assembly with light.

We revealed the self-assembled structures and dynamics of double-decker porphyrin complexes at the molecular scale using STM. A certain double-decker porphyrin complex with a cerium ion was observed as circles, while the same complex but with a zirconium ion was observed as ellipses (Fig 2a).[5] We ascribe the difference in appearance to a difference in the speed of rotation of these molecules. We synthesized a double-decker porphyrin having a single side arm as a beacon for molecular orientation. We noted that some molecules changed their orientation on standing on the substrate, which turned out to be the first visualization of molecular rotation of this class of compounds (Fig. 2b).[6]

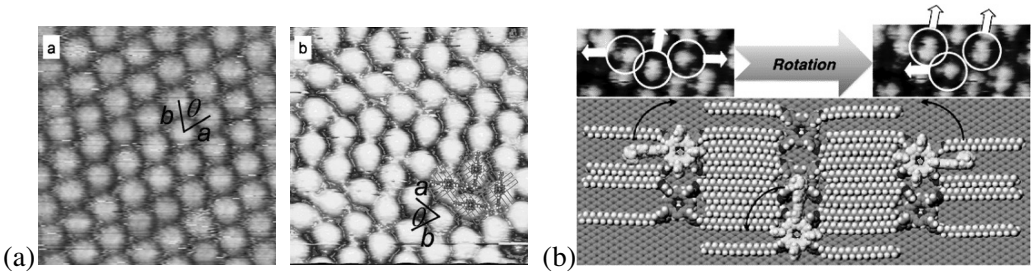

(a) (b)

Fig. 2. Double-decker porphyrins. (a) Different images due to rotation. (b) Change in orientation.

2. Photoenergy conversion by molecular systems

As for the reductive side of water photolysis, it is important that electrons are transferred efficiently from the photosensitizer to the reduction catalyst. We prepared photocatalysts in which the photosenitizers spontaneously assemble around a cobalt ion to form supramolecular photocatalyst (Fig. 3a).[7] We found that the amount of hydrogen produced by illumination using this system was twice that by a system without self-assembly.

The dye-sensitized solar cells (DSSCs) are attracting attention as a next-generation solar cell. The effects of a donor group on the perylenedicarboxylic anhydride derivatives were investigated as organic dyes.[8] We found that a donor group is effective to raise the energy level of the lowest unoccupied molecular orbital (LUMO), leading to efficient charge injection. We examined the effects of side arms but eventually found that dyes without side arms recorded the highest efficiency (3.1%). The reason for this is that the dye without a side arm was able to utilize up to the longest wavelength, which may be due to intermolecular interactions. This result indicates that some dyes work better with intermolecular interactions in spite of the conventional belief that dye aggregation is detrimental to the performance. We also prepared three new cyclometalated complexes and revealed their structures and properties.[10] New cyclometalated complexes for DSSCs based on these results are now in preparation.

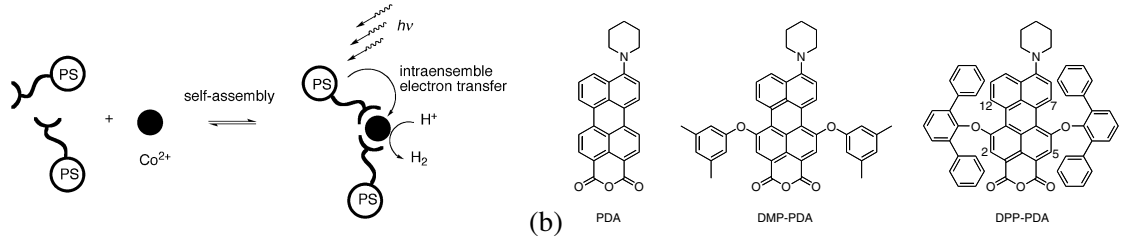

(a) (b)

Fig. 3. (a) Self-assembled photocatalyst. (b) Dyes for DSSCs.

3. Nanomaterials and their applications

Other than the systems described above, we investigated nanomaterials such as graphene[11,12] and nanoparticles.[13] Yet other works include studies on chlorophyll derivatives for photodynamic therapy in collaboration with Fujiwara et al in the Medical School, single molecule behaviors using fluorescence microscopy in collaboration with Chaen et al in the College of Humanities and Sciences, and nanoparticle assemblies for quantum information devices, in collaboration with Namekata et al in the Institute of Quantum Science.

(1) *Chem. Lett.* **2009**, *38*, 570. (2) *J. Am. Chem. Soc.* **2013**, *135*, 5262. (3) *J. Phys. Chem. A* **2010**, *114*, 884. (4) *Tetrahedron Lett.* **2009**, *50*, 2106–2108. (5) *Chem. Lett.* **2011**, *40*, 717. (6) *J. Am. Chem. Soc.* **2010**, *132*, 6870. (7) *Chem. Commun.* **2010**, *46*, 8466. (8) *Adv. OptoElectron.* **2011**, *2011*, Article ID 860486. (9) *Chem. Lett.* **2013**, *42*, 450. (10) *J. Organomet. Chem.* **2014**, *749*, 312. (11) *Appl. Nanosci.* **2013**, *3*, 477. (12) *Appl. Surf. Sci.* **2012**, *259*, 460. (13) *ACS Nano* **2013**, *7*, 9997.

Origin of Hund's rule and angular correlation in natural and artificial atoms

Tokuei SAKO
Quantum Theory and Computation Group

Artificial atoms or quantum dots, novel quantum systems confining a small number of electrons in a low-dimensional artificially-designed nanoscale potential well, play an essential role in the development of next generation devices operating under the principle of quantum mechanics, utilized in, such as, quantum computation and quantum telecommunication. Since the electronic properties of artificial atoms are known to depend strongly on their size and/or number of electrons, understanding their complicated electronic structure is one of the most fundamental and essential issues. In this direction the author has focused on in this *N*. project the origin of so-called Hund's rule and studied the mechanism of this fundamental rule operating in artificial atoms. An inherent hole in the spin-parallel singlet wave function has been identified and is called *conjugate Fermi hole*. It has been shown that the origin of Hund's rule is rationalized on the basis of this conjugate-Fermi-hole concept.

1. Origin of Hund's multiplicity rule

Empirically derived Hund's rules of pre-quantum-mechanics era that predict the ordering of the energy levels possessing different spin and orbital angular momentum quantum numbers proved to be almost universally valid for atoms, molecules, and quantum dots. Yet, despite the history of a long standing debate the search for various aspects of their origin persists, that was most likely due to our lack of knowledge as to how electrons in the system behave differently for different spin states. We explore the origin of the first Hund rule for a two-dimensional model of He-like systems and that of two-electron quantum dots which represent ideal systems providing a direct fundamental insight into the structure of the internal part of the fully-correlated wave functions, allowing us an unambiguous argument. An examination of their probability density distributions indeed reveals the existence of a region in the internal space which we refer to as a conjugate Fermi hole (Fig.1 Phys. Rev. A 2011). In this region the singlet wave function has a smaller probability density than the corresponding triplet one, in contrast to a genuine Fermi hole in which case the triplet has a smaller density than the singlet. Thanks to the presence of this conjugate Fermi hole, the singlet probability density has to migrate far away from the center of the one-electron potential, rationalizing thus a well-known broader electron density distribution of the singlet state than is the case for the corresponding triplet, that is a key observation to explain the singlet-triplet energy gap. This result was published in Journal of Physics B in 2012 and was chosen as IOP Select Paper, which was further covered by Europhysics News published by the European Physical Society. He was invited by JPS to write a review article on this subject in BUTSURI, that was published recently in the June issue of 2013 with the title "Origin of the First Hund Rule in He-Like Atoms".

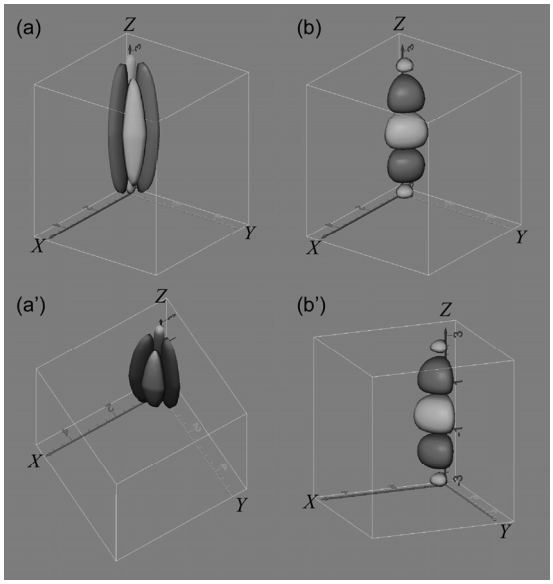

FIG1. Structure of standard Fermi holes (blue) and *conjugate Fermi holes* (red) in the internal space of two electron. (a) and (b) correspond, respectively, to the cases with (1s)(2s) and (1s)(2p) configurations. (a') and (b') represent the same distributions of (a) and (b), respectively, in a different viewpoint. The *X*, *Y*, and *Z* axes represent, respectively, the radial coordinate s_1, s_2, and the two-electron angle ϕ coordinates.

2. Conjugate Fermi holes and angular correlation

The helium atom has been an active source of both theoretical and experimental studies to explore electron correlation as the most simple and fundamental system. The angular correlation in singly-excited states of He and He-like atomic ions has been particularly focused on and studied extensively in the early 70th ~ the middle of 80th in the context of understanding the origin of Hund's rule. Among those pioneering studies Thakkar et al. showed that the probability density distributions of the singlet-triplet pair of state for the (1s)(2s) configuration depends only very weakly on the inter-electron angle irrespective of the nuclear charge Z_n whereas those for the (1s)(2p) configuration become appreciable for increasing nuclear charge Z_n.

It is noted that the effective correlation energy for atomic systems, defined by the correlation energy divided by Z_n^2 converges to 0 as $Z_n \rightarrow \infty$. Therefore, the wave function of the singly-excited states of He-like systems should become closer to that of an independent particle model based on the Hartree-Fock method as Z increases. On the other hand, the probability density distribution of the (1s)(2p) singlet-triplet pair of states shows an increasingly stronger dependence on the inter-electron angle, although in the limit of $Z_n \rightarrow \infty$ the electron correlation in the sense of a departure from the independent particle model diminishes to zero. In the present study in order to rationalize the origin of this strong inter-electron angle dependence in the probability density distribution of the (1s)(2p) pair of states we have examined in detail the nodal structure of the wave functions in the internal space.

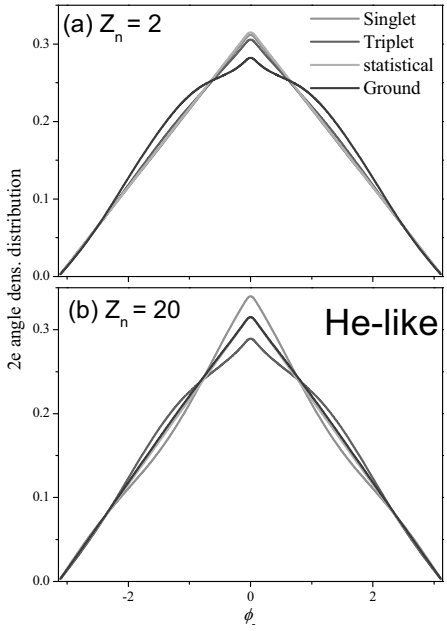

FIG2. Two-electron angular-density distributions for the He-like systems for different nuclear charge Z_n: (a) Z_n = 2, (b) Z_n = 20. The blue, green and red curves represent, respectively, the distribution of the $(1s)^2\ ^1S$ ground state, the singlet (1s)(2p) ^1P state and the triplet (1s)(2p) ^3P state. The statistical distribution, defined by $(\pi-|\phi_-|)/\pi^2$, corresponding to mutually independent rotation of the two electrons around the nucleus, is plotted as light-grey line.

We have used in this study the so-called two-dimensional helium model in which the spatial degrees of freedom of the two electrons are limited to a plane involving the nucleus. It was shown in earlier studies that this 2D model gives energy levels that have all characteristic features of those of the 3D case. The square of the probability density obtained from the full configuration interaction wave function $\Psi_Z(r_1,\phi_1,r_2,\phi_2)$ is integrated by the angle variable $\phi_+ \equiv \frac{1}{2}(\phi_1+\phi_2)$ corresponding to the total orbital angular momentum L. This yields the probability density $D_Z(r_1,r_2,\phi_-)$ in the internal space (r_1,r_2,ϕ_-), $[\phi_- \equiv \frac{1}{2}(\phi_1-\phi_2)]$.

The two-electron angular density distributions of the (1s)(2p) pair of states obtained by integrating $D_Z(r_1,r_2,\phi_-)$ with the radial coordinates (r_1,r_2) shows that the distribution of the singlet state has a peak at $\phi_- = 0,\pm\pi$ corresponding to the configuration where the two electrons align parallel to each other in the same side of the nucleus and that the distribution of the triplet state in turn has a peak at $\phi_- = \pm\pi/2$ corresponding to the configuration where they come in the opposite sides of the nucleus. This anisotropy of the angle density distributions shows to get pronounced for larger Z_n. The origin of the appearance of this anisotropy in the angle density distributions has been rationalized on the basis of the structure of the genuine and conjugate Fermi holes in the internal space (to be submitted to Phys. Rev. A).

Development of Pyrrole-Imidazole polyamide showing anti-tumor effect

Masayoshi Soma, Kyoko Fujiwara
Medicine

Pyrrole–imidazole (PI) polyamides can bind to double strand DNA in a sequence specific manner and suppress the expression of target gene by inhibiting DNA binding proteins including transcription factors. PI polyamides are small synthetic molecules composed of the aromatic amino acids N-methylpyrrole (Py) and N-methylimidazole (Im). A pair of PI polyamide recognizes specific DNA base pairs, i.e. Im/Py pair bind to G-C, Py/Im to C-G, and Py/Py to both A-T and T-A.

A concatenation of those pairs made it possible to bind to a variety of specific DNA sequences. Since PI polyamides can be effectively delivered to nuclei of several tissues without any specific drug -delivery system, they might be powerful materials to develop gene specific silencer. We have been developed various type of PI polyamides targeting genes involved in disease, and reported some of them had curative effect in vitro and in vivo.

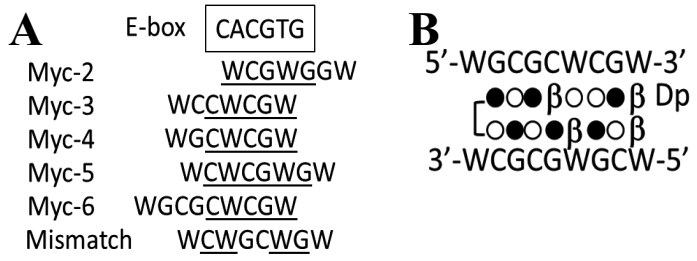

Fig.1 PI polyamides for E-box sequence
A. Recognition sequence of PI polyamides **B.** Structure of Myc-6 ○=Py; ●=Im, W= A or T

The amplification or over expression of c-MYC has been observed in many type of human tumors. c-MYC is a basics-helix-loop-helix leucine zipper transcription factor that binds E-box (5'-CACGTG-3') sequence of DNA with its partner MAX protein. It activates the transcription of more than 4000 genes whose products are involved in crucial aspects of cancer biology such as cell proliferation, cell growth, apoptosis and differentiation. There have been many approaches to down regulate MYC or its downstream genes, however, none of them has been succeeded to be developed as an anti-cancer drugs, because of the lack of drug-delivery system, or too complex treatment procedure.

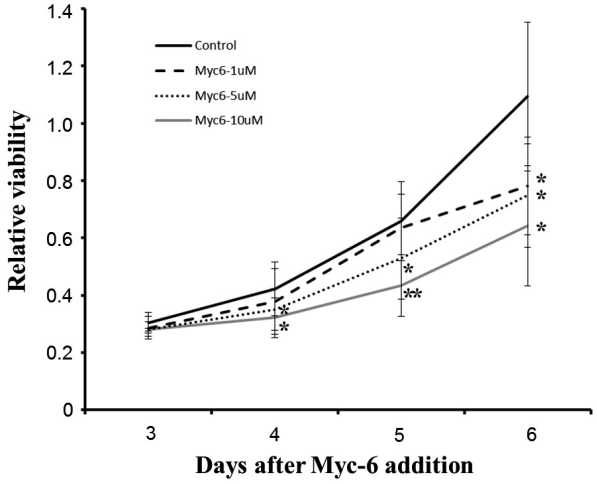

Fig.2 Growth inhibition of MG63 cells by treatment with Myc-6

We designed several PI polyamides which recognize E-box

consensus, and found that one of those PI polyamide Myc-6 inhibits proliferation of the many cells including osteosarcoma cell line MG63. The cells treated with 1μM or higher concentration of Myc-6 showed reduced growth rate when they were examined by WST8 assay and colony formation assay. When we analyzed the effect of Myc-6 treatment on cell cycle, dose dependent increase in the number of cells in sub-G1 or G1 phase, and reduction of cells in S-phase was observed. In addition, Myc-6 treatment increased the number of cells showing the phosphatidyl serine, which is the marker of early apoptosis, on their surface membrane, and also we found the increased amount of cleaved-caspase 3 in the cells treated with 10 μM of Myc-6. Collectively, those results strongly suggested that Myc-6 has an ability to promote apoptosis in MG63 cells.

To investigate the effect of Myc-6 *in vivo*, we injected MG63 cells subcutaneously into each anterior flank region of athymic nude mice. When tumor volume reached 200mm^3, mice were intravenously injected with Myc-6 at 6 mg/kg body weight once a week for a month. We found that Myc-6 treatment suppress tumor growth significantly compared to control cells. In addition, no evidence of toxicity for animals was observed.

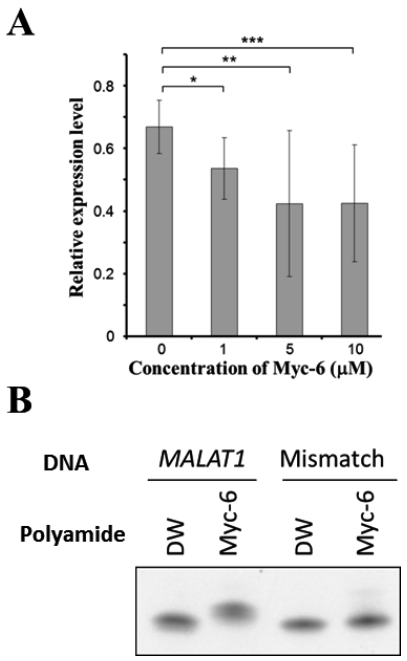

Fig.3 Regulation of *MALAT1* transcription by Myc-6

A. Myc-6 reduced expression level of *MALAT1* in MG63 dose dependently. **B.** In gel shift assay, DNA fragments containing E-box like motif on 5' upstream of *MALAT1* showed clear mobility shift in the presence of Myc-6.

By global gene expression analysis using microarray, 18 genes were found to be significantly down-regulated in MG63 cells treated with 10μM Myc-6. Among them, only *MALAT1*, which is coding long non-coding RNA, has Myc-6 binding sequence including E-box like motif on its 5'-upstream region. It was also shown by gel-shift assay that Myc-6 bind to this sequence specifically, and knockdown of *MALAT1* remarkably impaired the growth of MG63. Taken together, our present finding strongly suggested that Myc-6 suppresses malignant phenotypes of MG63 at least in part through the down regulation of *MALAT1* and also might provide a clue to develop a novel anti-tumor drug. Now, we are trying to improve the structure of Myc-6 to show stronger effect, and to develop new curative protocols using Myc-6 or improved Myc-6 in combination with conventional chemo drugs.

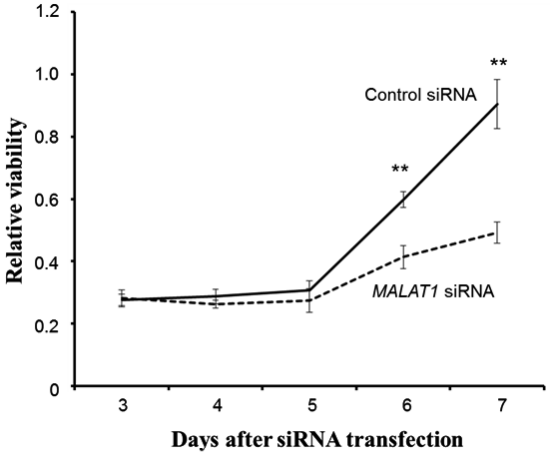

Fig.4 Effect of knock down of MALAT1 on the growth of MG63

Synthesis of Nano-Tube/Rod and Wide Band Gap Semiconductor Devices

Kaoru SUZUKI
Nanomaterials and Nanodevices

My research aims at fabrication of nano-materials and nano-devices for high functional applications such as nano-tube sensor or probe for magnetic force microscope, nano-tube/rod diode or transistor, and wide band gap semiconductor nano-film for water-splitting or light emitting diode or hydrogen storing alloy by using fundamental techniques of nano-process and fabrication of nano-materials. Using the achievement of the investigation, progress of energy conversion system, green- technology and bio-technology can be expected.

1. Metal encapsulated carbon nanotube for magnetic force microscope probes

We have synthesized directly ferromagnetic metal (Ni) and alloy (stainless-steel: SUS304) encapsulated linearly-extended carbon nanotubes (CNTs) for probe of magnetic force microscope or spin device on a mesh grid for viewing transmission electron microscope (TEM) by creeping arc discharge of ethanol (liquid) solution and silicon (solid) substrate in the cathode spot at tip of triangular pyramid shaped metal grid. These metals inside CNTs identified Ni and SUS with energy dispersive X-ray (EDX) spectrum analysis. The diameter and length of the metal core is in the range of 10 – 80 nm and 100 – 800 nm with varying heating period and temperature, respectively. The walls consist of cylindrical graphene sheets with 3 -50 layer. (Appl. Surf. Sci., DOI 10.1016/j.apsusc.2013.11.056, Patent Appl. No. 2010-198325) Figure 1 shows that TEM image of typically phase-separating stainless alloy filled CNT. The structure of the synthesized CNT processes 3 phases which indicate that monocrystal of $Fe_{2(1-x)}Cr_{2x}O_3$ in A part, polycrystal of $Fe_{2(1-x)}Cr_{2x}O_3$ in B part and monocrystal of $Fe_{(1-x)}Cr_x$ in C part by NBED analyses. (JPS Conf. Proc.2014)

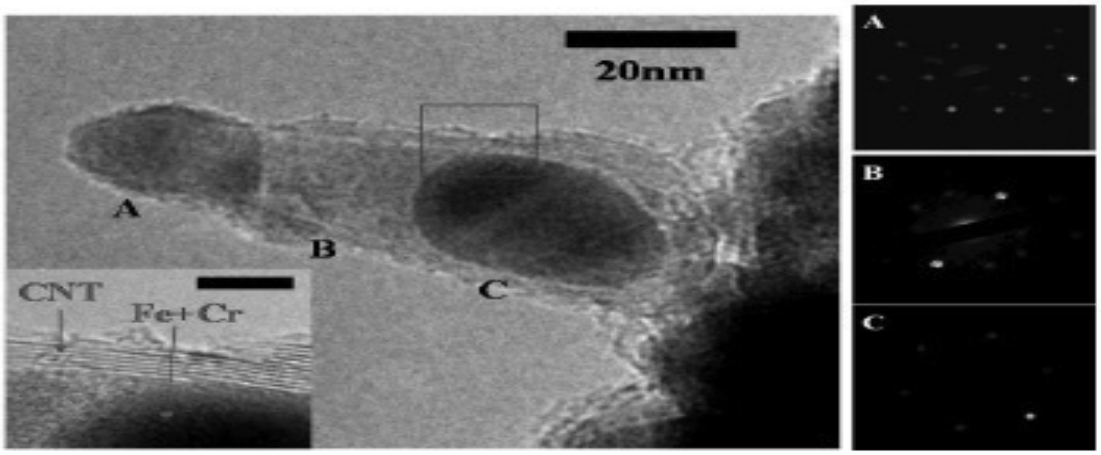

Figure 1. Transmission electron microscope image of stainless alloy filled CNT and NBED patterns

2. Creation of carbon nano-tube/rod and diamond-like carbon devices

We have synthesized phosphorus doped carbon nano-tube/rod by Joule heating on ethanol/Si surface assisted with laser irradiation for chirality controlling, and diamond-like carbon films by ion beam plating method(Appl. Phys. A, 101, 723-725). Type of p-n junction diode and wiring were created by focused Ga+ ion beam injection(J. Nanoele. Optoele., 7, 275-278). Carbon nano-tube/rod(Appl. Surf. Sci. 255, 9655-9658) forests were closely grown as shown in figure 2 (a), one of a CNT was processed by focused Ga+ ion beam. Voltage and current characteristic shown diode property in figure 2 (b), and n-type CNT back gate property in figure 2 (c).

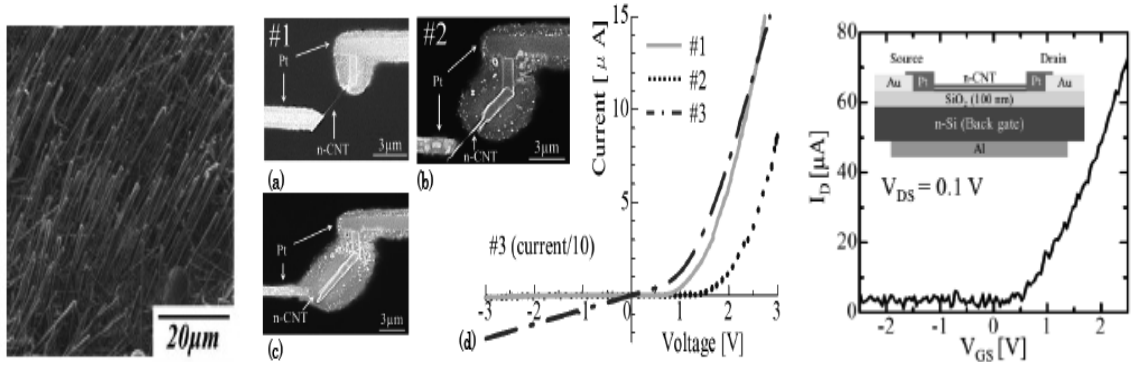

Figure 2. (a) Carbon nano-tube/rod forest (b) Diode property (c) Back gate property

3. Synthesize of photocatalytic $Sr_xLa_{1-x}TiO_3$ film for hydrogen generation

La doped TiO_2 have attracted great interest for photocatalytic properties, which can be used visible area in solar light although only TiO_2 limiting with ultra violet area. We have successfully crystallized perovskite structure films which were La doped TiO_2 thin film of $La_2Ti_2O_7$ (Appl. Surf. Sci., 255, 9688-9690), Sr doped TiO_2 thin film of $SrTiO_3$ and both impurity doped thin film of $Sr_xLa_{1-x}TiO_3$ (x=0.1~0.9). Now, we try to deposit of TiO_2 on polymer films by laser induced forward transfer method. (Appl. Mech. & Mat., 481, 125-128) magnetized coaxial plasma gun is utilized for a deposition of high-melting-point metal such as $Ti_{0.5}Zr_{0.5}(Fe_{0.2}Mn_{0.8})$ for hydrogen storing alloy collaborative study with professor Nishimiya and Asai. (JPS Conf. Proc.2014, Patent Appl. No.2012-195690)

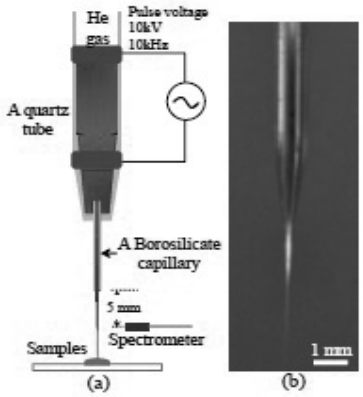

Figure 3. Low frequency and temperature micro plasma

4. Synthesis of ZnO nano-films for light emitting device

We have synthesis nitrogen doped p-type ZnO nano-films (Appl. Phys. A, 110, 963-966) by infrared light excited pulsed laser deposition method. High quality crystalline of p-type ZnO nano-films were improved (Appl. Phys. A, 101, 723-725) by pulsed YAG laser annealing below 532 nm ,and optimum wavelength was 266 nm.

5. Bio-electronics

Figure 3 show the sterilization of periodontal bacterium by atmosphere pressure low frequency/temperature micro plasma jet. The diameter of needle plasma was less than 50 mm, and temperature of plasma irradiated area was less than body temperature. Needle plasma showed emission due to OH and O radical. (JPS Conf. Proc.2014)

6. Green technology

Figure 4 show the evolution of controlled nano/micro bubble by laser/focused ion beam fabricated nozzle on piezoelectric vibrator for defecation of water. Micro bubbles were not able to generate from capillary nozzle without piezo-vibration, while micro bubbles, whose diameter was in the range of 2 mm to 500 mm, could be generated from the capillary nozzle with piezo-vibration. (Adv. Mat. Res., 871, 338-341, Patent Appl. No.2012-204982)

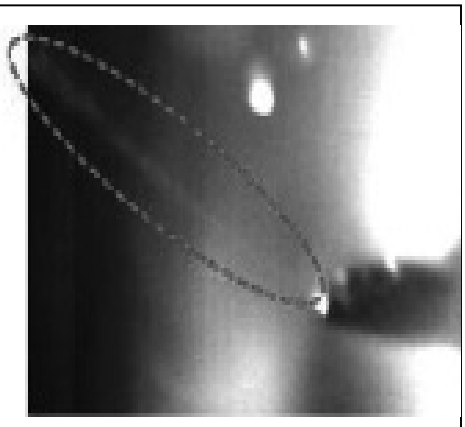

Figure 4. Nano/micro bubble ejected on piezoelectric vibrator micro nozzle

The development of newly molecular targeting drug for prostate cancer by using pyrrole-imidazole (PI) polyamide

Daisuke OBINATA, Satoru TAKAHASHI
Medicine

Under the close collaboration with Noboru Fukuda, Masayoshi Soma, and Kyoko Fujiwara, we have been developing new molecular targeting drug by PI polyamide for cancer therapy.

Prostate cancer is the second leading cause of cancer death in men in the USA. The androgen receptor (AR) plays a key role in the progression of prostate cancer. Until recently, the mainstay of therapy was to attenuate AR signaling pathway for prostate cancer. However, all men with androgen deprivation therapy for prostate cancer will eventually progress to castration resistant state. At that time they are termed as having castration resistant prostate cancer (CRPC). Several studies have shown that the majority of CRPC still express AR and androgen responsive genes, indicating that the AR signaling pathway is functional under androgen-depleted conditions. In addition, a recurrent fusion of TMPRSS2 with E26 transformation-specific (ETS) family genes were found in about 80% of prostate cancer tissues. ETS genes are transcription regulators, and altered expression or properties of them affect the control of transcriptional processes. Those alterations also could cause development and progression of cancer. Since TMPRSS2, 5'-fusion partner, was upregulated by androgen, AR has been supposed to be important to regulate the fusion genes in the prostate cancer. Aberrant overexpression of ERG induced by TMPRSS2-ERG fusion is likely to be involved in prostate cancer development including castrate resistant. Moreover, recent studies have shown that ligand-dependent binding of AR to intronic binding sites near the specific tumor translocation breakpoints (TGT/AGGGA/T) caused facilitating DNA double-stranded break (DSB) generation.
Pyrrole–imidazole (PI) polyamides are small synthetic molecules that recognize and attach to the minor groove of DNA, followed by inhibition DNA–protein interaction with high affinity and sequence specificity. Synthetic PI polyamides recognize and attach to the minor groove of DNA with high affinity and specificity.

(1) Efficacy of PI polyamide targeting of TMPRSS2-ERG gene fusion for prostate cancer cells
Here, we examined the effects of a PI polyamide targeting TMPRSS2-ERG translocation breakpoints (Fusion Polyamide) on prostate cancer. First, to determinate the binding affinity and specificity of polyamide to target DNA, gel mobility shift assays were performed. The fusion polyamide showed selective DNA binding ability. To determine whether fusion polyamide affects dihydrotestosterone (DHT)-dependent inter-chromosomal movement and TMPRSS2-ERG expression in LNCaP cells, we performed fluorescence in situ hybridization (FISH) analysis and measured TMPRSS2-ERG expression levels using quantitative reverse transcription-polymerase chain reaction (RT-PCR). After DHT treatment, the number of cells showing co-localization of TMPRSS2 and ERG was significantly increased in LNCaP cells cultured in the presence of negative control polyamide. This DHT-induced inter-chromosomal movement, however, was significantly decreased in cells cultured with fusion polyamide. The expression level of the TMPRSS-ERG transcript was also increased by DHT treatment; however, it was significantly suppressed in the presence of fusion polyamide compared with negative control polyamide. Moreover, we tested whether the fusion polyamide could down-regulate endogenous *ERG* gene expression. Fusion

polyamide substantially reduced mRNA expression levels of ERG in LNCaP cells.
Growth and migration of LNCaP cells treated with fusion polyamide were significantly suppressed compared with those of cells treated with negative control polyamide. Moreover, intravenous injection of fusion polyamide to athymic male mice bearing LNCaP-derived tumors resulted in growth retardation of the tumor. These results indicate that targeting of these breakpoint sequences by PI polyamide may be a new therapeutic intervention for prostate cancer (Japanese Unexamined Patent Application Publication No. 2013-234135).

(2) Polyamide targeting AR coregulator binding sites in long chain acyl-CoA synthetase 3 (ACSL3) enhancer region

AR is a member of the nuclear receptor superfamily and functions as a ligand-dependent transcription factor. Upon activation by androgens, AR translocates into the nucleus and binds to the androgen responsive elements (AREs). The transactivation of AR involves several coregulatory proteins. Aberrant expression of AR coregulators leads to AR hypersensitivity, which is one of the mechanisms underlying the progression of prostate cancer into a castrate-resistant state. Previously, we reported that one of nuclear receptor coregulators Oct1 could be a prognostic factor in prostate cancer as a coactivator of AR and may lead to the development of a new therapeutic intervention for prostate cancer (Obinata, Takahashi, et al. Int J Cancer 2012). Moreover, lipid metabolism is one of the diverse cellular functions regulated by androgen. ACSL3, which converts free long-chain fatty acids (16–22 carbons) into acyl-CoAs for ATP production through beta-oxidation and the generation of various lipids, was first reported as an androgen-responsive gene and ubiquitously expressed at the highest level in prostate tissue. Our previous chromatin immunoprecipitation study showed that the upstream region of ACSL3 includes a functional androgen receptor binding site (ARBS), which was putative ACSL3 enhancer. We found two non-canonical AREs, two Oct1 binding motifs, and one GATA2 motif in the putative ACSL3 enhancer ARBS in sequence. We validated two AREs and one Oct1 motif are functional by luciferase assay. Therefore, we prepared the novel PI polyamide targeting the Oct1 binding sites in ACSL3-ARBS (OCt1 BS polyamide) for selective knockdown of ACSL3. Cells were treated with either DHT for 24 h following luciferase assay. Synthetic PI polyamides targeting the Oct1 binding sites suppressed the proliferation and invasion of androgen-sensitive LNCaP prostate cancer cells, as well as in vivo tumor growth of LNCaP-derived xenografts in mice. These data indicate that ACSL3 plays an important role in prostate cancer progression and could offer a novel therapeutic strategy (Japanese patent application No 2013-048126).

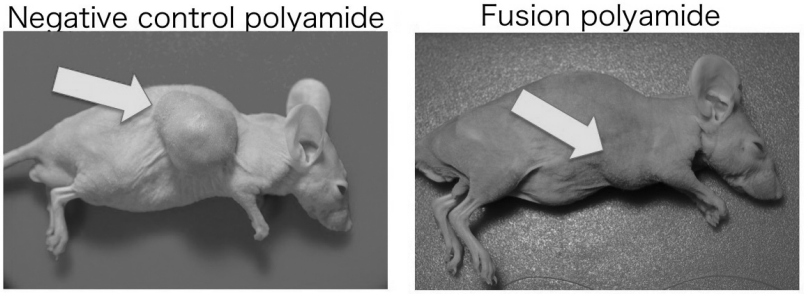

Figure 1. Fusion polyamide represses tumor formation of LNCaP cells in nude mice. Seven-week-old athymic male mice were implanted with 3 x 10^6 tumor cells and fusion polyamide or negative control polyamide was injected into the tail vein once weekly. Photographs of mice harboring tumors after 4 weeks of treatment with pyrrole–imidazole (PI) polyamide.

Mechanism of Superconductivity in Layered Iron-Arsenide Superconductors and Search of New Superconducting Compounds

Yoshiki TAKANO
Nanomaterials and Nanodevices

1. Introduction

In 2006, it was reported that (LaO)FeP became superconducting at about 4 K. Since $LaFeAsO_{1-x}F_x$ was discovered to be a superconductor in 2008, many iron-based superconductors have been found. All iron-based superconductors have Fe square lattices and they are classified roughly into four compounds, 1111, 111, 122, and 11 type superconductors due to their compositional ratio. In 2008, it was also reported that the superconducting transition temperature T_c of $Sr_{0.6}La_{0.4}FeAsF$ was 26 K and that of $Sr_{0.5}Sm_{0.5}FeAsF$ was 56 K. In 2010, oxygen deficient $LaFeAsO_{0.89}$ was also reported to be a superconductor with T_c of 28 K. As we have studied the electrical and magnetic properties of LaZnPnO (Pn=P, As, Sb) before the discovery of iron-based superconductors, we have mainly studied the 1111 type superconductors.

2. Experimental Results and Discussions

2.1 Superconductivity of La Deficient $La_{1-x}OFeP$

Although the superconducting transition temperature T_c of (LaO)FeP was firstly reported to be about 4K, several research groups reported different T_c in (LaO)FeP. Thus, the electrical properties of LaOFeP was controversial. We have succeeded to prepare almost single phase samples of $La_{1-x}OFeP$. The superconducting transition temperature T_c of (LaO)FeP is found to be 4.7K. T_c firstly increases with x and has a maximum value of 7 K at $x = 0.10$ and then decreases. The origin of the increase and the decrease of T_c is considered to be an introduction of holes in FeP layers due to the La deficiency. This result indicates that the origin of the previously reported scattering of T_c is the off-stoichiometry of the samples [1].

2.2 Crystal Structure and Superconducting Properties of $Sr_{1-x}R_xFeAsF$ (R=La, Pr, Nd, Sm)

When a part of Sr site was substituted by rare earth ions in SrFFeAs, the structural phase transition is suppressed and the superconductivity occurs. The study of $Sr_{1-x}R_xFeAsF$ besides R = La and Sm is quite a few. Then, we have prepared $Sr_{1-x}R_xFeAsF$ (R=La, Pr, Nd, Sm) and investigated their electric and magnetic properties. We have succeeded to almost single phase samples of them although a small amount of SrF_2 impurity is observed. The highest T_c is 49 K for $Sr_{0.5}Nd_{0.5}FeAsF$. This value is comparable with that of $Sr_{1-x}Sm_xFeAsF$. The value of the temperature derivative of the upper critical magnetic field (dH_{c2}/dT) at T_c is -1.5 T/K and the estimated value of H_{c2} at 0 K becomes about 75 T [2]. On the other hand, lattice parameters and T_c of $Sr_{1-x}Pr_xFeAsF$ are quite different from those of other compounds. This implies that Pr ions are not trivalent in $Sr_{1-x}R_xFeAsF$.

2.3 Preparation and Electrical Properties of $SrFeAsF_{1-x}$

As the electron doping due to the oxygen defficiency in $LaFeAsO_{1-y}$ induces high T_c superconductivity, high T_c superconductivity is also expected in $SrFeAsF_{1-x}$. Although the absolute values of the electrical resistivity decreases with x, supercondictivity is not observed above 3 K. The temperatrure dependence of the electrical resistivity is analyzed by the following power law formula; $\rho(T)=\rho_0+AT^n$ (Fig. 1). Although superconductivity is observed in the samples with n =1~2 for other iron-based superconductors, it is not observed in the sample with $x = 0.25$ which has n of

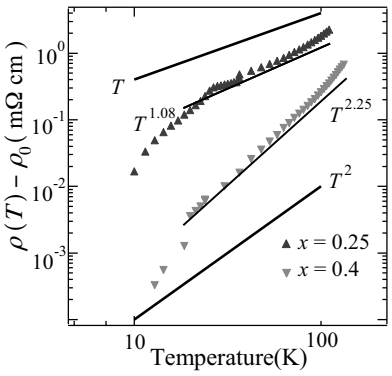

Fig. 1 Relation between $\log(\rho(T)-\rho_0)$ and $\log T$.

1.08 in this system.

2.4 Superconducting Properties of $Sr_{1-x}R_xFeAsF_{1-y}$ (R=La, Nd, Sm)

We have prepared the fluorine defficient $Sr_{1-x}R_xFeAsF_{1-y}$ for the optimum rare earth substituted $Sr_{1-x}R_xFeAsF$ (R=La, Nd, Sm). T_c decreases with y although the rare earth substitution and fluorine defficiency are expected to produce the same effects. The temperature dependence of the electrical resistivity in the normal region is analyzed by a power law, where ρ_0 was the resistivity just above T_c. Figure 2 shows the relation between n and y of $Sr_{1-x}R_xFeAsF_{1-y}$; x = 0.4 for R = La and x = 0.5 for R = Nd and Sm. As F deficiency y increases, n increased. This result is different from the previous study. Figure 3 shows the relation between n and T_c of $Sr_{1-x}R_xFeAsF_{1-y}$. As n increases, T_c decreases. Similar tendency was observed in other iron-based superconductors. It is independent of R ions. While the superconductivity is observed up to y = 0.15 for $Sr_{1-x}La_xFeAsF_{1-y}$ (low T_c compound), the superconductivity disappears at y = 0.05 for $Sr_{1-x}R_xFeAsF_{1-y}$ (R = Nd, Sm) (high T_c compound). n increases rapidly for $Sr_{1-x}R_xFeAsF_{1-y}$ (R = Nd, Sm) in a small y region and it gradually increases with y for $Sr_{1-x}La_xFeAsF_{1-y}$.

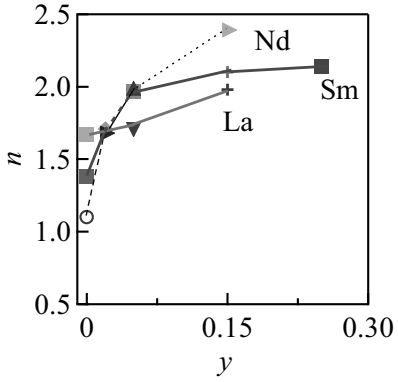

Fig.2 The relation n vs. y in $Sr_{1-x}R_xFeAsF_{1-y}$

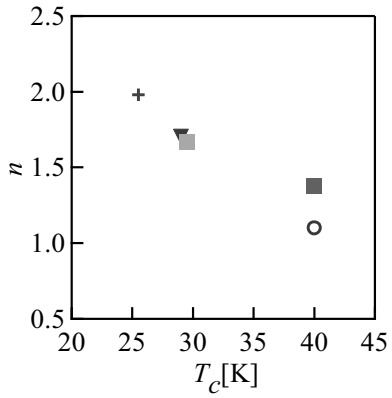

Fig. 3 The relation n vs. T_c in $Sr_{1-x}R_xFeAsF_{1-y}$

2.5 Crystal Structure and Electrical Properties of $LaFe_{1-y}Zn_yAsO$

Recently, it was reported that the optimum value of y which showed the highest T_c varied with x in $LaFe_{1-y}Zn_yAsO_{1-x}F_x$. We have prepared $LaFe_{1-y}Zn_yAsO$ for $0 \le y \le 1$. Mixed phase samples with LaFeAsO and LaZnAsO were obtained for middle region of y. Almost single phase samples were obtained for $y \le 0.2$. Lattice constants a and c increased with y in this region.

2.6 Preparation and Superconductivity of $LiFe_{1-x}Co_xAs$ and $Li_{1-x}Y_xFeAs$

LiFeAs is called 111-superconductor and is a superconductor with T_c of 18 K itself, which is different from other superconductors. We have prepared $LiFe_{1-x}Co_xAs$ and $Li_{1-x}Y_xFeAs$. T_c of LiFeAs is 10.8K which is smaller than the reported value. T_c of $LiFe_{0.98}Co_{0.02}As$ is 9.5 K and T_c decreases with increasing Co concentration. $Li_{0.9}Y_{0.1}FeAs$ does not show superconductivity above 3 K.

2.7 Electrical Properties of $SrFe_{1-x}Ni_xAsF$

As a part of the Fe site is substituted by Co ions in the FeAs-layer, it is reported that superconductivity occurs at 4 K. If the extra number of d electrons is important for the occurrence of superconductivity, Ni ions is considered to be more effective for the superconductivity. Then, we have prepared $SrFFe_{1-x}Ni_xAs$. Almost single phase samples are obtained for $0 \le x \le 0.2$. The kink temperature observed in the ρ-T curve which is due to the structural phase transition decreases with increasing x. Although all samples show a metallic conductivity, they are not superconducting above 3K.

2.8 Basic study for the application of $Sr_{1-x}Nd_xFeAsF$ for the superconducting wire rod

The upper critical magnetic field of $Sr_{0.5}Nd_{0.5}FeAsF$ is higher than that of MgB_2 that has the highest critical current density.

[1] X. Jin, T. Watanabe, K. Takase, Y. Takano, *J. Alloys and Compounds* **2009**, 488, L14-L16.

[2] R. Suganuma, Xinzhe Jin, T. Watanabe, K. Takase, Y. Takano, *J. Physics Conference Series* 200 (2010) 012193.

Ultra High Density Information Recording Materials on Self Assembled Nano-structured Substrates

Arata TSUKAMOTO, Akiyoshi ITOH
Information Storage; Supramolecules and Self-Assembly

In recent years, much attention has been focused on nano-structured magnetic media for achieving ultra high density recording up to several Tbit/inch^2. Combining self-assembly nano-structured substrates with defined magnetic properties provided by a magnetic film deposited onto the surface, enable a noble approach to create magnetic nanostructure arrays. We tried to prepare and utilize nano-structured substrates such as silica thin film having self-assembled nano-pores and self-assembled silica particle substrate.

1. Development of nano template substrate prepared by self-organization/-assembly phenomena

We tried to prepare and utilize nano-structured substrates such as SiO_2 thin film having self-assembled nano-pores and self-assembled silica particle substrate. Here, methods are presented for preparing the two different kinds of nano-structured substrates. One of them is a Nano-Dent Array (NDA) at the surface of SiO_2 layer which is including closed packed nano-pores prepared by the polymer micelles technique (Figures 1, 2) and the other is Self-Assembled spherical small Silica Particles (SASP) fabricated on Si substrates by the dip coating method (Figures 3, 4).

1-1 preparation of a Nano-Dent Array structure

1-1-1 Enlargement of the areal size of single domain nano-pore array structure

By reducing the molecular weight, the average diameter of nano-pores was decreased from 8nm (as see Fig. 2) to 5nm. Furthermore, the areal size of single domain nano-pore array structure was enlarged up to around 1μm^2 (> 8.8×10^5 nm^2) by reconsideration of fabrication process especially the sequence of compound molecules. See Fig. 5.

1-1-2 Thinning the silica layer with aligned nano pore array structure as 2 dimensional nano-pore allay structure

Nano-porous Silica layer was prepared by utilizing self-assembling phenomenon with main components of triblock copolymer(A), Tetra-Eth-Oxy-Silane (TEOS)(B), water with HCl(C) and Ethanol(D). Ethanol evaporates with drying process. By increase just the amount of Ethanol with keeping same ratio of other components A – C, prepared silica layer thickness was successfully reduced then achieved 2 dimensional nano-pore allay structure.

1-2 Nano structured template having a conjugate relation with nano-pore structure

As another type of nano structured template having a conjugate relation with nano-pore structure, nano convex pattern was prepared

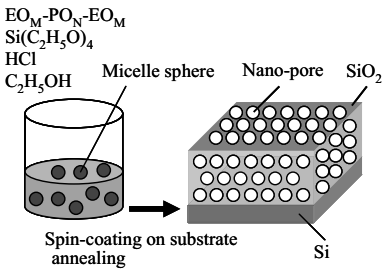

Fig. 1 Fabrication of SiO_2 thin films having self-assembled nano-pores.

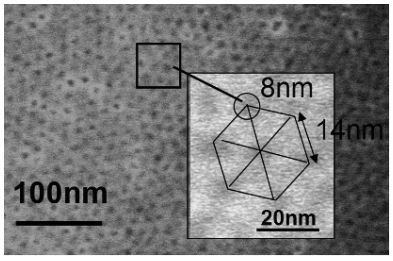

Fig. 2 SEM image of NDA (Nano Dent Array) surface.

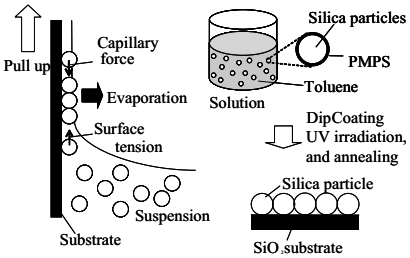

Fig. 3 Fabrication of SASP (Self-Assembled spherical small Silica Particles) layer.

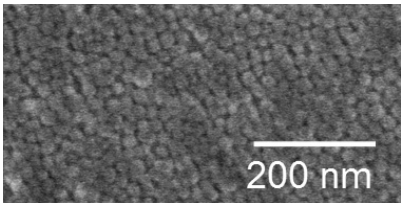

Fig. 4 SEM planer view of SASP (Self-Assembled spherical small Silica Particles) surface.

by using self-assembled spherical silica particles followed by inductively coupled plasma reactive ion etching.

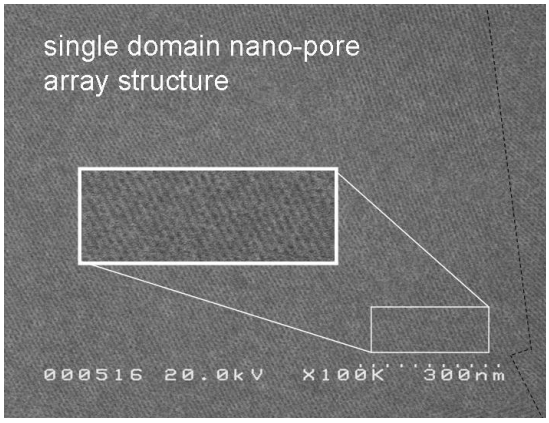

Fig. 5 SEM image of sirica thin film having nano dent array structure.

2. Preparation of isolated nano-magnetic particles by Rapid Thermal Annealing method

The Rapid Thermal Annealing (RTA) of Pt/Cu/Fe multilayered continuous films is effective to obtain perpendicularly magnetized small $L1_0$-FeCuPt grains on thermally oxidized Si substrate. We introduced Rapid Cooling Process into RTA. With the rapid cooling process, growing of grains were prevented, however new shoulder peak in XRD (X-ray diffraction) profile were appeared at slightly lower angle of FeCuPt (002) peak and it might be correspond to the disordered structure of FeCuPt. From electron diffraction patterns and dark field images of single grain by TEM, mostly $L1_0$-ordered polycrystalline structure was observed. Therefore, we preformed additional annealing to above isolated FeCuPt grains by using same annealing chamber of RTA, for crystallizing those poly-crystal grains to form single crystalline grains.

Annealing condition was decided as 600 degree C for 1 hour. The ordering temperature of FePt alloy is ~600 degree C and estimated atomic diffusion length is the order of third nearest neighbor distance in FePt at the annealing condition. From the comparison of the XRD profiles, the intensity of (001) super lattice peak which indicate the formation of $L1_0$-ordered phase is increased, and the shoulder peak at slightly lower angle of (002) is banished as shown in Fig. 6. Thus, FeCuPt grains and are expected to form single crystalline grains. After additional annealing, grains kept almost similar size. Furthermore, we observed crystal structure of a typical single grain after additional annealing by TEM. In most of grains, octagonal symmetric shape is appeared as shown in Fig. 7. From electron beam diffraction measurement of the single grain, series of {110} super lattice and {200} lattice spots are observed with fourfold-symmetry. {110} spots indicate the formation of $L1_0$-ordered structure. Thus, the grain consists of c-axis oriented single crystalline structure from complementary results of XRD covering macroscopic area and localized electron beam diffraction.

As a result, we found that an application of adequate additional annealing makes grains into $L1_0$ single crystalline structures and grains kept almost similar size.

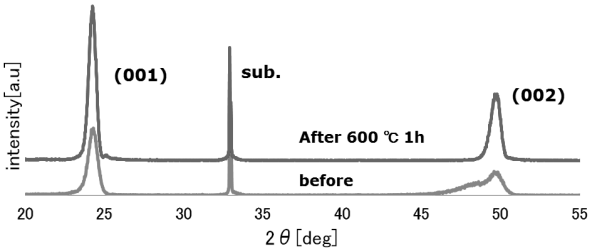

Fig. 6 XRD profiles of before and after the additional annealing

3. Achievement of high areal density magnetic particles

From the utilization of self-assembly prepared nano-structured substrate, high density FeCuPt magnetic nano-grains was prepared by rapid thermal annealing method as 5.4 T particles/inch^{-2} with average grain diameter of ~10 nm.

Furthermore, multiple formation process of the grain was performed for further increase in areal density of grains. By using this procedure, we got higher areal density of grains as 3.2 T particles/inch^{-2} on flat oxidized Si substrate.

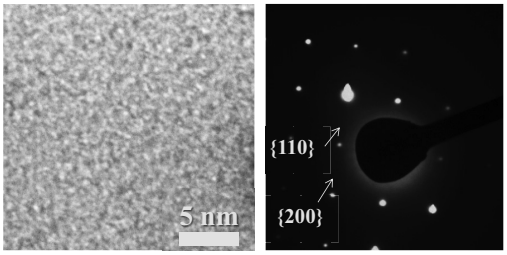

Fig. 7 Bright field image of TEM and Electron diffraction pattern for an isolated grain after additional annealing.

Ultra-Fast Information Recording and Ultra-Fast Photo Magnetic Switching

Arata TSUKAMOTO
Information Storage; Supramolecules and Self-Assembly

The ever increasing the capacity of storing information motivates the search for faster approaches to process and magnetically record information. Most computers store data on magnetic hard disk drives, in which the direction – "up" or "down" – of the magnetic moments in a small region of the disk corresponds to a binary bit. However, it was faced to unavoidable fundamental problem for faster operation in conventional way known as ferromagnetic resonance limit. We have experimentally demonstrated that an excitation of magnetization reversal phenomena can be triggered by the ultra-short pulsed laser irradiation. This finding reveals an ultrafast and efficient pathway for writing magnetic bits. Based on deep understanding of relationship between light and magnet including above new discovery, we are striving to establish the fundamental techniques of researching and developing ultrafast spin manipulation.

1. Ultra-fast demagnetization of magnetic recording medea with ultra-short pulsed laser

In conventional magneto-optical (MO) recording which triggered with nanoseconds pulsed laser irradiation, the time scale of heat-up and cool-down process depends on thermal diffusion property in multilayered recording media. The speed limits of heating and cooling process are important issue for fast heat assisted magnetic recording. Femtosecond pulsed laser light allow excitation of magnetic systems much shorter than the time scale of thermal diffusion. In this study, we investigated the film structure dependence of ultrashort laser-induced demagnetization of 20 nm thick GdFeCo alloy films, under the variety of with / without intermediate dielectric layer and heat sink layer. After the laser excitation, we found two time region from magnetic behavior: rapid step-like reducing process of magnetization and following recovering process with precessional motion. Figure 1 shows the ultrafast magnetic response of 20 nm thick GdFeCo alloy films triggered with ultrashort laser pulse irradiation measured by all-optical pump-probe method. Simultaneously, change of normalized reflectivity ΔR / R was measured for monitoring the time evolution of electron temperature.

The time scale of first rapid step-like demagnetization processes is conformed as within picoseconds range independently with film structure, which is much shorter than characteristic time scale of ferromagnetic resonance for all the cases. Following hundreds ps regime, film structure dependent precessional motion of magnetization was appeared. (*J. Magn. Soc. Jpn.,* 2012)

Furthermore, we demonstrated thermo-magnetic recording by ultra-short single laser pulse (FWHM: 90 fs).

2. All optical magnetization switching phenomena with ultra-short pulsed laser

It has been unexpectedly found that the ultrafast laser-induced spin reversal in GdFeCo, where spins are coupled antiferromagnetically, occurs by way of a transient ferromagnetic-like state (*Nature* 2011). Such a novel strongly non-equilibrium spin dynamics may lead to yet

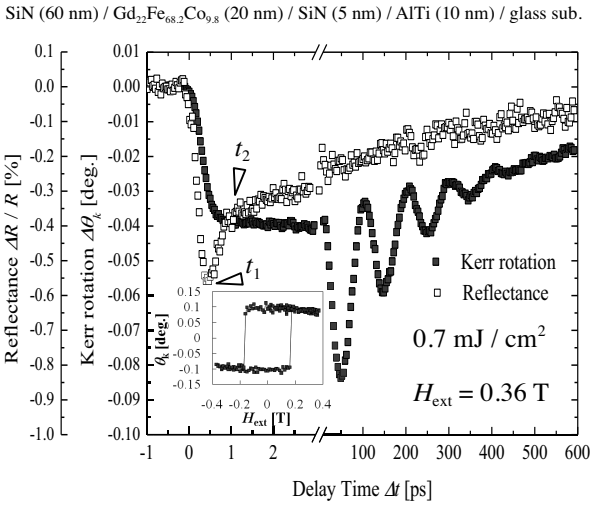

Fig. 1 Time-evolutions of the change of magneto-optical Kerr rotation $\Delta\theta_k$ and the normalized change of reflectivity ΔR / R of 20nm thick $Gd_{22}Fe_{68.2}Co_{9.8}$ alloy films. Inset figures show the magneto- optical Kerr effect hysteresis loops of each sample measured by same time-resolved observation set-up without pump laser.

unexplored magnetization reversal. We found that magnetization reversal could be achieved without any magnetic field, using an ultrafast thermal energy load alone (*Nature communications* 2012). Until now it has been generally assumed that heating alone, not represented as a vector at all, cannot result in a deterministic reversal of magnetization, although it may assist this process. We found experimentally deterministic magnetization reversal in a ferrimagnetic GdFeCo driven by an ultrafast heating of the medium resulting from the absorption of a sub-picosecond laser pulse without the presence of a magnetic field. Fig. 2 shows magneto-optical image of magnetic domains after single pulse laser irradiations. Subtracted (difference of each sets of images) images shows various magnetic domain was reversed in same areal size by laser irradiation for all the cases. A further set of experiments shows that this switching occurs independently of polarization and initial state in thin films of GdFeCo. Importantly for technological applications, we show experimentally that this type of switching can occur when starting at room temperature.

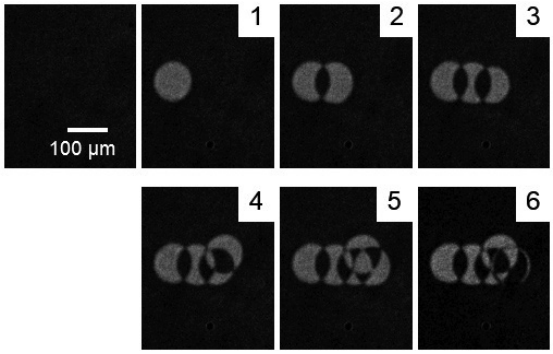

Fig. 2 Magneto-optical image of magnetic domains after single pulse laser irradiations.

3. The origin of all-optical light helicity-dependent magnetic switching

Direct demonstration of all-optical light helicity-dependent magnetic switching (AO-HDS) was observed in ferrimagnetic GdFeCo alloys in the absence of an external magnetic field, which became subject of intense discussion in modern magnetism. The most obvious explanation via the inverse Faraday effect (IFE) could only very qualitatively account for the previously observed features. What is the origin of the helicity dependence in the all-optical switching?

We found that all-optical switching with circular polarized (CP) femtosecond laser pulses in ferrimagnetic GdFeCo is related to the collinear sub-lattice magnetization and not with the net magnetization. Furthermore, we reached an explanation of the AO-HDS based on magnetic circular dichroism (MCD). Using magneto-optical microscopy in combination with femtosecond pulsed light, we measured the composition dependency (X:22~27) of AO-HDS in $Gd_x(Fe_{87.5}Co_{12.5})_{100-x}$. The relation between the direction of reversed net magnetization and helicity of the light changed sign by going across the magnetization compensation composition ratio C_M (X~24.5). We also found that the sign of MCD changed at C_M. It was hypothesized that CP light acts as a strong effective magnetic field pulse H_{OM} on the spins of the medium through the IFE. The direction of H_{OM} is then defined by the helicity of the light. The above results do not match with the description based on the IFE. We already reported that ultrafast heating can act as a sufficient stimulus for magnetization reversal in a ferrimagnet with taking into account the multi-sublattice nature as mentioned in section 2. The above results show that the helicity-dependent absorption in a multi-sublattice magnetic layer exactly matches the helicity-dependent features in switching experiments. (*Springer Verlag*, 2014)

We demonstrate that via careful tuning of the conditions in circularly polarized laser irradiation, it is possible that all optically and magnetically record an information in the metallic ferrimagnet GdFeCo as shown in Fig. 3. Furthermore, we clarified that the magnetization direction of high anisotropic magnetic recording media of TbFeCo can be switched by irradiation of circularly polarized ultra-short pulsed laser without magnetic field.

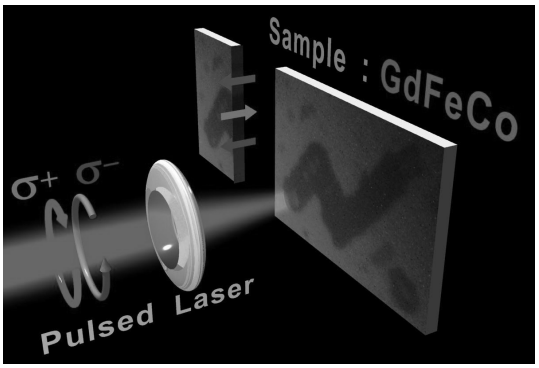

Fig. 3 The demonstration of all-optical information recording on magnetic media.

Switching Effect and Confinement efficiency by Dielectric Waveguide with Photonic Nanostructures

Tsuneki YAMASAKI
Quantum Theory and Computation

We have analyzed the scattering and guiding problems by dielectric waveguides with defects composed of dielectric circular cylinders array loaded with dielectric rectangular cylinder and arbitrary dielectric structure in the middle layer, and investigated the influence of power transmitted coefficients by using the combination of improved Fourier series expansion method and multilayer method and the distribution of energy flow for defect area utilizing the propagation constants at the guided region. We have investigated the optimum dielectric structure to obtain the switching effects or confinement efficiency.

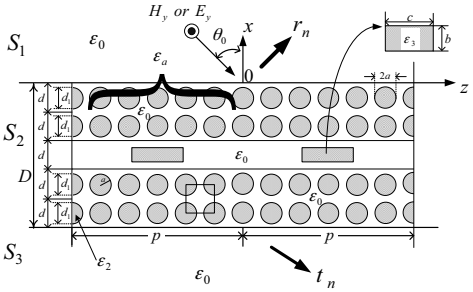

Fig.1 Structure and coordinate system of dielectric waveguide loaded with dielectric rectangular cylinder in the middle layer

Numerical results are given for the influence of the incident angle and normalized frequency of the transmitted power in terms of the parameter $\varepsilon_3/\varepsilon_0$ of the rectangular cylinders in the middle layer sandwiched between two multilayers, yielding the basis characteristics of resonance peak for switching or frequency selective devices for both TM and TE cases.

1. Switching effect of photonic structure for case of loaded with dielectric rectangular cylinder[1]

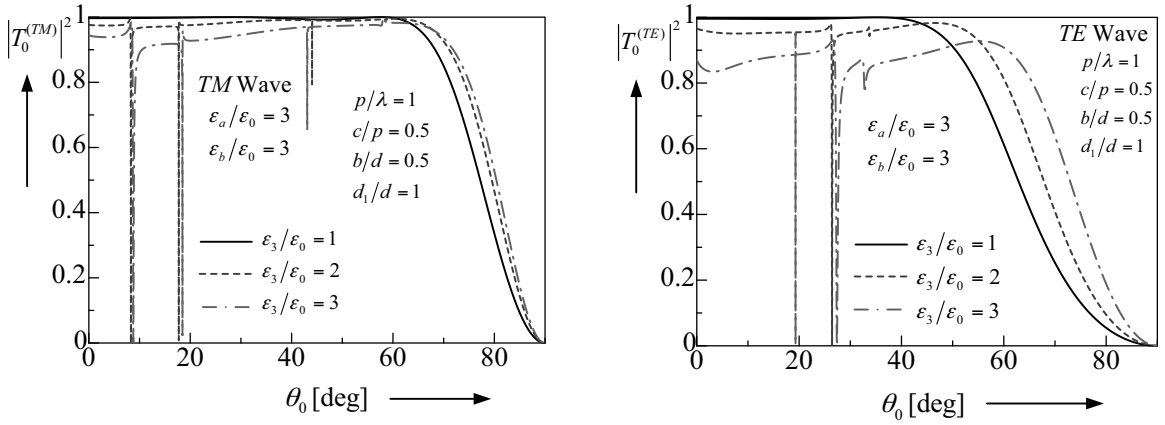

(a) TM wave (b) TE wave

Fig.2 0-th mode power transmitted coefficients vs. incident angle

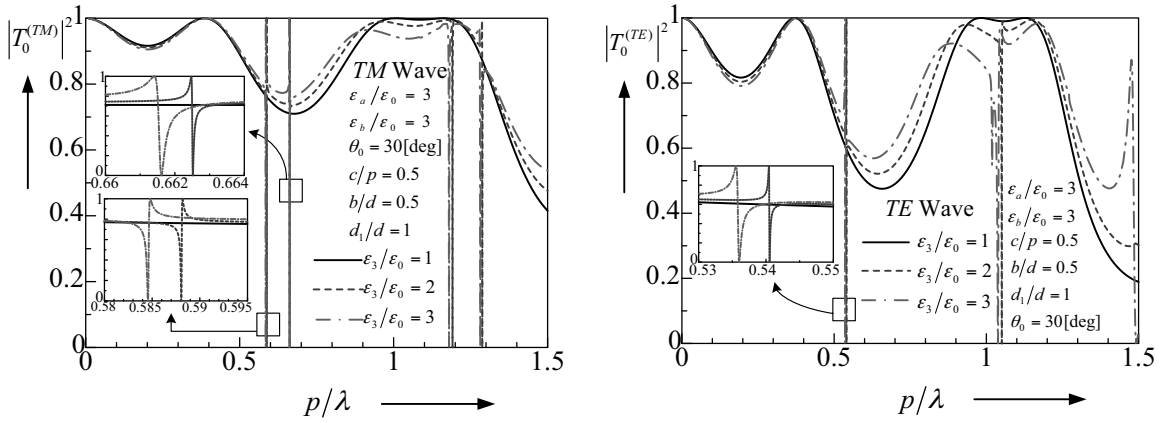

(a) TM wave (b) TE wave

Fig.3 0-th mode power transmitted coefficients vs. normalized frequency

2. Confinement efficiency of photonic structure for case of loaded with arbitrary dielectric structures[2,3,4].

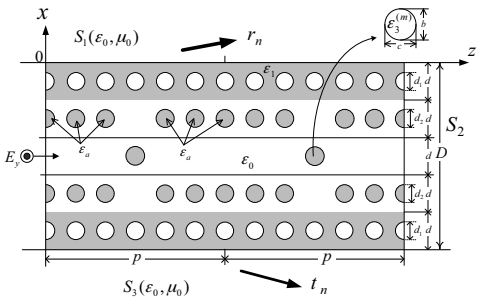

Fig.4 Structure and coordinate system of dielectric waveguides composed of dielectric circular cylinder array with air-hole

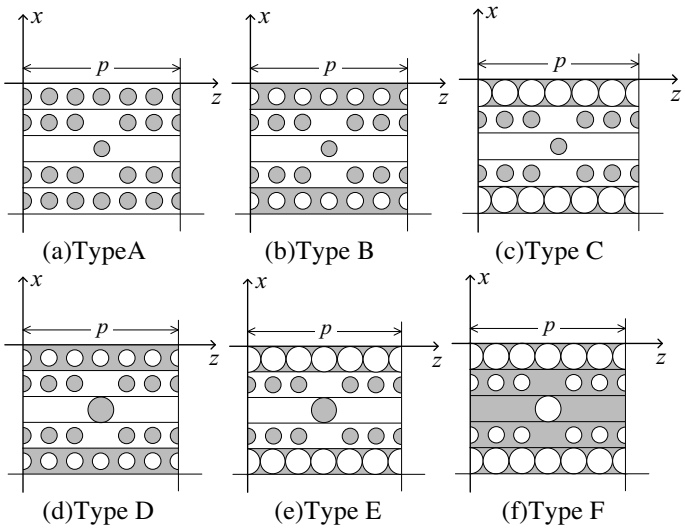

Fig.5 Structure of dielectric waveguide model

We consider the dielectric waveguides composed of dielectric circular cylinder array with air-hole type circular cylinder array as shown in Fig.4. Here, the structures in this study of analyses model are shown in Fig.5.

Figures 6(a) and (b) show the distribution of energy flow at the guided area for types A and B as condition of excited normalized frequency $p/\lambda = 0.4814$ and $p/\lambda = 0.4368$, respectively. And also, the circles of solid and dashed lines denote the position that it is placed the dielectric circular cylinders or air-hole circular cylinders corresponding to in Fig.5. Form these results, we can see the following features:

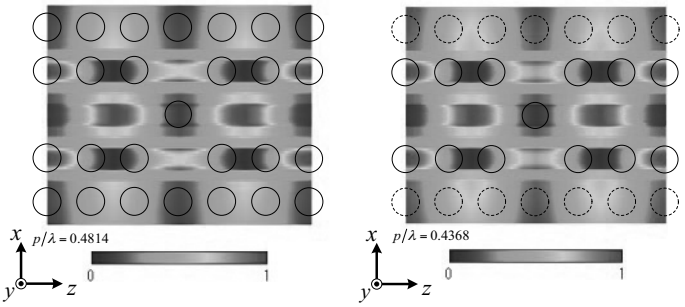

Fig.6 Distribution of energy flow at guided area for types A and B

(1)From a comparison of structure type A and type B, the energy of defect area for type B can be concentrated than that of structure type A.

(2)We obtained the confinement efficiency by type B compared with previous structure type A[2,3,4].

[1]R. Ozaki, T. Yamasaki, and T. Hinata ; "Scattering of Electromagnetic Waves by Dielectric Gratings with Dielectric Rectangular Cylinders Sandwiched between Two Multilayeres" , *IEEJ Trans. Fundamentals and Materials*, vol.129-A, no.10, pp.718-724, 2009.

[2]R. Ozaki and T. Yamasaki ; "Distribution of Energy Flow by Dielectric Waveguide with Rhombic Dielectric Structure along a Middle Layer", *IEICE Electronics Express*, vol.9, no.7, pp.698-705, 2012.

[3]R. Ozaki and T. Yamasaki ; "Distribution of Energy Flow for Defect Area by Air-hole Type Dielectric Waveguide", *The Technical Report of the IEEJ*, EMT-12-70, pp.29-34, 2012. (*in Japanese*)

[4]R. Ozaki and T. Yamasaki ; "Distribution of Energy Flow and Propagation Characteristics by Multilayered Dielectric Waveguide Composed of Dielectric Circular Cylinders and Air-hole Type Circular Cylinders", *The Technical Report of the IEEJ*, EMT-12-175, pp.1-6, 2012. (*in Japanese*)